SLAC-PUB-5219
March 1990
E/T

Precision Experiments in Electroweak Interactions*

MORRIS L. SWARTZ

Stanford Linear Accelerator Center
Stanford University, Stanford, California, 94309

Presented at the Seventeenth SLAC Summer Institute:
Physics at the 100 GeV Mass Scale,
Stanford Ca., July 10-21, 1989

* Work supported by the Department of Energy, contract DE-AC03-76SF00515.

Table of Contents

1. Introduction

The electroweak theory of Glashow, Weinberg, and Salam (GWS) has become one of the twin pillars upon which our understanding of all particle physics phenomena rests. It is a brilliant achievement that qualitatively and *quantitatively* describes all of the vast quantity of experimental data that have been accumulated over some forty years. Note that the word *quantitatively* must be qualified. The low energy limiting cases of the GWS theory, Quantum Electrodynamics and the V−A Theory of Weak Interactions, have withstood rigorous testing. The high energy synthesis of these ideas, the GWS theory, has not yet been subjected to comparably precise scrutiny.

The recent operation of a new generation of proton-antiproton ($p\bar{p}$) and electron-positron (e^+e^-) colliders has made it possible to produce and study large samples of the electroweak gauge bosons $W^\pm$ and Z^0. We expect that these facilities will enable very precise tests of the GWS theory to be performed in the near future. In keeping with the theme of this Institute, *Physics at the 100 GeV Mass Scale*, these lectures will explore the current status and the near-future prospects of these experiments.*

* In other words, we will use the title of this school as an excuse to ignore the many lower-energy, neutral current tests of the GWS theory. The two lecture format of this presentation precludes a more exhaustive treatment of the field.

LECTURE I

2. Parameters of the Standard Model

The minimal Standard Model contains some 21 empirical parameters. They are listed in Table I with their approximate values.

Table I

Parameter	Description	Approximate Value
g_s	SU(3) coupling constant	1.3 @ 34 GeV
g	SU(2) coupling constant	0.63
g'	U(1) coupling constant	0.35
$\langle\phi\rangle$	VEV of the Higgs field	174 GeV
M_H	Higgs boson mass	?
m_{ν_e}	electron neutrino mass	< 12 eV
m_{ν_μ}	muon neutrino mass	< 0.25 MeV
m_{ν_τ}	tau neutrino mass	< 35 MeV
m_e	electron mass	0.511 MeV
m_μ	muon mass	106 MeV
m_τ	tau mass	1.78 GeV
m_u	up-quark mass	5.6 MeV
m_d	down-quark mass	9.9 MeV
m_s	strange-quark mass	199 MeV
m_c	charm-quark mass	1.35 GeV
m_b	bottom-quark mass	5 GeV
m_t	top-quark mass	?
$\sin\theta_{12}$	K-M Matrix parameter	0.217-0.223
$\sin\theta_{23}$	K-M Matrix parameter	0.030-0.062
$\sin\theta_{13}$	K-M Matrix parameter	0.003-0.010
$\sin\delta$	K-M Matrix parameter	?

The dynamics of electroweak *Physics at the 100 GeV Mass Scale* are determined (at tree level) by three of the parameters: the SU(2) coupling constant (g),

the U(1) coupling constant (g'), and the vacuum expectation value of the Higgs field ($\langle\phi\rangle$). The complete specification of the electroweak sector of the Standard Model requires that all three parameters be *precisely* known. The values of these quantities are extracted from the measurement of three related quantities: the electromagnetic fine structure constant (α), the Fermi coupling constant (G_F), and the mass of the Z^0 boson (M_Z). The current values of these quantities are listed in Table II.

Table II

The current values of the physical parameters that determine the determine the electroweak sector of the Standard Model.

Quantity	EW Parameters	Current Value	Precision (PPM)
α	$\frac{1}{4\pi}\frac{g^2 g'^2}{g^2+g'^2}$	$[137.0359895(61)]^{-1}$	0.045
G_F	$\frac{1}{\langle\phi\rangle^2\sqrt{8}}$	$1.16637(2)\times10^{-5}$ GeV^{-2}	17
M_Z	$\sqrt{\frac{g^2+g'^2}{2}}\langle\phi\rangle$	91.16(3) GeV	320

The value of α is extracted from a very precise measurement of the anomalous magnetic moment of the electron.[1] The value of G_F is derived from the measured value of the muon lifetime.[2] The first precise measurements of the Z^0 mass have been made quite recently.[6] Although M_Z is determined with far less accuracy than are α and G_F, it is expected to remain the most well-determined Standard parameter for the foreseeable future. It is clear that the measurement of a fourth physical quantity should overconstrain the determination of the electroweak parameters. We should therefore be able to *test* the electroweak sector of the Standard Model.

Unfortunately, the expression given in Table II that relates M_Z to g, g', and $\langle\phi\rangle$ is valid only at tree-level. Since M_Z is measured at a substantially larger energy scale than are α and G_F, we must include virtual electroweak corrections in order to extract accurate values for the electroweak parameters. In principle, this requires a knowledge of all of the parameters listed in Table I. In practice, a dispersion relation is used to determine the dominant correction (due to low mass

fermion loops) from the low energy e^+e^- total cross section. The largest remaining corrections depend upon the top quark mass (strongly) and the Higgs boson mass (weakly). A reasonably precise test of the Standard Model therefore requires at least two more experimental measurements (ideally a measurement of m_t would be one of them).

At high energies, all of the proposed tests of the Standard Model fall into one of two categories:

1. An improved measurement of the W boson mass,

$$M_W^2 = \frac{g^2}{2}\langle\phi\rangle^2(1+\delta_{RC}^W), \tag{2.1}$$

   where M_W is the W boson mass and δ_{RC}^W accounts for the virtual electroweak corrections.

2. A measurement of the ratio of the vector and axial vector parts of the Z^0 coupling to a fermion-antifermion ($f\bar{f}$) pair. The vector and axial vector coupling constants (v_f and a_f, respectively) are given by the following expression,

$$\begin{aligned} v_f &= \tau_3^f - 4Q_f\frac{g'^2}{g^2+g'^2} \\ a_f &= -\tau_3^f \end{aligned} \tag{2.2}$$

   where τ_3^f is twice the third component of the fermion weak isospin and Q_f is the fermion charge.

The Standard Model tests that fall into the second category measure one combination of coupling constants. At tree-level, this combination is the well-known electroweak parameter $\sin^2\theta_w$,

$$\sin^2\theta_w = \frac{g'^2}{g^2+g'^2}. \tag{2.3}$$

To good approximation, the virtual corrections that affect each quantity in the category can be absorbed into the definition of $\sin^2\theta_w$. We can therefore use the

tree-level $\sin^2\theta_w$ sensitivities of the second-category quantities to compare their sensitivities to the electroweak parameters and loop corrections.

3. Experiments at Hadron Colliders

High energy physics, like most fields of scientific endeavor, follows trends that are determined as much by psychology as by logic. In the decade of the 1970's, the electron-positron collider was preeminent. The great success of the SPEAR storage ring at SLAC lead to the construction of larger projects at DESY, SLAC, Cornell, and KEK. The experimental program at the CERN ISR (which was the world's only hadron-hadron collider) was rather slow in bearing fruit and never did produce a major discovery.*

In the 1980's, the situation was somewhat reversed. The large program of moderate energy e^+e^- storage rings (25-60 GeV in the cm frame) produced no major discoveries.† On the other hand, the observation of the $W^\pm$ and Z^0 bosons at the CERN Sp$\bar{\text{p}}$S Collider provided fairly dramatic evidence that the GWS theory of electroweak interactions is substantially correct. This has lead to the great popularity of high energy hadron-hadron colliders and to the plans for the building of the SSC in the US and the LHC at CERN. Perhaps some discovery at SLC/LEP will cause the pendulum to swing the other way?

At the current time, there are two active hadron colliders in the world, the Sp$\bar{\text{p}}$S at CERN and the Tevatron collider at Fermilab. The parameters of the two machines are summarized in Table III. Note that substantial upgrades of the Tevatron collider are being proposed for the next several years.

⋆ The observation of large transverse momentum scattering processes did lend support, along with data from electron-nucleon scattering experiments, to the parton model of hadrons.

† The observation of an increased fraction of three-jet events in the total hadronic cross section was strong supporting evidence for Quantum Chromodynamics. The reader is requested to consider whether these data could have been termed *the discovery of the gluon* in the absence of a very detailed theory and several very detailed simulations.

Table III

Machine	Energy	Peak Luminosity	Integrated Luminosity
$Sp\bar{p}S$	630 GeV	$3\times10^{30}cm^{-2}sec^{-1}$	6.7 pb^{-1}
Tev I	1.8 TeV	$1\times10^{30}cm^{-2}sec^{-1}$	4.7 pb^{-1}
Tev I(1995)	1.8 TeV	$5\times10^{31}cm^{-2}sec^{-1}$	300 pb^{-1}?

3.1. Experimental Details

There are four experiments that are active or in preparation at the $Sp\bar{p}S$ and the Tevatron: the UA1 and UA2 experiments at CERN, and the CDF and D0 experiments at Fermilab. The main features of the these experiments are as follows:

1. Large Solid Angle Calorimeters - each experiment utilizes a calorimeter that covers the entire azimuth in a region of polar angle that extends to within $\sim 5^\circ$ of the beam direction. These devices are usually segmented transversely and longitudinally. The longitudinal segmentation permits the separation of electron and photon showers from hadron showers. The energy resolution of these devices is typically $\delta E/E \sim 0.15/\sqrt{E}$ (E in GeV) for electromagnetic showers and $\delta E/E \sim 0.80/\sqrt{E}$ for hadronic showers. Additionally, the overall energy scale of a typical calorimeter is uncertain to $\lesssim 1\%$ for electromagnetic showers and $\sim 3.5\%$ for hadronic showers.

2. Magnetic Spectrometers - The UA1 and CDF experiments contain large charged particle tracking systems that are immersed in magnetic fields. They are capable of reconstructing transverse momenta with resolutions in the range $\delta P_t/P_t \sim$(0.001-0.005)$\cdot P_t$ (where P_t is in GeV). Although these resolutions are inferior to those of the calorimeters for high energy electrons, the CDF collaboration have managed to control the momentum scale uncertainty to a few tenths of a percent. The UA2 and D0 experiments have charged particle tracking systems but are not capable of charged particle momentum reconstruction.

3. Muon Spectrometers/Identifiers - The UA1, CDF, and D0 experiments have magnetized iron shielding for the identification and measurement of muon tracks. The momentum resolution of these systems is poor as compared with the inner tracking systems mentioned above.

4. Triggers - All four experiments need fairly sophisticated, calorimeter-based triggers to ignore the large rate ($\sim$ 100 kHz) of ordinary hadronic interactions. The triggers normally require that preselected patterns of transverse energy* be deposited into the calorimeter. The energy thresholds are adjusted to reduce the trigger rates to a few Hertz.

Observable Quantities

As the energies of storage rings and collider complexes have increased, the importance of observing individual final-state hadrons has declined. This is particularly true in hadron colliders. The experimentally observable and measurable quantities are as follows:

1. Hadron Jets - the signature of a quark or gluon jet in a typical detector is a cluster of energy in the calorimeter. The transverse and longitudinal extent of the energy deposition is much larger than that associated with an electron or photon. A large number of charged tracks is usually required to originate from a vertex and point to the cluster.

2. Electron - the signature of an electron in a typical detector is a cluster of energy in the calorimeter of small transverse and longitudinal extent. A charged track must be associated with the cluster. The track-calorimeter matching is improved with the use of high granularity preshower detectors, high granularity layers in the calorimeter, or position sensitive detectors embedded in the calorimeter. The UA1 and CDF experiments also require that the momentum of the charged track (as measured by magnetic deflection)

* Transverse energy is defined as the product of the energy deposited into a calorimeter segment and the sine of the polar angle subtended by the segment.

agree with the energy that is measured in the calorimeter. All of the experiments require that electron candidates pass an isolation criterion of some description (typically, less than a few GeV of energy must be detected in a cone of 15°-40° about the track-cluster).

3. Muons - the signature of a muon is a charged track that penetrates the iron muon identifier. The track is required to match to a charged track in the central detector. The central track must not show any sign of a *kink* that could be associated with the decay of a pion or kaon. The energy measured in the calorimeter must be consistent with the passage of a minimum ionizing particle. Additionally, the muon candidate must pass an isolation criterion that is similar to the one applied to electron candidates.

4. Neutrinos - the large coverage of the calorimeters permits the reconstruction of the net transverse momentum vector of the entire event (relative to the beam axis). The measurement of the net longitudinal momentum of the event requires calorimetric coverage to quite near the beam direction and is not practical. Since the transverse momentum of the initial state is zero, the total event transverse momentum measures the total transverse momentum of all non-interacting particles. Neutrinos with large transverse momenta can be identified and tagged by this technique. The missing transverse momentum (P_t^{miss}) resolution of a typical detector is given by the following expression,

$$\delta P_{T_{x,y}}^{miss} = (0.5 \rightarrow 0.7) \cdot \sqrt{E_t^{obs}} \text{ GeV}$$

where x, y are the directions that are orthogonal to the beam axis and where E_t^{obs} is the total transverse energy that is observed in the calorimeter (the energy of each cell weighted by the sine of the polar angle).

It is clear that large P_t electrons and (in the case of CDF) muons are much better measured quantities than are jets or neutrinos. The most serious backgrounds to large transverse momentum charged leptons are due to low multiplicity hadronic jets. The rejection power of the selection criteria is typically several $\times 10^4$. The

efficiency to detect a large P_t lepton is typically 50% to 75% depending upon the detector and the selection criteria.

3.2. Gauge Boson Production

All the electroweak tests that have been performed at hadron colliders involve the measurement of gauge boson properties. It is important to remember that gauge boson production in these machines is a small part of the total cross section. The signatures and cross sections for gauge boson production are compared with those of hadronic processes in Table IV.

Table IV

Process	Signature	σ(0.63 TeV)	σ(1.8 TeV)
Soft Collision	E_t = 5-10 GeV 15-25 charged tracks	$\sim 6\times10^7$ nb	$>6\times10^7$ nb
Hard Collision	Two large P_t jets back-to-back azimuthally	$\sim$600 nb ($P_t^j>$30 GeV)	$\sim$3000 nb ($P_t^j>$32 GeV)
$p\bar{p} \rightarrow W \rightarrow q\bar{q}$	Two large P_t jets back-to-back azimuthally	$\sim$3 nb	$\sim$15 nb
$p\bar{p} \rightarrow Z \rightarrow q\bar{q}$	Two large P_t jets back-to-back azimuthally	$\sim$1 nb	$\sim$5 nb
$p\bar{p} \rightarrow W \rightarrow \ell\nu$	Large P_t lepton	$\sim$0.5 nb	$\sim$2.5 nb
$p\bar{p} \rightarrow Z \rightarrow \ell\ell$	Two large P_t leptons	$\sim$0.05 nb	$\sim$0.25 nb

Note that the hadronic final states of the gauge bosons have a signature that is very similar to that of the dominant large P_t scattering process. For this reason, all precise gauge boson measurements make use of the leptonic final states.

Drell-Yan Mechanism

The hadronic production of the $W^{\pm}$ and Z^0 bosons occurs via the well-known *Drell-Yan* mechanism which is illustrated in in Figure 1. The incident proton and antiproton have momenta k_1 and k_2, respectively. A parton carrying a fraction

x_1 of the proton momentum collides with a parton carrying a fraction x_2 of the antiproton momentum. The two lowest order subprocesses that produce gauge bosons are shown in parts a) and b). The dominant subprocess is the $q\bar{q}$ annihilation diagram shown in part a). Note that the emitted gluon is optional and is shown only to illustrate the production mechanism for gauge boson transverse momenta. The second subprocess is the Compton scattering of a quark and gluon. This process is higher order in α_s than the basic process (without initial state gluon radiation) and is important when the longitudinal or transverse momentum of the gauge boson is large.

The parton-parton center of mass energy, $\sqrt{\hat{s}}$, has a simple relationship to the hadron-hadron center of mass energy $\sqrt{s}$,

$$\hat{s} = x_1 x_2 s = \tau s \tag{3.1}$$

where the definition of τ is obvious. If the gauge boson transverse momentum $P_t^{W,Z}$ is small as compared with its mass, the gauge boson longitudinal momentum is given by the following simple expression,

$$P_L^{W,Z} = P_{beam} \cdot (x_1 - x_2), \tag{3.2}$$

where P_{beam} is the beam momentum.

Assuming that the annihilation subprocess dominates the cross section, we can therefore write the lowest order differential cross section as,

$$\frac{d\sigma_0}{dx_1 dx_2} = \frac{1}{N_c} \sum_{i,j} \left[\frac{q_i^1(x_1)\bar{q}_j^2(x_2)}{x_1 x_2} + \frac{\bar{q}_j^1(x_1) q_i^2(x_2)}{x_1 x_2} \right] \hat{\sigma}_{ij}(x_1 x_2 s), \tag{3.3}$$

where: $q_i^1(x_1)/x_1$ is the probability of finding a quark of species i in the proton with momentum fraction x_1; N_c is a color factor (3) to account for the probability of finding a quark-antiquark pair in a color-neutral state; and $\hat{\sigma}_{ij}(\hat{s})$ is the cross section for the annihilation of quark species i and j with a $q\bar{q}$ cm energy of $\hat{s}$.

The QCD radiative corrections to equation (3.3) are quite substantial. Real gluon emission produces large gauge boson transverse momenta. At a center of mass energy of 630 GeV, the average gauge boson transverse momentum is approximately 7 GeV. In the absence of gluon radiation, the natural scale of the gauge boson transverse momentum would be that of the Fermi momentum of a quark in a nucleon (a few hundred MeV). Additionally, the QCD vertex corrections change the size of the cross section by a factor that is between one and two. Nevertheless, equation (3.3) correctly describes many of the features of gauge boson production and gives the correct scale of the cross section.

3.3. *W* Boson Physics

As an example of the Drell-Yan mechanism, let's consider the process $p\bar{p} \rightarrow W^{\pm} \rightarrow \ell^{\pm}\nu$. The cross section for the process $q\bar{q} \rightarrow W^{\pm} \rightarrow \ell^{\pm}\nu$ in the $q\bar{q}$ cm frame can be written as,

$$\frac{d\hat{\sigma}}{d\Omega}(q_\ell cos\theta^*) = \frac{\alpha^2}{64\sin^4\theta_w} \cdot \frac{\hat{s}}{(\hat{s}-M_W^2)^2 + \Gamma_W^2\hat{s}^2/M_W^2} \cdot (1 - q_\ell \cos\theta^*)^2, \qquad (3.4)$$

where: θ^* is the polar angle of the charged lepton relative to the quark direction; q_ℓ is the lepton charge; and Γ_W is the W boson width. The large angular asymmetry is a consequence of the V-A coupling of the W to all fermions. Note that electrons are emitted preferentially in the quark direction and positrons in the antiquark direction.

The lowest order Drell-Yan cross section for the production of the W^- boson follows from the substitution of equation (3.4) into equation (3.3),

$$\frac{d\sigma_0}{d\Omega} = \frac{1}{3}\int dx_1 dx_2 \delta(x_1x_2 - \hat{s}/s)\left[\frac{d_p(x_1)\bar{u}_{\bar{p}}(x_2)}{x_1x_2}\frac{d\hat{\sigma}}{d\Omega}(-\cos\theta^*) + \frac{\bar{u}_p(x_1)d_{\bar{p}}(x_2)}{x_1x_2}\frac{d\hat{\sigma}}{d\Omega}(\cos\theta^*)\right] \qquad (3.5)$$

where $u_h(x)$ $[d_h(x)]$ is the momentum distribution of u $[d]$ quarks in hadron h. The antiquark-antiproton distribution $\bar{u}_{\bar{p}}(x)$ is required to be identical to the quark-proton distribution $u_p(x)$ by CPT invariance. The sea quark distributions $\bar{u}_p(x)$

and $d_{\bar{p}}(x)$ are approximately equal and are unimportant except at small values of x. The angular asymmetry that is associated with the $\bar{u}_p(x_1)d_{\bar{p}}(x_2)$ factor has the opposite sense because the $q\bar{q}$ axis reverses direction with respect to the parent hadrons. Note that the delta function explicitly applies the constraint given in equation (3.1). The average value of x_1 or x_2 is therefore $x_{avg} \sim M_W/\sqrt{s}$. At larger values of x_{avg} (lower energy colliders), the valence quark distributions dominate equation (3.5) and the lepton angular asymmetry is large. As x_{avg} becomes smaller, the wrong-sign sea quark terms dilute the asymmetry.

Since the u-quark distribution of the proton is *harder* than is the d-quark distribution (there are two valence u quarks to one d quark), we expect that W^- bosons are slightly boosted in the antiproton direction, and that W^+ bosons are slightly boosted in the proton direction. The scaled longitudinal momentum distribution $x_2 - x_1$ of W^- bosons produced at $\sqrt{s} = 630$ GeV is shown in Figure 2. The average boost along the antiproton direction is fairly small, $x_2 - x_1 = 0.06$. However, the distribution is quite broad. The average value of the absolute value $|x_2 - x_1|$ is 0.22 which corresponds to an average longitudinal momentum of 68.2 GeV.

The Detection of W Bosons

As we have already discussed, there are serious QCD backgrounds to the detection and measurement of W bosons via their hadronic decays. It is necessary to search for the charged lepton-neutrino final states. The QCD background is suppressed both by the leptonic selection criteria and by the missing P_t signature of the neutrino.

The identification of charged leptons and neutrinos is greatly aided by the two-body nature of the W decay. This becomes clearer if we consider the transformation of the lepton angular distribution from the W center-of-mass frame to the laboratory frame. Let the cm angular distribution be described by some (analytic)

function f,

$$\frac{dN}{d\cos\theta^*} = f(\cos\theta^*). \tag{3.6}$$

In the laboratory frame, most of the W boson momentum is along the beam axis. Therefore, the transverse momentum distribution of the charged leptons is the same in both frames. The lepton transverse momentum P_t^ℓ has a simple relationship to the cm emission angle,

$$P_t^\ell = \frac{M_W}{2}\sin\theta^*. \tag{3.7}$$

Changing variables from $\cos\theta^*$ to P_t^ℓ, equation (3.6) becomes

$$\frac{dN}{dP_t^\ell} = \frac{1}{\sqrt{1-4P_t^{\ell 2}/M_W^2}} f(\pm\sqrt{1-4P_t^{\ell 2}/M_W^2}). \tag{3.8}$$

There is a singularity in the P_t^ℓ distribution at $M_W/2$! This so-called *Jacobian peak* (after the Jacobian of the transformation) implies that most of the leptons and neutrinos emerge with the largest transverse momenta.

The singularity in the P_t^ℓ distribution as described by equation (3.8) is unphysical and is moderated by three effects:

1. The parent W boson has a finite width, $\Gamma_W \sim 2.1$ GeV.
2. The detector has finite resolution.
3. The parent W is produced with non-zero transverse momentum.

These effects are incorporated into a simulation of the process $p\bar{p} \rightarrow W \rightarrow e\nu$ at $\sqrt{s} = 630$ GeV. The P_t^e distribution is presented for three different phenomenological W boson transverse momentum distributions in Figure 3. The average values of P_t^W are zero (the dashed curve), 7 GeV (the dashed-dotted curve), and 14 GeV (the solid curve). The energy resolution of the detector is assumed to be $\delta E/E = 0.15/\sqrt{E}$. Note that the P_t^e distribution is very sensitive to the W transverse momentum distribution.

The Jacobian peak is a feature of transverse momentum distributions of the charged leptons and of the neutrinos. Since the backgrounds that affect the identification of charged and neutral leptons decrease rapidly with increasing P_t, most experiments select W candidates by requiring that P_t^ℓ and P_t^ν be larger than 20 GeV. The electron and neutrino transverse momentum distributions for the 1203 $W \to e\nu$ event sample of the UA2 Collaboration[9] are shown in Figure 4. The background from misidentified two-jet events is estimated to be less than 1%.

In practice, W bosons are detected by their decays into $e\nu$ and $\mu\nu$ final states. The $\tau\nu$ final state cannot be detected with high efficiency (the efficiency is in the range 10%-15%). This is because a large fraction of τ decays appear as low multiplicity hadronic jets. One must use very restrictive cuts to eliminate low multiplicity QCD events. A second difficulty is that neutrinos are detected from an imbalance in the total transverse momentum of the event. Since all τ decays contain at least one neutrino, the missing P_t distribution is softened considerably. The P_t^ν requirement is therefore less efficient. Although the identification of τ lepton final states is difficult, the leptonic decays of the τ's do contaminate the $e\nu$ and $\mu\nu$ final states. For electron or muon transverse momenta above 20 GeV, the τ contamination is in the range 3%-4%.

<u>W Mass Measurement</u>

It is clear from equation (3.8) and from Figure 3 that the position of the Jacobian peak in the P_t^ℓ distribution is determined by the mass of the W boson. Figure 3 also illustrates the difficulty in the extraction of M_W from a fit to the distribution. The P_t^ℓ distribution is very sensitive to the P_t^W distribution which is neither well-known nor well-measured. The solution to this problem is to use the so-called transverse mass variable, $M_t^{\ell\nu}$. The transverse mass is the two-dimensional analog of the normal three-dimensional one,

$$M_t^{\ell\nu} \equiv \sqrt{2P_t^\ell P_t^\nu (1 - \cos\Delta\phi_{\ell\nu})} \tag{3.9}$$

where P_t^ν is the neutrino transverse momentum and $\Delta\phi_{\ell\nu}$ is the azimuthal angle

between the lepton and neutrino P_t vectors. Although M_t is not a Lorentz-invariant quantity, it is quite insensitive to the P_t^W distribution. This is shown in Figure 5. The $M_t^{e\nu}$ distributions are plotted for the three P_t^e distributions shown in Figure 3. The average values of P_t^W are zero (the dashed curve), 7 GeV (the dashed-dotted curve), and 14 GeV (the solid curve). The resolution of the neutrino P_t along the x and y axes is assumed to be $\delta P_{t,xy}^{\nu} = 0.5\sqrt{E_T}$ GeV. Note that the $M_t^{e\nu}$ distribution is very insensitive to the details of the P_t^W distribution.

Note also that the $M_t^{e\nu}$ distributions are much more sharply peaked than are the P_t^e distributions. The transverse mass should therefore be a more sensitive measure of the W mass. We can quantify this observation by analyzing the expected results of likelihood fits to the P_t^e and $M_t^{e\nu}$ distributions. Let f and g be P_t^e and $M_t^{e\nu}$ likelihood functions that are normalized in the region of sensitivity. In practice, the regions 25 GeV $< P_t^e <$ 50 GeV and 50 GeV $< M_t^{e\nu} <$ 100 GeV are used to measure M_W. The functions f and g are therefore defined as follows,

$$f(P_t^e, M_W) = \frac{\frac{dN}{dP_t^e}}{\int_{25}^{50} dP_t^e \frac{dN}{dP_t^e}} \qquad g(M_t^{e\nu}, M_W) = \frac{\frac{dN}{dM_t^{e\nu}}}{\int_{50}^{100} dM_t^{e\nu} \frac{dN}{dM_t^{e\nu}}}. \tag{3.10}$$

The M_W precision of likelihood fits to the measured distributions can be estimated from the following expressions,

$$\begin{aligned} \delta M_W &= \left[N_d \int_{25}^{50} dP_t^e \frac{\left(\frac{\partial f}{\partial M_W}\right)^2}{f} \right]^{-\frac{1}{2}} & \delta M_W &= \left[N_d \int_{50}^{100} dM_t^{e\nu} \frac{\left(\frac{\partial g}{\partial M_W}\right)^2}{g} \right]^{-\frac{1}{2}} \\ &= \frac{14}{\sqrt{N_d}} \text{ GeV} & &= \frac{8.1}{\sqrt{N_d}} \text{ GeV} \end{aligned} \tag{3.11}$$

where N_d is the number of detected events. The numerical results given in the second line are derived by numerically differentiating and integrating the $\langle P_t^W \rangle =$ 7 GeV distributions in Figures 3 and 5. Note that the transverse mass distribution has substantially more analyzing power than does P_t^e distribution. Note also that our simulation of the missing P_t resolution is somewhat optimistic. The analyzing

power of the $M_t^{e\nu}$ distribution is probably not a good as indicated by equation (3.11).

The transverse mass distribution has the advantages that it is less sensitive to the W boson P_t distribution and more sensitive to the W boson mass than is the lepton transverse momentum distribution. These advantages are the result of adding more information to the problem (the neutrino P_t). Unfortunately, the additional information is accompanied by an additional uncertainty. We must understand the resolution function for the missing P_t vector. In practice, the increase in the systematic uncertainty that is associated with the use of the P_t^ν information is more than compensated by the reduced sensitivity to the P_t^W distribution.

The shapes of the $M_t^{\ell\nu}$ and P_t^ℓ distributions near the Jacobian peaks are sensitive to the proton structure functions. The lineshape of the W resonance and the accepted lepton transverse momentum distribution are both affected by the structure functions. The lineshape is given by the convolution of the relativistic Breit-Wigner resonance form (given in equation (3.4)) with the quark structure functions (see equation (3.5)). Since the structure functions fall sharply with increasing x, the $M_t^{\ell\nu}$ and P_t^ℓ distributions are steepened above the peak values. The acceptance effect is caused by the boosting of the W along the beam axis. The acceptance for a lepton that is emitted with a *backward angle* (in the W rest frame) relative to the boost direction is larger than the acceptance for a lepton that is emitted with the symmetric forward angle. Since P_t^ℓ is completely correlated with the emission angle, the accepted P_t^ℓ and $M_t^{\ell\nu}$ distributions are sensitive to the choice of proton structure functions. The dependence of the predicted distributions upon the structure functions leads to an uncertainty on the fit value of M_W of roughly 100 MeV.

The best current measurement of the W boson mass is the one derived from the 1203 event sample of the UA2 Collaboration,[9]

$$M_W = 80.79 \pm 0.31(\text{stat}) \pm 0.21(\text{syst}) \pm 0.81(\text{scale}) \text{ GeV}.$$

The systematic error has roughly equal contributions from uncertainties on the transverse momentum resolution, the quark distribution functions, and the statistical precision of the Monte Carlo that was used to calculate the shape of the $M_t^{e\nu}$ distribution. There are smaller contributions to the systematic error from the leakage energy from the underlying event into the electron clusters, from uncertainties on the final state radiative corrections, and from the uncertainty on the electron energy resolution function. Note that the largest single uncertainty is due to the 1% energy scale uncertainty of the UA2 electromagnetic calorimeter. The error is quoted separately because it cancels in the ratio of the W and Z masses.

W Angular Distribution

We have already seen that the angular distribution of the leptons emitted in W decay is expected to be strongly asymmetric *in the $q\bar{q}$ center-of-mass frame.* It is clearly important to verify that this is indeed true for the 81 GeV particle that has been observed. Unfortunately, the $q\bar{q}$ center-of-mass frame is generally not well determined. The reasons for this are:

1. The $q\bar{q}$ axis is coincident with the $p\bar{p}$ axis only when the W is produced with zero transverse momentum. A non-zero value for P_t^W implies that one or both of the incident quarks emitted gluons in the collision process. The solution to this problem is to use the Collins-Soper definition of the $q\bar{q}$ cm frame.[10] The bisector of the proton and antiproton directions in the W rest frame is chosen as the $q\bar{q}$ axis. This definition is therefore *correct on average* but fails on an event by event basis.

2. The use of the Collins-Soper frame requires that we know the W boson rest frame. However, since the neutrino longitudinal momentum is not measured, we do not have enough information to reconstruct the W rest frame. The solution to this problem is to constrain the mass of the lepton-neutrino system to the W mass (ignoring the finite width of the W). This yields two solutions for the neutrino longitudinal momentum P_L^ν. Since the W longitudinal momentum is $P_L^W = P_L^\ell + P_L^\nu$, there are two solutions for P_L^W. In the

Collins-Soper frame, the two solutions correspond to opposite sign solutions for $\cos\theta^*$. In many cases, the W is highly boosted on the laboratory frame and one solution is unphysical ($P_L^W > \sqrt{s}/2$). These unambiguous events are normally used to measure W boson angular asymmetry.

The UA1 collaboration has performed this analysis with their old (767 nb^{-1}) sample of $W \to e\nu$ events.[11] They have used only the 149 events that have an unambiguous solution for P_L^W and a measured value of P_t^W less than 15 GeV. They correct the measured distribution for the biases that are introduced by the selection process. The resulting distribution is plotted in Figure 6. The solid curve shows the expected $(1 - q_e \cos\theta^*)^2$ distribution. It agrees well except near $q_e \cos\theta^* = 1$ where the wrong-sign sea quark contribution is large (see equation (3.5)).

3.4. Z^0 Boson Physics

The cross section for the process $p\bar{p} \to Z^0 \to \ell^+\ell^-$ can be calculated from the zeroth order Drell-Yan formalism given in equation (3.3). The cross section for the point process $q\bar{q} \to Z^0 \to \ell^+\ell^-$ is straightforward to calculate from the Standard Model couplings,

$$\begin{aligned}\frac{d\hat{\sigma}_q}{d\Omega}(c) = \frac{\alpha^2}{4\hat{s}}\Bigg\{ & Q_q^2(1+c^2) \\ & - \frac{Q_q}{2\sin^2 2\theta_w}\text{Re}\Gamma(\hat{s})\Big[vv_q(1+c^2) + 2aa_qc\Big] \\ & + \frac{1}{16\sin^4 2\theta_w}|\Gamma(\hat{s})|^2\Big[(v^2+a^2)(v_q^2+a_q^2)(1+c^2) + 8vav_qa_qc\Big]\Bigg\}\end{aligned} \tag{3.12}$$

where: $c \equiv \cos\theta^*$ is cosine of the polar angle of the lepton relative to the quark direction; $\Gamma(\hat{s}) = \hat{s}/(\hat{s} - M_Z^2 + i\Gamma_Z\hat{s}/M_Z)$ is the normalized Z propagator; Γ_Z is the Z^0 width; and where the coupling constants (defined in equation (2.2)) without subscript, v and a, refer to the leptonic couplings. The first term within the braces describes the process of pure γ exchange, the second term describes the Z^0-γ interference, and the third term describes pure Z^0 exchange. The γ

exchange term is quite small and can be ignored. The interference term vanishes at $\hat{s} = M_Z^2$ and can be ignored except when calculating the angular distribution (because $aa_q \gg vv_q$).

The lowest order Drell-Yan cross section for the Z^0 production follows from the substitution of equation (3.12) into equation (3.3),

$$\begin{aligned}\frac{d\sigma_0}{d\Omega} &= \frac{1}{3}\int dx_1 dx_2 \delta(x_1x_2 - \hat{s}/s)\cdot \\ &\left\{\frac{u_p(x_1)\bar{u}_{\bar{p}}(x_2)}{x_1x_2}\frac{d\hat{\sigma}_u}{d\Omega}(c) + \left[\frac{s_p(x_1)\bar{s}_{\bar{p}}(x_2)}{x_1x_2} + \frac{d_p(x_1)\bar{d}_{\bar{p}}(x_2)}{x_1x_2}\right]\frac{d\hat{\sigma}_d}{d\Omega}(c)\right. \\ &\left.\frac{\bar{u}_p(x_1)u_{\bar{p}}(x_2)}{x_1x_2}\frac{d\hat{\sigma}_u}{d\Omega}(-c) + \left[\frac{\bar{s}_p(x_1)s_{\bar{p}}(x_2)}{x_1x_2} + \frac{\bar{d}_p(x_1)d_{\bar{p}}(x_2)}{x_1x_2}\right]\frac{d\hat{\sigma}_d}{d\Omega}(-c)\right\}\end{aligned} \tag{3.13}$$

where $s_h(x)$ is the strange (sea) quark structure function.

Note that the angular distribution of the outgoing lepton is a function of the ratio of the rates $u\bar{u}$ annihilations and $d\bar{d}$ annihilations (because $d\hat{\sigma}_u/d\Omega$ is quite different from $d\hat{\sigma}_d/d\Omega$). Like the W case, there is also a dilution effect coming from the wrong-sign sea quarks.

Z Boson Detection

The presence of a second charged lepton makes the detection of the decay $Z^0 \to \ell^+\ell^-$ extremely straightforward for electron and muon final states. On the other hand, the detection of τ final states is quite difficult without the missing P_t signature of the W decays. At the current time, no experiment has published a signal for the process $p\bar{p} \to Z^0 \to \tau^+\tau^-$. In the case of electrons, it is necessary to require that only one of the *legs* of the Z candidate satisfy very restrictive identification criteria. Taking all lepton pair masses between 60 and 120 GeV, the background from misidentified hadronic events is typically less than 1%.

Measurement of M_Z

The mass of the Z boson is extracted from the observed lepton-lepton mass ($M_{\ell\ell}$) distribution. The observed $M_{\ell\ell}$ distribution is the convolution of the underlying Breit-Wigner lineshape, the quark structure functions, and the experimental

resolution. The leptonic daughters of the Z are sufficiently energetic that the energy resolution associated with electromagnetic calorimeters ($\delta E/E \sim 0.15/\sqrt{E}$) is better than that associated with magnetic spectrometers ($\delta(1/P_t) \sim 0.001$ GeV^{-1}) by roughly a factor of two. We therefore expect the electron final states to offer better statistical analyzing power than do the muon final states. We can quantify the difference by comparing the expected results of fits to the M_{ee} and $M_{\mu\mu}$ distributions. Let $z(M_{\ell\ell}, M_Z)$ be the likelihood function for the observed lepton pair mass distribution normalized over the interval 60 GeV $< m_{\ell\ell} <$ 120 GeV,

$$z(M_{\ell\ell}, M_Z) \equiv \frac{\frac{dN}{dM_{\ell\ell}}}{\int_{60}^{120} dM_{\ell\ell} \frac{dN}{dM_{\ell\ell}}}. \tag{3.14}$$

The M_Z precision of a likelihood fit to the measured distribution can then estimated from the following expression,

$$\delta M_Z = \left[N \int_{60}^{120} dM_{\ell\ell} \frac{\left(\frac{\partial z}{\partial M_Z}\right)^2}{z} \right]^{-\frac{1}{2}} = \begin{cases} \frac{2.9}{\sqrt{N}} \text{ GeV}, & \text{for electrons} \\ \frac{4.1}{\sqrt{N}} \text{ GeV}, & \text{for muons} \end{cases} \tag{3.15}$$

where N is the number of detected events. The electrons are expected to be better by roughly 30%.

In practice, only well-measured lepton pairs are used to extract M_Z. The existing experiments are well instrumented only at relatively large values of polar angle ($|\theta| \gtrsim 20°$). The probability that both leptons are detected in this region is about 70% at $\sqrt{s} = 630$ GeV and 47% at $\sqrt{s} = 1800$ GeV. The magnetically measured masses of 123 muon pairs and 65 electron pairs of the CDF collaboration[12] are shown in Figure 7. Although the momentum resolution of the CDF magnetic spectrometer is inferior to the energy resolution of the CDF calorimeter, the momentum/energy scale is more precisely known (an uncertainty of 0.22% is claimed). The magnetic spectrometer is used to directly measure the muon pair masses and to calibrate the electromagnetic calorimeter with low energy electrons (from b quark decay). Performing likelihood fits to the 123 μ-pair sample and to a

sample of 73 calorimetrically measured electron pairs, the following the measurements of M_Z were obtained,

$$M_Z = 90.7 \pm 0.4 \text{ (stat)} \pm 0.2 \text{ (syst) GeV (muons)}$$
$$M_Z = 91.1 \pm 0.3 \text{ (stat)} \pm 0.4 \text{ (syst) GeV (electrons).}$$

The systematic error on the muon result is dominated by the momentum scale uncertainty of the magnetic spectrometer. The systematic error quoted for the electron measurement is due largely to uncertainties in the calorimeter calibration. The combined result is

$$M_Z = 90.9 \pm 0.3 \text{ (stat + syst)} \pm 0.2 \text{ (scale) GeV}$$

where the scale uncertainty has been quoted separately.

The UA2 Collaboration have also recently published a result that is based upon a sample of 90 electron pair events,[9]

$$M_Z = 91.49 \pm 0.35(\text{stat}) \pm 0.12(\text{syst}) \pm 0.92(\text{scale}) \text{ GeV},$$

where dominant contributions to the systematic error are due to leakage of energy from the underlying event into the electron clusters and to uncertainties in the detector response to the process $Z^0 \rightarrow e^+e^-\gamma$.

3.5. M_W, M_Z AND THE STANDARD MODEL

The ratio of the W and Z boson masses is an interesting quantity for very practical reasons. We have seen that lepton energy scale uncertainties lead to substantial uncertainties on the gauge boson masses. These particular uncertainties cancel in the ratio M_W/M_Z. Since M_Z has been precisely measured in e^+e^- experiments (which cannot measure M_W at the current time), the electroweak information contained within M_W is also contained within the mass ratio.

The best measurement of M_W that is currently available is contained within the M_W/M_Z measurement of the UA2 Collaboration,[9]

$$\frac{M_W}{M_Z} = 0.8831 \pm 0.0048(\text{stat}) \pm 0.0026(\text{syst}).$$

Taking the current weighted world average value[8] for M_Z ($M_Z = 91.160 \pm 0.0029$ GeV), they quote a rescaled W mass value of,

$$M_W = 80.49 \pm 0.43(\text{stat}) \pm 0.24(\text{syst}) \text{ GeV}.$$

The ratio M_W/M_Z directly determines the parameter $\sin^2\theta_w$ as defined by Sirlin,[13]

$$\sin^2\theta_w \equiv 1 - \left(\frac{M_W}{M_Z}\right)^2 = 0.220 \pm 0.008(\text{stat}) \pm 0.005(\text{syst}).$$

The Sirlin definition of $\sin^2\theta_w$ is related to the Z^0 mass by a very well-known expression,[14]

$$M_Z^2 = \frac{A^2}{(1-\Delta r)\sin^2\theta_w \cos^2\theta_w}, \tag{3.16}$$

where Δr contains the effects of electroweak radiative corrections ($\Delta r = 0$ at tree level), and A is a constant,

$$A = \left[\frac{\pi\alpha}{\sqrt{2}G_F}\right]^{\frac{1}{2}} = 37.2805 \pm 0.0003 \text{ GeV}.$$

Using the SLC/LEP value for M_Z and their own result for M_W/M_Z, the UA2 group derive a result for Δr,

$$\Delta r = 0.026^{+0.029}_{-0.032}.$$

Their result is consistent with a large value of m_{top} (100-200 GeV).

3.6. Future Measurements of M_W and M_Z

We have seen that the mass ratio M_W/M_Z has the advantage that the uncertainty on the leptonic energy scale cancels in the ratio. The remaining systematic errors are due largely the differences in the techniques that are used to extract the masses. These techniques have been developed to minimize the statistical error of the result. The Tevatron experiments expect to accumulate significantly larger data samples in the next few years (the current CDF sample could increase by a factor of order fifty). The increased size of the samples should be adequate to saturate the current systematic errors.* One must therefore ask if it is possible to reduce the systematic uncertainties by using techniques with less statistical sensitivity.

The obvious approach is to extract the Z mass from the transverse mass technique. In this case, the uncertainties associated with the P_t^ν resolution, the underlying event, and the electron energy resolution would largely cancel in the mass ratio. The remaining uncertainties would be those due to the differences in radiative corrections and structure functions.

The question of whether to discard one leg of a Z event has been much discussed (over coffee). It is clear that a strong correlation exists between the transverse momenta of the two leptons. It would be difficult to assess the effect of the correlation on the result. However, it is very likely that this question will remain academic. In the current experiments, the number of Z candidates with two well-measured legs is somewhat smaller than the number with only one well-measured leg (the CDF group uses 73 well-measured electron pairs to determine M_Z and 193 events with one well-measured leg to determine the Z cross section[15]). The use of second well-measured legs would therefore add only a small statistical advantage (in the CDF example, the statistical error would be improved by only 17%).

Scaling the current CDF samples[15] of $W \to e\nu$ candidates (1828 events) and

* It would also permit the detailed study and reduction of the current systematic errors. For instance, a large sample of Z^0 decays should help understand the missing P_t resolution from the study of the hadronic system that recoils against the (well-measured) lepton pair.

one-legged $Z \rightarrow ee$ events (193) by a factor of 50, we can use equation (3.11) to estimate the statistical error on M_W/M_Z that might be achieved in the future. Assuming that only one leg from each Z event is used, we estimate the error on the ratio to be

$$\delta\left(\frac{M_W}{M_Z}\right) \sim 0.0009.$$

Assuming that M_Z is known to 30 MeV, this corresponds to an error on M_W of 83 MeV. It is clear than a 100-150 MeV measurement of M_W is possible if the remaining systematic error can be controlled to a comparable level.

3.7. The Z^0 Angular Distribution

The angular distribution of the leptons in the $q\bar{q}$ center-of-mass frame is given by equations (3.12) and (3.13). Although the net expression is fairly complicated, it has the following form,

$$\frac{d\sigma}{d\Omega^*} = \frac{A}{2}(1+\cos^2\theta^*) + B\cos\theta^* \tag{3.17}$$

where the complexity is hidden in the definitions of the constants A and B. If the initial state hadrons were monoenergetic quarks of energy $M_Z/2$, we could write A and B as

$$\begin{aligned} A &= \frac{\alpha^2}{512\sin^4 2\theta_w}\cdot\frac{1}{\Gamma_Z^2}\cdot 2(v^2+a^2)(v_q^2+a_q^2) \\ B &= \frac{\alpha^2}{512\sin^4 2\theta_w}\cdot\frac{1}{\Gamma_Z^2}\cdot 8vav_qa_q. \end{aligned} \tag{3.18}$$

It is often quite useful to consider the so-called *forward-backward asymmetry* which measures the ratio of the B and A terms. It is defined as follows,

$$\begin{aligned} A_{FB}(x) &\equiv \frac{\int_0^x d\cos\theta^* \frac{d\sigma}{d\cos\theta^*} - \int_{-x}^0 d\cos\theta^* \frac{d\sigma}{d\cos\theta^*}}{\int_{-x}^x d\cos\theta^* \frac{d\sigma}{d\cos\theta^*}} \\ &= \frac{4x}{3+x^2}\cdot\frac{3}{4}\cdot\frac{B}{A} = F(x)\cdot\frac{3}{4}\cdot\frac{B}{A} \end{aligned} \tag{3.19}$$

where x is an integration limit and the function $F(x)$ is normalized such that

$F(1) = 1$. The forward-backward asymmetry is the ratio of the difference in the cross sections for finding the lepton in the quark and antiquark hemispheres to the total cross section. The effect of limited detector acceptance in polar angle is described by the function $F(x)$ where x is the maximum value of $\cos\theta^*$. By convention, the symbol A_{FB} describes the asymmetry for complete polar angle coverage ($A_{FB} = A_{FB}(1)$).

The forward-backward asymmetry is sensitive to the couplings of the Z^0 to incident quarks and the final state leptons. For the simple example of monoenergetic quarks of energy $M_Z/2$, the asymmetry has the form,

$$A_{FB} = \frac{3}{4} \cdot \frac{-2va}{v^2 + a^2} \cdot \frac{-2v_q a_q}{v_q^2 + a_q^2} = \begin{cases} 0.063 & \text{for } u\text{-quarks} \\ 0.089 & \text{for } d\text{-quarks} \end{cases} \tag{3.20}$$

where we have assumed that $\sin^2\theta_w = 0.234$. Note that the lepton and quark vector coupling constants are sensitive functions of $\sin^2\theta_w$ (see equation (2.2)). The Z^0 forward-backward asymmetry is therefore useful for testing the Standard Model.

The actual $p\bar{p}$ initial state is a mixture of $u\bar{u}$ and $d\bar{d}$ states. The measured asymmetry should therefore fall between the above extremes (as determined by the u and d quark structure functions and by the quark couplings to the Z^0). Or should it? We expect that a number of effects should reduce the measured asymmetry:

1. As in the case of the W angular distribution, there are *wrong-sign* sea-quark pairs that dilute the asymmetry. Note that a correct analysis of this effect depends upon a good knowledge of the low-x quark structure functions.

2. The electroweak interference terms are important when $\hat{s} \neq M_Z^2$. This effect is also sensitive to the quark structure functions.

3. The acceptance of a real experiment is finite ($x < 1$). The actual acceptance depends upon the longitudinal momentum distribution of the Z which is sensitive to the quark structure functions.

4. The actual $q\bar{q}$ axis is unknown. Although we can use the average direction (the Collins-Soper definition), there will be an inevitable dilution of the asymmetry.

It appears that the measured value of A_{FB} might be quite sensitive to uncertainties in the quark structure functions of the proton. To investigate the above effects, we have performed a Monte Carlo simulation with several different sets of structure functions. It is assumed that our experiment can reconstruct leptons with polar angles larger than 20°. We find that the reconstructed value of A_{FB} is 0.050 ± 0.002 where the uncertainty reflects the variation of the result with structure function parameterizations. This result does not vary between Sp$\bar{\text{p}}$S and Tevatron energies. Given our list of structure function dependent dilution effects, the uncertainty seems remarkably small. Note that our simulation does not include the correct mechanism for the generation of Z^0 transverse momentum. The smearing of the angular distribution due to the initial state gluon bremsstrahlung (which produces non-zero P_t^Z) is not correctly simulated. This may result in a large uncertainty in the reconstructed asymmetry. The sensitivity of the resolved asymmetry to variations in $\sin^2\theta_w$ is given by the following expression,

$$\delta \sin^2\theta_w = \frac{1}{3.7} \cdot \delta A_{FB}. \tag{3.21}$$

The only measurement of A_{FB} that is currently in print was performed by the UA1 Collaboration[11] with 33 events,

$$A_{FB} = \frac{3}{4} \cdot (0.06 \pm 0.24) = 0.045 \pm 0.18$$

which they convert into a measurement of $\sin^2\theta_w$,

$$\sin^2\theta_w = 0.24^{+0.05}_{-0.04}.$$

It is likely that CDF will be able to produce a measurement in the near future

with a precision,

$$\delta A_{FB} \sim \frac{1}{\sqrt{N}} \sim 0.07$$

where N is the number of Z candidates. The corresponding precision on $\sin^2\theta_w$ would be approximately $\delta\sin^2\theta_w \sim 0.020$.

Although neither the UA1 nor the likely CDF results are likely to be very significant, future high-luminosity measurements could reach the $\delta\sin^2\theta_w \sim 0.003$ level if the uncertainty associated with the $q\bar{q}$ axis can be controlled.

LECTURE II

4. Experiments at Electron-Positron Colliders

During the last year, two high energy electron-positron colliders have begun operation. The SLAC Linear Collider (SLC) began physics operation in April of 1989 and had produced a sample of about 600 Z^0 events by early 1990. The LEP project began operation in October of 1989 and had produced samples of approximately 30,000 Z^0 events in each of four detectors by early 1990. The current and future parameters of the two machines are summarized in Table V.

Table V

Machine	Date	Energy	Peak Luminosity
SLC	1989	$\lesssim 100$ GeV	$\sim 1.4\times10^{28}\text{cm}^{-2}\text{sec}^{-1}$
SLC	1992	$\lesssim 100$ GeV	$\sim 6\times10^{29}\text{cm}^{-2}\text{sec}^{-1}$
LEP I	1989	$\lesssim 100$ GeV	$\sim 2\times10^{30}\text{cm}^{-2}\text{sec}^{-1}$
LEP I	1990	$\lesssim 100$ GeV	$\sim 1\times10^{31}\text{cm}^{-2}\text{sec}^{-1}$
LEP II	1994?	$\lesssim 200$ GeV	$\sim 3\times10^{31}\text{cm}^{-2}\text{sec}^{-1}$

The luminosity of the SLC is expected to improve by a factor of approximately forty in the next two years. The SLC has a spin polarized electron source that is expected to provide a 40% degree of polarization at the beam collision point. The polarized electron beam should begin operation during 1990. The LEP machine was operated routinely at 20% of its design luminosity during its first run. It seems likely that the design luminosity of 10^{31} $\text{cm}^{-2}\text{sec}^{-1}$ will be achieved during the next year. Although there are serious plans to produce longitudinally polarized beams in LEP, it appears to be difficult to achieve a high degree of longitudinal polarization ($\gtrsim 30\%$) with good luminosity. In the longer term, the energy of LEP will be upgraded to a value above the threshold for W pair production.

4.1. Experimental Details

There are a total of six experiments that are currently operating at or being prepared for SLC and LEP. At the SLC, the Mark II detector is currently in operation and will be replaced by the SLD detector later this year. There are four active experiments at the LEP collider: ALEPH, DELPHI, L3, and OPAL. A complete description of the six detectors would be extremely tiresome. All of them share the a number of common features and capabilities:

1. High Resolution Magnetic Spectrometers - all of the experiments contain charged particle tracking systems that are immersed in magnetic fields. They are capable of reconstructing track directions and transverse momenta. The transverse momentum resolution is typically $\delta P_t/P_t \sim$(0.001-0.002)$\cdot P_t$ (where P_t is in GeV) in the region of polar angle $|\cos\theta| < 0.8$.

2. Electromagnetic Calorimetry - all of the experiments have electromagnetic calorimeters. These range from gas sampled devices with resolutions $\delta E/E \sim 0.30/\sqrt{E}$ (E in GeV) to lead glass and BGO calorimeters with sub-percent resolutions over a large range of energies.

3. Muon Spectrometers/Identifiers - all of the experiments except L3 have magnetized iron shielding for the identification and measurement of muon tracks. The momentum resolution of these systems is poor as compared with the inner tracking systems mentioned above. The L3 detector handles muons in an *inside-out* manner. The muon identification is achieved by penetration of the unmagnetized hadron calorimeter. The muons are momentum analyzed in a huge magnetic spectrometer that is external to the identification shielding and has much higher momentum resolution than the internal tracking system.

4. Vertex Detectors - since the Z^0 is a fairly copious source of b and c quarks, all of the experiments have high precision tracking systems at small radius. The resolution of these systems is typically a few 10's of microns per track measurement.

5. Triggers - since the total (accepted) cross section in an e^+e^- experiment is quite small, a trigger is necessary to find bunch crossings that contain events. The SLC and LEP experiments all contain electronic hardware that can find drift chamber tracks and calorimeter energy depositions during the interval between bunch crossings (22.5 μsec at LEP, 8.3 msec at SLC). Typically, any event containing two or more charged tracks or a calorimeter energy deposition larger than approximately 5 GeV is recorded.

6. Specialties - in addition to the common elements, most of the experiments have some special strengths and features. The following is a partial list:

   (a) Ring Imaging Cerenkov Devices - DELPHI and SLD use ring imaging Cerenkov devices to identify long-lived hadrons.

   (b) High Resolution Vertexing - Mark II and SLD make use of the small SLC beam and the small SLC vacuum chamber with very high resolution microvertex detectors.

   (c) Muon Measurement - as already mentioned, L3 has been optimized for the measurement of muon final states.

   (d) DE/DX - the ALEPH and DELPHI have time projection chambers as their primary tracking systems. These devices are capable of very good measurements of the charged-particle energy loss due to ionization of the chamber gas. This information can be used to identify long-lived charged particles at low momentum.

   (e) Hadron Calorimetry - the SLD calorimeter is expected to have good energy resolution for hadronic final states.

The Electron-Positron Environment

Unlike the situation with hadron colliders, the most copious processes in a high energy e^+e^- collider are also the most interesting ones. The signatures and relative sizes of the various processes are indicated in Table VI. The most serious background to Z^0 production is due to the various two-photon processes. The

two-photon background is rather trivial to remove from the data sample (a total energy cut is sufficient to suppress it by several orders of magnitude).

Table VI

Event Type	Signature	$\sigma(\sqrt{s} = M_Z)$
$e^+e^- \to Z^0 \to$ hadrons	2-3 jets $\gtrsim 20$ charged tracks	~30 nb
$e^+e^- \to e^+e^-$ (small angle)	45 GeV clusters in small angle *tagger*	~50-200 nb (dep on acceptance)
$e^+e^- \to e^+e^-\ell^+\ell^-$ $e^+e^- \to e^+e^-h^+h^-$	Transversely balanced low energy track pairs	~7-8 nb (dep on acceptance)
$e^+e^- \to Z^0 \to \mu^+\mu^-$	back-to-back high energy tracks	~1.5 nb
$e^+e^- \to Z^0 \to \tau^+\tau^-$	acolinear track pairs 1-3 combinations	~1.5 nb

4.2. Mass and Width of the Z^0

We have already discussed the importance of a high precision measurement of the mass of the Z^0. The width of the Z^0 has a tree-level dependence upon the parameters of the Standard Model and the particle content of the theory. The total width is the sum of the partial widths for the decay into each fermion-antifermion final state,

$$\Gamma_Z = \sum_f \Gamma_{f\bar{f}} = \frac{G_F M_Z^3}{24\pi\sqrt{2}} \sum_f C_f (v_f^2 + a_f^2), \tag{4.1}$$

where $\Gamma_{f\bar{f}}$ is the partial width for the decay $Z^0 \to f\bar{f}$ and the constant C_f is defined as

$$C_f = \begin{cases} 1 + \frac{3\alpha}{4\pi} Q_f^2 & \text{for leptons} \\ 3 \cdot \left[1 + \frac{3\alpha}{4\pi} Q_f^2 + \frac{\alpha_s}{\pi}\right] & \text{for quarks.} \end{cases}$$

Note that the expression of each partial width in terms of M_Z has the advantage that the m_{top} and m_{Higgs} dependences are minimized. The partial widths for a

generation of quarks and leptons are listed in Table VII. The last line shows the expected total width for three lepton flavors and five quark flavors. A small phase space suppression factor is included for the $b\bar{b}$ final state.

Table VII

Final State	$\Gamma_{f\bar{f}}$
$\nu\bar{\nu}$	166 MeV
$\ell^+\ell^-$	83 MeV
$u\bar{u}$	297 MeV
$d\bar{d}$	383 MeV
2.75 Generations	2.481 GeV

The actual measurement of M_Z and Γ_Z is made by measuring the cross section for the process $e^+e^- \rightarrow Z^0 \rightarrow f\bar{f}$ for a number of center-of-mass energies about the Z^0 pole. The theoretical Z lineshape is then fit to the measured cross section points to extract the desired parameters. This technique is illustrated in Figure 8 which shows the result of an actual measurement by the Mark II Collaboration.[3]

The theoretical lineshape was discussed in great detail by Michael Peskin in a lecture at this institute.[16] He showed that the tree-level lineshape for the process $e^+e^- \rightarrow Z^0 \rightarrow f\bar{f}$ is well-approximated by a relativistic Breit-Wigner form,

$$\sigma_f^0(s) = \frac{12\pi}{M_Z^2} \cdot \frac{s\Gamma_{ee}\Gamma_{f\bar{f}}}{(s - M_Z^2)^2 + \Gamma_Z^2 s^2/M_Z^2}. \tag{4.2}$$

Equation (4.2) does not apply to the process $e^+e^- \rightarrow e^+e^-$ which occurs via both s-channel and t-channel subprocesses.

The electron and positron radiate real photons rather copiously in a hard collision. The lineshape is strongly affected by the initial state radiation. This effect can be treated in a Drell-Yan-like formalism by introducing an electron structure function. The electron structure function $D(x, s)$ is defined as the probability that an electron (positron) radiates a fraction $1 - x$ of its initial energy during the

collision (of cm energy $\sqrt{s}$).* The radiatively corrected cross section can then be written as,

$$\sigma_f(s) = \int dx_1 dx_2 D(x_1, s) D(x_2, s) \sigma_f^0(\hat{s} = x_1 x_2 s), \tag{4.3}$$

where x_1 and x_2 the electron and positron energy fractions. The leading term of the electron structure function has the form,

$$D(x, s) \simeq \frac{\beta}{2}(1-x)^{\frac{\beta}{2}-1}, \tag{4.4}$$

where the dimensionless constant β is the effective number of radiation lengths for the process,

$$\beta \equiv \frac{2\alpha}{\pi}\left[\ln\left(\frac{s}{m_e^2}\right) - 1\right] \simeq 0.11.$$

The effect of the convolution described in equation (4.3) is to reduce the peak cross section by ~25% and to shift the peak of the cross section by roughly 120 MeV from the pole position.

It is convenient to write the radiatively corrected cross section in a form that is close to the underlying Breit-Wigner form,

$$\sigma_f(s) = \frac{12\pi}{M_Z^2} \cdot \frac{s\Gamma_{ee}\Gamma_{f\bar{f}}}{(s - M_Z^2)^2 + \Gamma_Z^2 s^2 / M_Z^2} \cdot [1 + \delta_{RC}(s)], \tag{4.5}$$

where the effects of the radiative corrections are contained in $\delta_{RC}(s)$. Using equation (4.1), we can expression all of the quantities that appear in equation (4.5) in terms of a single parameter, M_Z. Note that this choice of parameters minimizes the sensitivity of the lineshape to higher-order terms in m_{top} and m_{higgs}.

Equation (4.5) is the basis for the measurement of a number of Z resonance parameters. The analysis is usually performed with several sets of constraints:

---

* Note that the electron structure function is defined as a number distribution unlike the hadron structure functions which are defined as normalized momentum distributions. The e^+e^- cross sections therefore lack the factors of x^{-1} that appear in the hadronic cross sections.

1. All resonance parameters are constrained to their Standard Model values. In this case, the only free parameter is M_Z. The measurement can be performed with any or all of the final states (the e^+e^- final states must be excluded or fit to the correct form).

2. The visible partial widths are constrained to their Standard Model values and the invisible width is allowed to vary as a free parameter. The total width Γ_Z is decomposed into visible and invisible portions,

$$\begin{aligned} \Gamma_Z &= \sum \Gamma_{q\bar{q}} + 3\Gamma_{\ell^+\ell^-} + 3\Gamma_{\nu\bar{\nu}} \\ &= \Gamma_{vis} \qquad\qquad\quad + \Gamma_{inv}, \end{aligned} \tag{4.6}$$

   where the visible width Γ_{vis} contains all hadronic final states and all charged lepton pairs, and Γ_{inv} contains the neutrino decays and any additional unobserved particles. Any or all of the final states can be used to perform the measurement (with the usual caveat about electrons). The data are therefore fit to a function of two parameters (M_Z and Γ_{inv}),

$$\sigma_f(s) = \frac{12\pi}{M_Z^2} \cdot \frac{s\Gamma_{ee}\Gamma_{f\bar{f}}}{(s-M_Z^2)^2 + (\Gamma_{vis}+\Gamma_{inv})^2 s^2/M_Z^2} \cdot [1+\delta_{RC}(s)]. \tag{4.7}$$

3. The resonance parameters of the total hadronic cross section are not constrained to their Standard Model values. The hadronic cross section is described by the model-independent form,

$$\sigma_{had}(s) = \frac{s\Gamma_Z^2\sigma^0_{had}}{(s-M_Z^2)^2 + \Gamma_Z^2 s^2/M_Z^2} \cdot [1+\delta_{RC}(s)], \tag{4.8}$$

   where the free parameters are: M_Z, Γ_Z, and the tree-level hadronic peak cross section σ^0_{had}. The Standard Model prediction for the tree-level peak cross section is,

$$\sigma^0_{had} = \frac{12\pi}{M_Z^2} \cdot \frac{\Gamma_{ee}\Gamma_{had}}{\Gamma_Z^2} \simeq 41.5 \text{ nb}^{-1}. \tag{4.9}$$

4. None of the partial widths given in equation (4.5) are constrained to their Standard Model values. This analysis is most elegantly performed by fitting

the hadronic and leptonic final states separately but simultaneously. If the electron final states (and the appropriate lineshape) are not used, it is necessary to invoke lepton universality, $\Gamma_{ee} = \Gamma_{\mu\mu} = \Gamma_{\tau\tau}$. Assuming universality, the fit involves four parameters (M_Z, Γ_Z, Γ_{had}, and $\Gamma_{\ell\ell}$).

Scanning Theory

A hadron collider gives the experimenter a free energy scan. The hadron structure functions are quite broad in that reasonable quark-quark luminosity is produced over a large range of energies. The electron structure functions have an integrable singularity at $x = 1$. Most of the e^+e^- luminosity is produced near the nominal value of $\sqrt{s}$. The experimenter can therefore choose the most efficient energy scan to optimize the measurement he/she wishes to measure. Note that an optimal scanning strategy requires some *a priori* knowledge of the parameters that one desires to measure. In the earliest runs of the SLC, the Z^0 mass was not well known and it was necessary to search for an enhancement in the event rate. Once M_Z became somewhat constrained, it was possible to choose very efficient operating points. The presence of the Standard Model as a predictor of widths and couplings made this task much easier.

Let us consider a hypothetical scan of N energy-luminosity points:

$$E_b = E_1, E_2, ..., E_N$$
$$\int \mathcal{L}dt = L_1, L_2, ..., L_N.$$

We assume that a cross section σ_i is measured at each point,

$$\sigma_{measured} = \sigma_1, \sigma_2, ..., \sigma_N.$$

The M parameters a_j $(j = 1, M)$ of our theoretical lineshape $\sigma(E)$ can be

extracted from a χ^2 fit to the measured points. The quantity χ^2 is defined as,

$$\chi^2 \equiv \sum_{i=1}^{N} \frac{[\sigma_i - \sigma(E_i)]^2}{(\delta\sigma_i)^2}, \tag{4.10}$$

where $\delta\sigma_i$ is the error on the i^{th} measurement.

The best estimate of the parameters $(\bar{a}_j)$ is the one that minimizes χ^2. The parameter errors are found from a Taylor expansion of χ^2 about the minimum value,

$$\begin{aligned} \chi^2 &= \chi^2(\bar{a}) + \frac{1}{2}\sum_{j,k=1}^{M} \frac{\partial^2\chi^2}{\partial a_j \partial a_k}(a_j - \bar{a}_j)(a_k - \bar{a}_k) \\ &= \chi^2(\bar{a}) + \sum_{j,k=1}^{M} (\mathbf{C}^{-1})_{jk}(a_j - \bar{a}_j)(a_k - \bar{a}_k) \end{aligned}, \tag{4.11}$$

where the matrix $\mathbf{C^{-1}}$ is the inverse of the parameter covariance matrix. The error hyperellipsoid is determined by changing χ^2 by one unit about the minimum value. It is straightforward to show that the parameter errors are given by the diagonal elements of the covariance matrix $\mathbf{C}$,

$$(\delta a_j)^2 = \mathbf{C}_{jj}. \tag{4.12}$$

Averaging equation (4.11) over many experiments, the inverse matrix can be expressed in the following form,

$$(\mathbf{C}^{-1})_{jk} = \sum_{i=1}^{N} \frac{1}{(\delta\sigma_i)^2} \cdot \left[\frac{\partial\sigma}{\partial a_j}(E_i)\right] \cdot \left[\frac{\partial\sigma}{\partial a_k}(E_i)\right]. \tag{4.13}$$

Although equation (4.13) is quite general, it is useful to express the cross section errors in terms of the luminosity and the theoretical cross section. Ignoring the

statistical errors on the luminosity measurements,* we can express the cross section errors as $(\delta\sigma_i)^2 = \sigma(E_i)/L_i$. Equation (4.13) can then be written as,

$$(\mathbf{C}^{-1})_{jk} = \sum_{i=1}^{N} \frac{L_i}{\sigma(E_i)} \cdot \frac{\partial\sigma}{\partial a_j}(E_i) \cdot \frac{\partial\sigma}{\partial a_k}(E_i) = \sum_{i=1}^{N} L_i \cdot S(E_i, a_j) \cdot S(E_i, a_k), \quad (4.14)$$

where we define the so-called *sensitivity function* $S(E, a_j)$ as

$$S(E, a_j) \equiv \frac{1}{\sqrt{\sigma(E)}} \cdot \frac{\partial\sigma}{\partial a_j}(E). \quad (4.15)$$

If the lineshape is a function of a single parameter or if the off-diagonal elements of the inverse matrix $\mathbf{C}^{-1}$ are small, the parameter errors have a particularly simple form,

$$(\delta a_j)^{-2} \simeq \sum_{i=1}^{N} L_i \cdot \Big[S(E_i, a_j)\Big]^2. \quad (4.16)$$

Equation (4.16) *implies that the error* δa_j *is minimized when the integrated luminosity is concentrated in regions of scan energy where* $|S(E, a_j)|$ *is large.* Note that $|S(E, a_j)|$ is large where the derivative $|\partial\sigma/\partial a_j|$ is large and where the cross section is small.

The correlations between the parameters are described by the off-diagonal elements of the matrices $\mathbf{C}^{-1}$ and $\mathbf{C}$ (the error ellipsoid is unrotated if they vanish). *The presence of non-zero correlation always increases a parameter error beyond the value given in equation* (4.16).† It is clearly important to minimize the off-diagonal elements by our choice of the scan point luminosities.

Equations (4.14) and (4.12) predict the complete parameter error matrix in terms of the theoretical lineshape and the scan point luminosities. *Note that it is assumed that* χ^2 *is well-defined* ($N > M$) *and that a sufficient number of events is collected at each point that the errors are Gaussian.*

⋆ This assumption is quite valid for the measurement of non-resonant cross sections.

† The presence of non-zero correlation allows the error associated one parameter to *leak* into the error associated with another parameter.

Since any cross section measurement has an associated normalization uncertainty, it is important to consider the sensitivity of the final result to systematic shifts in the measured cross sections. Expanding the theoretical cross section in parameter space about the best estimates $\bar{a}_j$, it is straightforward to derive the average shift in a parameter Δa_j caused by shifts in the measured cross sections $\Delta\sigma_i$,

$$\langle \Delta a_j \rangle = \sum_{k=1}^{M} \mathrm{C}_{jk} \cdot \sum_{i=1}^{N} L_i \cdot \frac{\Delta\sigma_i}{\sigma_i} \cdot \frac{\partial\sigma}{\partial a_k}(E_i). \tag{4.17}$$

It is clear that we would like to choose the energies and luminosities to minimize the parameter errors and the correlations between the parameters. We can be guided in this task by examining the energy dependence of the functions $S(E, a_j)$.

As an example of the usefulness of the sensitivity functions, let us consider the measurement of the model-independent parameters of the hadronic cross section. For simplicity, we assume that values of M_Z, Γ_Z, and $\sigma^0_{had}(M_Z^2)$ are 91 GeV, 2.5 GeV, and 40 nb, respectively. The sensitivity functions for M_Z, Γ_Z, and $\sigma^0_{had}(M_Z^2)$ are plotted in Figures 9-11 as functions of $E - M_Z$. The maximum sensitivity to M_Z occurs at the scan energies -0.8 GeV and +1.0 GeV about the pole. Note that there is little sensitivity to Γ_Z at these points. The maximum sensitivity to Γ_Z occurs at points that are approximately ± 2 GeV about the pole. If we choose our energy-luminosity points symmetrically about the pole, the sum of the products $S(E_i, M_Z) \cdot S(E_i, \Gamma_Z)$ will tend to cancel since $S(E, M_Z)$ is odd about the pole and $S(E, \Gamma_Z)$ is even about the pole. The maximum sensitivity to σ^0_{had} occurs at the pole. The same odd-even effect that cancels the M_Z-Γ_Z correlation will cancel the M_Z-σ^0_{had} correlation. The Γ_Z-σ^0_{had} correlation cannot be cancelled by a choice of scan energies. However, it is not intrinsically large since $S(E, \Gamma_Z)$ is small in the energy region where $S(E, \sigma^0_{had})$ is large.

In general, a scan strategy that is based upon equations (4.14) and (4.12) is a problem in linear programming. The scan planner must decide how important various parameters are and what constraints must be satisfied. Nevertheless, fairly

simple considerations lead to the conclusion that a minimal Z-pole scan should include points at 0, ± 1, and ± 2 GeV about the pole.

Event Selection

The selection of hadronic and leptonic events was done by the five experiments with five different sets of criteria. While these criteria differ in detail, they do contain a number of common features. The selection of hadronic events usually involves the following requirements:

1. The event is required to contain five or more charged tracks. This requirement is sometimes relaxed to three or more tracks. In this case, one must be careful to exclude $\tau^+\tau^-$ events from the sample.

2. The event is required to have a visible energy (track momenta and/or calorimeter energy) that is larger than 10% of the center-of-mass energy. The principal reason for this requirement is to suppress two-photon events.

3. Most of the analyses require that substantial energy be observed in both hemispheres about the detector midplane (polar angle $\theta = 90°$). This requirement suppresses beam-gas events.

4. The time of the event must be consistent with the time of a beam crossing (to suppress cosmic ray events).

The detection efficiency for hadronic events is typically $\sim$95% with an uncertainty of 0.5-1%. The residual background contamination is typically at level of a few parts in 10^3 (mostly from $\tau^+\tau^-$ events).

Leptonic events are selected by a set of criteria that are similar to the following:

1. Electron Final States

   (a) The event is required to have two tracks. Some analyses require that the acolinearity angle be less than 5°.

   (b) There must be energy depositions in the electromagnetic calorimeters that match the tracks (spatially and/or in energy-momentum). The

total energy of the calorimeter clusters must be a large fraction ($\gtrsim 80\%$) of the center-of-mass energy.

2. Muon Final States

   (a) The event is required to have two tracks. Some analyses require that the acolinearity angle be less than 5°. The momenta of each track must be $\gtrsim 60\%$ of the beam momentum.

   (b) The energy deposition in the calorimeter that is associated with each track must be consistent with the passage of a minimum ionizing particle.

   (c) At least one track is required to penetrate the muon shielding and be detected in the outer tracking system.

3. Tau Final States

   (a) The event is required to have a visible energy that is larger than $\sim$10% of the center-of-mass energy.

   (b) The event is required to have between two and six tracks. Dividing the event into two thrust hemispheres, the legal track configurations are: one track recoiling against one track (1-1), one track recoiling against three tracks (1-3), or three tracks recoiling against three tracks (3-3).

   (c) The track momenta of two-track events are required to be $\lesssim 60\%$ of the beam momentum.

   (d) The invariant masses of the charged tracks in each hemisphere must be less than 2 GeV.

The detection efficiencies for lepton pairs are strongly affected by the acceptance of the tracking, calorimetric, and muon identification systems. Typically, electrons are selected with the largest efficiency ($\sim 70\%$). The typical detection efficiencies for muon and tau pairs are 60% and 50%, respectively. The uncertainties on the efficiencies are typically about 2%. The background contamination from hadronic events, two-photon events, and miscategorized lepton pairs ranges from $\sim$1% for electron pairs to $\sim$5% for tau pairs.

Luminosity Measurement

The experimental luminosities are inferred from measurements of the process $e^+e^- \rightarrow e^+e^-$ at small scattering angles (25-150 milliradians). In the small angle region, this process is dominated by t-channel exchange of photons and is independent of the parameters of the Z^0 system. The tree-level differential cross section has the form,

$$\frac{d\sigma_{lum}}{d\theta} \simeq \frac{4\pi\alpha^2}{s} \cdot \frac{1}{\theta^3}, \tag{4.18}$$

where the scattering angle θ is assumed to be small. An accurate determination of the luminosity requires that the radiative corrections be included in equation (4.18). Nevertheless, equation (4.18) does illustrate one of the difficulties in the measurement of the luminosity. The measured cross section σ_{lum}^{meas} is a sensitive function of the angular acceptance of the detector edges,

$$\sigma_{lum}^{meas} \simeq \frac{2\pi\alpha^2}{s}\left(\frac{1}{\theta_1^2} - \frac{1}{\theta_2^2}\right), \tag{4.19}$$

where θ_1 and θ_2 are the angles of the inner and outer detector edges.

Each of the SLC/LEP detectors contains a luminosity monitor that consists of two cylindrical electromagnetic calorimeters designed to detect e^+e^- pairs in the very forward regions (from 25-60 milliradians at the inner edges to ~150 milliradians at the outer edges). In order to control the angular acceptance well, each device is either highly segmented or contains an integral tracking system to measure the scattering angle of each particle. The accepted cross section for these devices is in the range 25-150 nb. In some cases, the statistical error on the luminosity determination is a bit worse than that on the number of hadronic events (the radiatively corrected cross section for hadronic events is ~30 nb). The systematic error on the luminosity measurement is usually dominated by the uncertainty on the accepted cross section and on the effect of higher-order radiative corrections. The systematic errors range from 1.3% to about 5%.

The uncertainty on the luminosity determination must be combined with the uncertainty on the detection efficiency to yield an overall normalization uncertainty for a cross section measurement. The overall normalization uncertainties are typically several percent.

Experimental Results

The current results of the five SLC/LEP experiments[3-7] are listed in Table VIII. The Mark II, ALEPH, DELPHI, L3, and OPAL results are based upon exposures of 17, 850, 53.9, 627, and 1247 nb^{-1}, respectively.

Table VIII

The results of the Z^0 mass and width analyses of the SLC/LEP experiments.

Experiment	M_Z (GeV)	Γ_Z (GeV)	Γ_{inv} (MeV)	σ^0_{had} (nb)	$\Gamma_{\ell\ell}$ (MeV)
Mark II[3]	91.14(12)	$2.42(^{+45}_{-35})$	460(100)	42.0(40)	$92.0(^{+170}_{-160})$
ALEPH[4]	91.18(4)	2.54(6)	501(26)	41.4(8)	83.9(22)
DELPHI[5]	91.06(9)	2.42(21)	400(107)	42.8(58)	—
L3[6,17]	91.16(4)	2.54(5)	548(29)	39.8(9)	83.0(24)
OPAL[7]	91.16(3)	2.54(5)	453(44)	41.2(11)	81.9(20)
Average	91.16(3)	2.54(3)	506(17)	40.8(5)	82.9(13)

The following notes apply to the information that is presented in Table VIII.

1. The Mark II value for the leptonic partial width is determined from the product of the measured[18] ratio $\Gamma_{\ell\ell}/\Gamma_{had}$ and the theoretical value for Γ_{had}.

2. The ALEPH Collaboration quote their result for Γ_{inv} in terms of the number of neutrinos N_ν as defined by the following

$$\Gamma_{inv} = N_\nu \cdot \Gamma_{\nu\nu} = N_\nu \cdot 166 \text{ MeV}. \tag{4.20}$$

They derive N_ν from an analysis of Γ_Z and σ^0_{had}. Note that this procedure is entirely equivalent to the use of equation (4.7) in a constrained fit. We convert their result to Γ_{inv} for display purposes.

3. The Delphi Collaboration do not use σ^0_{had} as a fit parameter but instead scale the Standard Model value with a free normalization parameter. We convert their result for the normalization parameter into a value for the peak cross section.

4. The averages that are listed in the last line are calculated by weighting each measurement appropriately with its error. The common energy scale error was correctly included in the averaging procedure. All other errors are assumed to be uncorrelated (which is undoubtedly incorrect).

The measurements of the resonance parameters that are shown in Table VIII agree remarkably well with the Standard Model predictions. Using equation (4.20) we estimate the number of light neutrino species to be,

$$N_\nu = 3.04 \pm 0.10,$$

which is the best evidence for the three generation model (note that neutrino species of mass larger than $M_Z/2$ are not ruled out). The only apparent discrepancy between the measurements and the expectations is that Γ_Z seems a bit larger than expected (by ~60 MeV). There are several possible explanations for this. We list them in descending order of likelihood: 1) it is a statistical fluctuation (the probability of a fluctuation is not small enough to establish a discrepancy); 2) there is a correlating effect (like the energy of a scan point differed from its nominal value); 3) the QCD corrections to the hadronic partial widths need more work; 4) there is a new particle in the final state. It is even possible that several of these explanations are valid.

Systematic Errors

The various resonance parameters vary in their sensitivity to the energy scale and normalization uncertainties. The determination of M_Z depends completely on the accelerator energy scale. The 27 MeV uncertainty on the LEP energy scale and the 40 MeV uncertainty on the SLC energy scale apply directly to mass measurements made at the two machines. The model-independent determinations of M_Z

are completely insensitive to the normalization uncertainty. The model constrained determinations of M_Z have a slight sensitivity to the normalization uncertainty. These uncertainties are typically a few MeV or less (even with the model constraints, most of the M_Z information is derived from the resonance shape).

The peak cross section and the invisible width are strongly affected by normalization uncertainty. This can be seen from an inspection of equation (4.7). The invisible width enters the cross section as a component of the total width. The influence of the total width is maximized when the center-of-mass energy is $s = M_Z^2$. The effect of the normalization uncertainty $\delta\sigma$ upon the invisible width is approximately,

$$\delta\Gamma_{inv} \simeq 1.5 \text{ GeV} \cdot \left(\frac{\delta\sigma}{\sigma}\right).$$

The measurement of Γ_Z depends almost entirely upon the measurement of the resonance shape. It is therefore insensitive to the absolute energy and normalization errors. It is sensitive to point-to-point errors in the energy and luminosity. These are typically much smaller than the absolute errors.

The measurement of the leptonic width is sensitive to the absolute normalization uncertainty. The peak leptonic cross section is proportional to the square of the leptonic width. The percentage uncertainty on $\Gamma_{\ell\ell}$ is therefore one half of the percentage uncertainty on the normalization.

4.3. Mass and Width of the W

The measurement of the W boson mass and width will become possible in the second phase of LEP operation. The installation of superconducting RF cavities will permit the beam energy to be increased to a value above the threshold for the process $e^+e^- \to W^+W^-$.

High Energy e^+e^- Cross Sections

The tree-level expression for the W-pair cross section is somewhat complex.[19] The inclusion of initial state radiation (as in equation (4.3)) and finite widths

for the final state W bosons involves a four dimensional convolution of the tree-level expression. We therefore choose to present only the result of a Monte Carlo integration. The cross section for the process $e^+e^- \rightarrow W^+W^-$ is plotted in Figure 12 as a function of $E_b - M_W$ where E_b is the single beam energy. The mass and width of the W are assumed to be 80 GeV and 2.1 GeV, respectively. Note that three curves are plotted: the dashed curve is the basic tree-level cross section; the dashed-dotted curve is the cross section including the effect of initial state radiation; and the solid curve is the cross section including initial state radiation and the effect of a finite W width. The inclusion of initial state radiation reduces the size of the cross section. The finite W width produces non-zero cross section at energies below the nominal threshold at $E_b = M_W$.

The basic $e^+e^- \rightarrow f\bar{f}$ cross section for five quark and three lepton flavors increases from about 7 units of R at center-of-mass energies below the Z^0 pole to 10 units of R at energies above the Z^0 pole.* At $\sqrt{s} = 160$ GeV, the tree-level cross section is approximately 34 pb. Unfortunately, the initial state radiative corrections increase this number enormously. Although the photon structure functions decrease greatly as x is decreased from 1, the Z pole is sufficiently large that the convolution given in equation (4.3) is several times larger than the tree-level cross section. The process $e^+e^- \rightarrow \gamma Z^0$ therefore dominates the visible cross section at W-pair threshold. Using equation (4.3), we estimate the size of the visible cross section to be $\sim$150 pb at $\sqrt{s} = 160$ GeV.

$\underline{e^+e^- \rightarrow W^+W^- \text{ Threshold Scan}}$

There are several different techniques that can be used to measure the W mass at LEP II. It is possible to extract M_W from the measured distributions of jet masses or lepton energies. These methods are are described in Reference 20. The technique that we'll discuss here is the measurement of the threshold behavior of the W pair cross section.

$\star$ The unit of R is the cross section for $e^+e^- \rightarrow \gamma^* \rightarrow \mu^+\mu^-$. Numerically, the cross section has the value $\sigma_R = 86.8$ nb-GeV$^2/s$.

It is clear than the W mass can be extracted from the *step* in the cross section that is shown in Figure 12. Since there is a large background from ordinary processes, it is necessary to apply selection criteria to the data to improve the signal-to-noise ratio. The background processes produce mostly two- and three jet hadronic events or lepton pair events that are often highly boosted along the beam direction. The visible energy of the background is often small as compared with $\sqrt{s}$. The W-pair events appear most often as four-jet events ($\sim$44% of W-pairs) or as an energetic lepton and two jets ($\sim$44% of W-pairs). The authors of Reference 20 have studied a number of selection criteria to reduce the background cross section to less than $\sim$1 pb while retaining $\sim$75% of the four-jet and $\sim$45% of the lepton+two-jet events (we assume that τ leptons cannot be used and that one third of the remaining events are eliminated by the isolation cut used to suppress heavy flavor events). Assuming that the residual background is due to the large $\sqrt{\hat{s}}$ continuum, the measured cross section would have the following form,

$$\sigma_{meas}(E_b) = \varepsilon\sigma_{ww}(E_b) + \frac{B}{(2E_b)^2}, \tag{4.21}$$

where: ε is the efficiency to identify a W-pair event ($\varepsilon \simeq 0.53$); $\sigma_{ww}(E_b)$ is the cross section plotted in Figure 12; and B is a constant that represents the residual background (which presumably scales as $1/s$).

subsectionSensitivity Functions

We can analyze the M_W and Γ_W sensitivity of a cross section scan of the W pair threshold by using the scanning theory that was discussed in the last section. Numerically differentiating the measured cross section (as defined in equation (4.21)), it is straightforward to calculate the sensitivity functions for M_W, Γ_W, and the background constant B. For the purpose of this exercise, we assume that $B = 1$ pb $\cdot (2M_W)^2$ or that the background cross section is 1 pb at W-pair threshold.

The sensitivity function $S(E_b, M_W)$ is plotted in Figure 13 as a function of $\epsilon_b = E_b - M_W$. Note that the maximum sensitivity occurs at $\epsilon_b \simeq 0.5$ GeV.

The sensitivity function $S(E_b, \Gamma_W)$ is shown in Figure 14 as a function of ϵ_b. As one would expect, it peaks just below the nominal threshold ($\epsilon_b = -1$ GeV) where the width-induced *tail* in the cross section is largest. The function $S(E_b, \Gamma_W)$ decreases rapidly as E_b is increased. It passes through zero near $\epsilon_b = 1$ GeV and plateaus above $\epsilon_b = 3$ GeV. The sensitivity in the plateau region is due to the reduction in the cross section caused by the finite width (see Figure 12). The maximum value of $|S(E_b, \Gamma_W)|$ is smaller than the maximum value of the mass sensitivity function by a factor of three. A good measurement of Γ_W will clearly require a substantial commitment of luminosity to a point of very small cross section. Note that the product $S(E_b, M_W) \cdot S(E_b, \Gamma_W)$ is an odd function about the point $\epsilon_b = 1$ GeV. In principle, the M_W-Γ_W correlation can be cancelled by measuring the cross section on both sides of this point. The functions $S(E_b, M_W)$ and $S(E_b, \Gamma_W)$ are not large in the region $\epsilon_b > 1$ GeV. The cancellation of the correlation therefore requires a substantial commitment of luminosity to a relatively insensitive region.

The function $S(E_b, B)$ is plotted as a function of ϵ_b in Figure 15. As one would expect, the background sensitivity is largest at small beam energy and decreases dramatically as E_b increases through the W pair threshold. Note that it is possible to cancel the B-Γ_W correlation but that it is not possible to cancel the B-M_W correlation.

Scan Strategies

It is clear that precise measurements of M_W and Γ_W require that LEP be operated in regions of small cross section. Since all other studies of the W-pair system require a large sample of data, there will be considerable pressure to operate the machine on the cross section plateau at the largest available energy. In order to estimate how precisely M_W and Γ_W could be measured in a 1-2 year run (500 pb^{-1}), we assume that 50% of the luminosity is dedicated to operating at the largest available energy (we assume that $\epsilon_b = 15$ GeV or $\sqrt{s} = 190$ GeV is achieved) and the remaining 50% is dedicated to operation in the threshold region.

It is instructive to first consider an extremely unrealistic scan scenario. We assume that we will measure only one parameter and that the other parameters are precisely known. In this case, we need only one scan point in the threshold region for a constrained fit. We choose to allocate the entire 250 pb^{-1} luminosity to operation at the most mass-sensitive point ($\epsilon_b = 0.5$ GeV) or at the most width-sensitive point ($\epsilon_b = -1$ GeV). Using equation (4.16) we estimate the precision of these measurements to be

$$\delta M_W = 92 \text{ MeV} \quad \text{or} \quad \delta \Gamma_W = 286 \text{ MeV}.$$

The M_W measurement would be a very desirable result. The Γ_W measurement is not competitive with the recent indirect determinations that have been published by the CDF and UA2 collaborations;[15,21]

$$\Gamma_W = (0.85 \pm 0.08) \cdot \Gamma_Z = 2.19 \pm 0.20 \text{ GeV (CDF)}$$
$$\Gamma_W = (0.89 \pm 0.08) \cdot \Gamma_Z = 2.30 \pm 0.20 \text{ GeV (UA2)}.$$

Since the width cannot be measured to an interesting level, it is clearly unwise to design a scan to measure Γ_W. We therefore concentrate on the measurement of M_W.

A real measurement of M_W will require that the background constant B be varied as a fit parameter. Unfortunately, the B-M_W correlation cannot be canceled by a clever choice of scan points. It is therefore necessary to measure both parameters well.

The number of scan points is somewhat arbitrary. A minimum of three points are required to constrain the two parameter problem. The presence of a high energy point implies that only two points are needed in the threshold region. Equation (4.14) implies that several closely spaced points in a region of large sensitivity are equivalent to a single point in the same region. We can therefore analyze the optimization of the M_W measurement by considering a two-point threshold measurement.

An optimal scan must include an energy point in a region of large background sensitivity $|S(E_b, B)|$ and a point near the maximum of the mass sensitivity function $|S(E_b, M_W)|$. We choose the scan point energies to be $\epsilon_b = -5$ GeV and $\epsilon_b = 0.5$ GeV, respectively.* The apportionment of the available luminosity between the two points is a straightforward problem in one-dimensional optimization. We find that the error δM_W has a very broad minimum about the ratio of luminosities, $L(0.5 \text{ GeV})/L(-5 \text{ GeV}) \simeq 2/1$. If the luminosities of the -5 GeV and 0.5 GeV points are 85 pb^{-1} and 165 pb^{-1}, respectively, the minimum value of the error δM_W is approximately 155 MeV.

A two-point threshold scan is somewhat risky. It is safer to bracket the region of maximum M_W sensitivity with several scan points. We therefore construct an optimal four-point scan (a five-point measurement when the $\epsilon_b = 15$ GeV point is included) by assigning one third of the 165 pb^{-1} (55 pb^{-1}) to each of three points: $\epsilon_b = 0$ GeV, 0.5 GeV, and 1.0 GeV. It is instructive to compare this scan (Scan 1) with a slightly modified version. The modified version (Scan 2) is created by shifting the luminosity from the $\epsilon_b = 0$ GeV point to $\epsilon_b = -1$ GeV. We expect the second scan strategy to improve the width measurement at the expense of the mass measurement. Finally, we note that our modified scan strategy is similar to the scan strategy that was studied in Reference 20 (which we label Scan 3). The authors of Reference 20 assigned 100 pb^{-1} to each of the following five points: $\epsilon_b = -5$ GeV, -1 GeV, 0 GeV, 1 GeV, and 15 GeV.

Using equation (4.14) and the sensitivity functions, the performance of each scan scenario can be estimated. The expected number of detected events and the expected precisions δM_W, $\delta \Gamma_W$, and δB are listed in Table IX for each of the three scan strategies. The presence of a high energy point in each strategy reduces the M_W-Γ_W correlation sufficiently that the M_W precision obtained from the three parameter fit is essentially identical to that obtained from a two-parameter fit.

---

* Varying the energy of the second point about $\epsilon_b = 0.5$ GeV verifies that the B-M_W correlation does not shift the point of maximum M_W sensitivity.

As one might expect, the third scan strategy which allocates 400 pb^{-1} to the threshold measurement provides the most precise M_W measurement, $\delta M_W =$ 150 MeV. *The M_W precision obtained from the optimized mass scan (Scan 1) is worse by 7%. Note however, that Scan 1 produces nearly 60% more events than does Scan 3.* Surprisingly, the second scan strategy provides a slightly better width measurement than does the third strategy. This occurs because the second scan produces a smaller B-Γ_W correlation than does the third scan strategy.

It is clear from equation (4.21) that the functions $S(E_b, a_j)$ are sensitive to the level of residual background and to the W-pair detection efficiency. We investigate these effects by reducing the background constant to $B = 0.5$ pb $\cdot (M_W)^2$ and by increasing the detection efficiency to $\varepsilon_{ww} = 0.70$. The results are listed in Table IX. The error δM_W is improved by approximately 20 MeV in the case that the background is reduced by a factor of two. The mass error is improved by approximately 30 MeV when the efficiency is increased. Note that the optimal luminosity ratio $L(0.5 \text{ GeV})/L(-5 \text{ GeV})$ is nominally sensitive to both effects. However, the optimal region is so broad that the use of a 2/1 ratio degrades the result by less than 1%.

Table IX

The predicted results of three different five-point measurements of the W-pair threshold. Scan 1 is optimized for the measurement of M_W. Scan 2 is an attempt to improve the measurement of Γ_W. Scan 3 is identical to the threshold scan used in Reference 20. The results are presented for several assumptions about the level of residual background B and the W-pair detection efficiency.

Quantity	Scan 1	Scan 2	Scan 3
L[-5 GeV] (pb^{-1})	85	85	100
L[-1 GeV] (pb^{-1})	0	55	100
L[0 GeV] (pb^{-1})	55	0	100
L[0.5 GeV] (pb^{-1})	55	55	0
L[1 GeV] (pb^{-1})	55	55	100
L[15 GeV] (pb^{-1})	250	250	100
$B = 1.0$ pb $\cdot [2M_W]^2$ $\varepsilon_{ww} = 0.53$			
Number of Events	2951	2912	1863
δM_W (MeV)	160	176	150
$\delta\Gamma_W$ (MeV)	531	482	492
δB (pb $\cdot [2M_W]^2$)	0.12	0.12	0.12
$B = 0.5$ pb $\cdot [2M_W]^2$ $\varepsilon_{ww} = 0.53$			
Number of Events	2737	2698	1627
δM_W (MeV)	137	154	130
$\delta\Gamma_W$ (MeV)	508	450	448
δB (pb $\cdot [2M_W]^2$)	0.096	0.098	0.098
$B = 1.0$ pb $\cdot [2M_W]^2$ $\varepsilon_{ww} = 0.70$			
Number of Events	3760	3709	2309
δM_W (MeV)	130	144	123
$\delta\Gamma_W$ (MeV)	453	407	410
δB (pb $\cdot [2M_W]^2$)	0.12	0.13	0.13

Systematic Errors

The measurement of the W-pair threshold is affected by systematic uncertainties on the energy scale and cross section normalization. The energy scale uncertainty affects the M_W measurement directly. Assuming that the fractional error on the beam energy scale is constant, the uncertainty on M_W should be comparable to the one that applies to the M_Z measurement. By 1994, this uncertainty is expected to be ~20 MeV.

The sensitivity of the results given in Table IX to normalization errors can be estimated from equation (4.17). Taking the first scan strategy as an example, we estimate that the uncertainties on the parameters are related to an overall normalization uncertainty $\delta\sigma/\sigma$ as follows,

$$\delta M_W = -2.26 \text{ GeV} \cdot \frac{\delta\sigma}{\sigma}$$
$$\delta\Gamma_W = -19.3 \text{ GeV} \cdot \frac{\delta\sigma}{\sigma}.$$

The normalization error must be controlled to the 3% level to avoid inflating the M_W error.

Sensitivity to Assumptions

Our analysis assumes that we have complete *a priori* knowledge of the W resonance parameters. Although the characteristic width in E_b space of the M_W-sensitive region is larger than the current uncertainty on M_W, our precision estimates are likely to be somewhat optimistic. It is possible to alter the results by $\lesssim$10% by varying the resonance parameters over reasonable intervals.

Conclusions

Despite the uncertainties on the ultimate W-pair detection efficiency and residual background contamination, several conclusions can be drawn from this analysis:

1. The most sensitive scan region for the measurement of M_W is ϵ_b = 0-1 GeV. *The mapping of the entire threshold shape would produce a less precise measurement.*

2. It is not possible to remove the correlation between the background parameter and M_W by a clever choice of scan point energies. This implies that a scan point of energy below the nominal threshold is quite important. If the energy is chosen to be $\epsilon_b = -5$ GeV ($E_b = 75$ GeV), an M_W-optimized scan strategy would allocate twice as much integrated luminosity to the M_W sensitive region as is allocated to the low energy point.

3. A measurement of M_W at the $\lesssim$160 MeV level is possible with the dedication of a large integrated luminosity (250 pb^{-1}) and good control of the background contamination.

4. The measurement of Γ_W to an interesting level is difficult or impossible. It is probably unwise to attempt anything more than a cursory measurement.

4.4. Forward-Backward Asymmetries

In the next several years, several asymmetries of the Z^0 cross section will be used to test the electroweak portion of the Standard Model. Note that all of these tests work by measuring the ratio of the vector and the axial vector couplings of the Z^0 to the fermionic current. As was described in the Introduction, this implies that the sensitivities of the various tests can be characterized in terms a single parameter $\sin^2\theta_w$. Note that this parameter differs from the Sirlin definition that was used to describe the ratio M_W/M_Z.

Let us begin by considering the cross section for the process $e^+e^- \rightarrow f\bar{f}$. We assume the electron and positron beams can be longitudinally polarized. The beam polarizations, P^- and P^+, are described in terms of a helicity basis ($P = +1$ describes a right-handed beam, $P = -1$ describes a left-handed beam). We can then write the tree-level cross section in the cm frame as follows,

$$\frac{d\sigma_f}{d\Omega} = \frac{\alpha^2 N_c^f}{64s\sin^4 2\theta_w} \cdot \left\{(1 - P^+P^-)[\sigma_u^{\gamma Z} + \sigma_u^Z] + (P^+ - P^-)[\sigma_p^{\gamma Z} + \sigma_p^Z]\right\} \quad (4.22)$$

where: the unpolarized partial cross sections due to γZ interference and pure Z

exchange are defined as,

$$\sigma_u^{\gamma Z} = -8Q_f \sin^2 2\theta_w \mathrm{Re}[\Gamma(s)]\Big[(1+\cos^2\theta^*)vv_f + 2\cos\theta^* aa_f\Big]$$
$$\sigma_u^{Z} = |\Gamma(s)|^2\Big[(1+\cos^2\theta^*)(v^2+a^2)(v_f^2+a_f^2) + 8\cos\theta^* vav_f a_f\Big];$$

θ^* is the angle of the outgoing fermion relative to the incident electron; the polarized partial cross sections due to γZ interference and pure Z exchange are defined as,

$$\sigma_p^{\gamma Z} = 8Q_f \sin^2 2\theta_w \mathrm{Re}[\Gamma(s)]\Big[(1+\cos^2\theta^*)av_f + 2\cos\theta^* va_f\Big]$$
$$\sigma_p^{Z} = -|\Gamma(s)|^2\Big[(1+\cos^2\theta^*)2va(v_f^2+a_f^2) + 2\cos\theta^*(v^2+a^2)2v_f a_f\Big];$$

the constant N_c^f is the color factor (3) for quark final states; and where the normalized Z propagator is defined in equation (3.12). Note that we've assumed that the masses of all final state fermions are small as compared with $\sqrt{s}$ and that the unpolarized cross section for pure photon exchange is small as compared with the pure Z and interference terms. In the case that the beams are unpolarized ($P^+ = P^- = 0$), equation (4.22) is identical to the expression that we used to describe the cross section for the process $q\bar{q} \to Z^0, \gamma \to \ell^+\ell^-$ (equation (3.12)).

We have already defined the forward-backward asymmetry in the context of the process $q\bar{q} \to \ell^+\ell^-$ (see equation (3.19)). The asymmetry is defined in exactly the same way for the process $e^+e^- \to f\bar{f}$. For unpolarized electrons and positrons, the form of the asymmetry **at the Z^0 pole** is identical to the form that was given in equation (3.20),

$$A_{FB}^f(x) = F(x)\cdot A_{FB}^f = F(x)\cdot\frac{3}{4}\cdot\frac{-2va}{v^2+a^2}\cdot\frac{-2v_f a_f}{v_f^2+a_f^2} = F(x)\cdot\frac{3}{4}\cdot A_{LR}\cdot A_{LR}^f, \quad (4.23)$$

where the function $F(x) = 4x/(3+x^2)$ accounts for incomplete coverage of the detector in $x = \cos\theta^*$ space, and A_{LR}^f is defined as a particular combination of

coupling constants,

$$A_{LR}^{f} \equiv \frac{-2v_f a_f}{v_f^2 + a_f^2}. \tag{4.24}$$

The forward-backward asymmetries are fairly sensitive to $\sin^2\theta_w$ due to the presence of the vector coupling constants (see equations (2.2) and (2.3)). The expected size and sensitivity to $\sin^2\theta_w$ of each asymmetry is listed in Table X (assuming that the appropriate value of $\sin^2\theta_w$ is 0.233).

Table X

Fermion Type	A_{FB}^{f} ($\sin^2\theta_w = 0.233$)	Sensitivity to $\sin^2\theta_w$
u-quark	0.063	$\delta A_{FB}^{u} \simeq 4.2\delta\sin^2\theta_w$
d-quark	0.089	$\delta A_{FB}^{d} \simeq 5.6\delta\sin^2\theta_w$
charged lepton	0.012	$\delta A_{FB}^{\ell} \simeq 1.6\delta\sin^2\theta_w$

Table X illustrates a *Peter Principle* of experimental physics, *the most easily measured quantities are usually the least interesting ones.* The forward-backward asymmetry for muons is undoubtedly the most straightforward one to measure but is the least sensitive to $\sin^2\theta_w$. The identification and measurement of quark jets is more difficult. The DELPHI Collaboration[22] have studied the flavor tagging of simulated of hadronic jets (which makes use of the particle identification capability of their detector). The identification criteria, tagging efficiency, level of residual background, and the corresponding uncertainty on A_{FB}^{f} are listed in Table XI. They find good consistency between several different fragmentation models. The obvious (and difficult to answer) question is whether nature agrees with the fragmentation models to the same level of consistency. It is clear that believable results must be based upon very detailed experimental fragmentation studies.

Table XI

The result of a Monte Carlo study of the flavor tagging of hadronic jets with DELPHI detector.[22]

Flavor	Significant Criteria	Efficiency	Background	δA_{FB}^f
b-quark	$\ell^{\pm}K^{\pm}$ pairs, $P_\ell P_K > 25$ GeV^2	11.2%	16.1%	0.0013
c-quark	$\ell^{\pm}K^{\mp}$ pairs, reconstruct D^*	8.1%	32.2%	0.0013
s-quark	high momentum $K^{\pm}$,K_s^0,K^{0^*}	2.9%	45.5%	0.0026
u-quark	high momentum protons	1.4%	30.5%	0.002

Initial State Radiative Corrections

We have already seen that the emission of initial state radiation causes the effective center-of-mass energy $\sqrt{\hat{s}}$ to be skewed from the nominal value. At tree-level, the electroweak interference term causes a shift in the asymmetry as the energy varies away from M_Z. Ignoring a small term in the denominator, the energy dependence of the asymmetry can be expressed as follows,

$$A_{FB}^f(\hat{s}) \simeq A_{FB}^f(M_Z^2) - 6Q_f \sin^2 2\theta_w \Big(1 - \frac{M_Z^2}{\hat{s}}\Big) \frac{a a_f}{(v^2+a^2)(v_f^2+a_f^2)}. \qquad (4.25)$$

The interference term becomes large as $\sqrt{\hat{s}}$ varies from M_Z. Note that a shift $\Delta\sqrt{\hat{s}} = -148$ MeV is sufficient to cancel the tree-level muonic forward-backward asymmetry!

The energy dependence of the forward-backward asymmetries is plotted[23] Figure 16. Note that the d-quark forward-backward asymmetry is the least sensitive to changes in $\sqrt{\hat{s}}$. The steep energy dependence of the leptonic forward-backward asymmetries implies that they are quite sensitive to uncertainties on the initial state radiative corrections. The uncertainty on A_{FB}^{μ} is currently estimated[24] to

be 0.001. The corresponding uncertainties on the quark asymmetries are much smaller.

QCD Corrections

The quark forward-backward asymmetries are affected by QCD corrections to the $Zq\bar{q}$ vertex and by real gluon emission (which produces three-jet events). The QCD corrections have been computed to first order in α_s by Kleiss, Renard, and Verzegnassi.[25] They find that the corrected asymmetry $A^q_{FB}(\alpha_s)$ can be described in terms of the tree-level asymmetry as follows,

$$A^q_{FB}(\alpha_s) = A^q_{FB}(\alpha_s = 0)\Big[1 - \eta\frac{\alpha_s}{3\pi}\Big], \tag{4.26}$$

where the parameter η is four if all two- and three-jet events are used. If the three-jet events (according to a purely theoretical definition) are excluded, the parameter η decreases to one. The value of η that is appropriate to a real experiment must therefore be in the range 1-4. This leads to an uncertainty that is a few percent of the native asymmetry.

Statistical Uncertainties

The statistical uncertainty that is associated with the measurement of an asymmetry A is given by the following expression,

$$\delta A = \Big[\frac{1 - A^2}{N}\Big]^{1/2} \simeq \frac{1}{\sqrt{N}}, \tag{4.27}$$

where the number of events N is assumed to be large enough that a Gaussian treatment is applicable. Note that most asymmetries are small as compared with unity so that the A^2 term in the numerator can be ignored.

Bottom Line

The LEP experiments are expected to accumulate a sample of 6×10^6 hadronic Z^0 decays (which corresponds to an integrated luminosity of 200 pb^{-1}) in the next

several years. Combining the expected statistical and systematic errors, the precision of the various forward-backward asymmetry measurements can be predicted. The total uncertainty δA_{FB}^{f} and the corresponding uncertainty on $\sin^2\theta_w$ are listed in Table XII.

Table XII

The expected precision of measurements of the forward-backward asymmetries with a sample of 6×10^6 Z^0 events.

Asymmetry	δA_{FB} (all effects)	$\delta\sin^2\theta_w$
A_{FB}^{μ}	0.003	0.0020
A_{FB}^{u}	0.01	0.0030
A_{FB}^{s}	0.007	0.0016
A_{FB}^{c}	0.007	0.0021
A_{FB}^{b}	0.006	0.0010

Note that the b quark asymmetry offers the most sensitive test of the Standard Model. This particular asymmetry has a particular difficulty that must be addressed. The measured asymmetry can be diluted by the mixing of neutral B mesons. A complete reconstruction of each B meson or baryon would permit the exclusion of the B_d^0 and B_s^0 mesons from the asymmetry measurement. Unfortunately, this is beyond the capability of most detectors. The tagging of b-jets is more easily done with large P_t (with respect to the jet axis) leptons. The measured asymmetry $A_{FB}^{b}(meas)$ is then related to the native quark asymmetry by the following expression,

$$A_{FB}^{b}(meas) = (1-2\chi_m)\cdot A_{FB}^{b}, \tag{4.28}$$

where χ_m is the mixing-induced probability of measuring a wrong-sign lepton. The parameter χ_m can be extracted from a measurement of the ratio of the number of same-sign lepton pairs to the total number of lepton pairs,

$$\frac{N(\ell^+\ell^+)+N(\ell^-\ell^-)}{N(\ell\ell)} = 2\chi_m(1-\chi_m),$$

where the notation is obvious. Note that χ_m is not the actual mixing parameter but is a phenomenological average quantity that depends upon the neutral meson fractions and upon the selection criteria.

A reasonable value for χ_m is in the range $\sim$0.1. Therefore, a sample of 6×10^6 hadronic Z^0 decays would produce several thousand same-sign lepton pairs. This number should be adequate to correct the measured asymmetry for mixing effects without inflating the combined error greatly.

4.5. The Left-Right Polarization Asymmetry

At the beginning of this lecture, we mentioned that the SLC will have a polarized electron beam with a degree of polarization $P_0 \simeq 40\%$. There are also plans to produce longitudinally polarized electron and positron beams at LEP. These enterprises are designed to measure the polarization dependent part of the total cross section as defined in equation (4.22). The forward-backward asymmetries are defined to select the part of the e^+e^- cross section that is odd under spatial reflection. The left-right polarization asymmetry is designed to select the part of the cross section that is odd in difference of the beam polarizations $P^+ - P^-$. It is therefore useful to define a generalized beam polarization P_g that is proportional to $P^+ - P^-$ and has a convenient normalization,

$$P_g \equiv \frac{P^+ - P^-}{1 - P^+P^-}. \tag{4.29}$$

Note that P_g is positive whenever the electron beam is left-handed and/or the positron beam is right-handed. It is negative whenever the reverse is true. The generalized polarization becomes unity when either beam is completely polarized. The positron beam of the SLC is unpolarized. The generalized polarization therefore has the simple form, $P_g = -P^-$.

The left-right polarization asymmetry is defined as the ratio of the difference of the total Z^0 production rates with left-handed and right-handed beams to the

total rate. This can be expressed more precisely as,

$$A_{LR} \equiv \frac{\sum_f \left\{ \int_{-x_f}^{x_f} dc\sigma_f(c, P_g = +1) - \int_{-x_f}^{x_f} dc\sigma_f(c, P_g = -1) \right\}}{\sum_f \left\{ \int_{-x_f}^{x_f} dc\sigma_f(c, P_g = +1) + \int_{-x_f}^{x_f} dc\sigma_f(c, P_g = -1) \right\}}, \tag{4.30}$$

where: $c \equiv \cos\theta^*$; $\sigma_f(c, P_g)$ is shorthand for the differential cross section $d\sigma_f/d\Omega^*$; $\pm x_f$ are integration limits that depend upon fermion type; and where the sum is taken over all visible final state fermions except electrons (to exclude the t-channel scattering process). Note that the integrals must be taken over symmetric limits (which is a natural property of most e^+e^- detectors).

Substituting equation (4.22) (actually, the version of equation (4.22) with finite final state masses) into equation (4.30) it is straightforward to show that the left-right asymmetry takes the following form **on the Z^0 pole**,

$$A_{LR} = \frac{-2va \sum_f \int_{-x_f}^{x_f} dc[(v_f^2 + a_f^2)(1 + \beta_f^2 c^2) + (v_f^2 - a_f^2)(1 - \beta_f^2)]}{(v^2 + a^2) \sum_f \int_{-x_f}^{x_f} dc[(v_f^2 + a_f^2)(1 + \beta_f^2 c^2) + (v_f^2 - a_f^2)(1 - \beta_f^2)]},$$

where β_f is the velocity of the final state fermion in the $f\bar{f}$ center-of-mass frame. Cancelling the common factor, we recover a familiar expression,

$$A_{LR} = \frac{-2va}{v^2 + a^2} = \frac{2(1 - 4\sin^2\theta_w)}{1 + (1 - 4\sin^2\theta_w)^2}. \tag{4.31}$$

A number of conclusions can be drawn from this derivation:

1. A_{LR} depends upon the Z^0-electron couplings alone. The dependence on the final state couplings cancels in the ratio.

2. A_{LR} is independent of the detector acceptance. This remains true even if each final state fermion is accepted differently.

3. A_{LR} is independent of final state mass effects (which would cause β_f to differ from unity).

4. All of the visible final states except the electron pairs can be used to measure A_{LR}. The measurement therefore utilizes about 96% of the visible decays. The various other Standard Model tests that are performed on the Z^0 pole make use of much smaller fractions of the event total ($\sim$ 4% for the muonic forward-backward asymmetry, $\sim$ 0.9% for the τ polarization measurement, and $\sim$ 4% for the b-quark forward-backward asymmetry).

5. A_{LR} is very sensitive to the electroweak mixing parameter $\sin^2\theta_w$. This is shown graphically in Figure 17. Small changes in A_{LR} are related to changes in $\sin^2\theta_w$ by the following expression,

$$\delta A_{LR} \simeq -8\delta\sin^2\theta_w. \tag{4.32}$$

For $M_Z = 91.17$ GeV, the asymmetry is expected to be in the range 13%-15%.

Radiative Corrections

The left-right asymmetry has the property that it is insensitive to a large class of relatively uninteresting real and virtual radiative corrections and is very sensitive to an interesting set of virtual electroweak corrections. This behavior can be summarized as follows:

1. The left-right asymmetry is very insensitive to initial state radiative corrections. The emission of real photons by the incident electron and positron causes a smearing of the center-of-mass energy of the $f\bar{f}$ system ($\sqrt{\hat{s}}$). The left-right asymmetry is quite insensitive to small changes in $\sqrt{\hat{s}}$. The energy dependence of A_{LR} is compared with those of several forward backward asymmetries in Figure 16. The size of the initial state radiative correction to A_{LR} is calculated to be[26] $\delta A_{LR} \simeq 0.002$ (this is a 2% correction to the asymmetry). The uncertainty on the correction to A_{LR} is smaller by an order of magnitude.

2. The QCD corrections to the left-right asymmetry vanish entirely to all orders in the strong coupling constant α_s at the leading order in the electromagnetic coupling constant α. The leading QCD corrections to A_{LR} are the (extremely small) corrections to the weak vector boson box diagrams.

3. The theoretical uncertainty on A_{LR} is completely dominated by the uncertainty on the renormalization of the electromagnetic coupling constant to the Z^0 mass scale. The current value of this uncertainty is[27] $\delta A_{LR} \simeq 0.002$.

4. The left-right asymmetry is quite sensitive to virtual electroweak corrections and to the presence of new particles. The sensitivity of the asymmetry to the top quark mass (m_{top}) and the Higgs boson mass (m_{Higgs}) will be discussed in the last section of this document.

Experimental Errors

At the SLC, the measurement of A_{LR} is performed by randomly flipping the sign of the beam polarization on a pulse-to-pulse basis and by counting the number of Z^0 events that are produced from each state. The measured asymmetry, A_{LR}^{exp}, is related to the theoretical asymmetry, A_{LR}, by the following expression,

$$A_{LR}^{exp} \equiv \frac{N_Z(P_g = +P_0) - N_Z(P_g = -P_0)}{N_Z(P_g = +P_0) + N_Z(P_g = -P_0)} = P_0 A_{LR}, \tag{4.33}$$

where P_0 is the magnitude of the beam polarization ($P_0 \sim 0.40$), and $N_Z(P)$ is the number of Z^0 events logged with beam polarization P. Since the left-handed and right-handed Z^0 cross sections are measured simultaneously, any systematic effects due to variations in detector livetime, luminosity, beam energy, beam position, etc., are cancelled in the ratio of the cross sections. This technique was used successfully to measure a very small polarized asymmetry ($\sim 10^{-5}$) in electron-deuteron scattering in 1978.[28] The dominant systematic error is expected to be the uncertainty on the beam polarization measurement. We expect that the SLC Compton polarimeter is capable of measuring the beam polarization with a precision of 1-2% ($\delta P_0/P_0 = 1$-2%).

There are a number of consistency checks that can be made with the SLC polarization hardware. It is possible to reverse the circular polarization optics of the electron source laser to search for systematic problems in that system. The polarity of the spin rotation system can be reversed to check for systematic problems in the damping rings. The polarization direction of each polarimeter target is reversible. The beam polarization can be measured separately with each target polarization direction (and must be consistent). Finally, the left-right asymmetry for small-angle Bhabha scattering is *very small* ($\sim 10^{-4}$). The luminosity monitors therefore provide an important check that the left-handed and right-handed luminosities are equal (the left-right asymmetry of the Bhabha signal must be consistent with zero).

Assuming that the dominant systematic error is the beam polarization uncertainty, the combined statistical and systematic uncertainty on A_{LR} is given by the following expression,

$$\delta A_{LR} = \left[A_{LR}^2 \left(\frac{\delta P_0}{P_0} \right)^2 + \frac{1 - (P_0 A_{LR})^2}{P_0^2 N_{tot}} \right]^{1/2}, \tag{4.34}$$

where N_{tot} is the total number of Z^0 events. The expected precision of the A_{LR} measurement and the corresponding precision on $\sin^2\theta_w$ are listed in Table XIII for several values of N_{tot}. Note that the statistical uncertainty dominates the total error in the region $N_{tot} \leq 10^6$. At $N_{tot} = 3 \times 10^6$, the statistical and systematic components are comparable.

Table XIII

The expected error on A_{LR} and $\sin^2\theta_w$ as a function of the number of Z^0 events. The left-right asymmetry is assumed to be $A_{LR} = 0.135$ (which is in the middle of the range that is expected for $M_Z = 91.17$ GeV). The beam polarization is assumed to be $P_0 = 0.40$ and the precision of the polarization monitoring is assumed to be $\delta P_0/P_0 = 0.01$.

N_{tot}	δA_{LR}	$\delta\sin^2\theta_w$
100K	0.008	0.0010
300K	0.005	0.0006
1M	0.003	0.00035
3M	0.002	0.00025

Note that a measurement of A_{LR} with 10^5 events determines $\sin^2\theta_w$ to a level that is comparable to a measurement of A^b_{FB} that is based upon 6×10^6 hadronic Z^0 decays.

4.6. The τ-Lepton Polarization Asymmetry

The left-right polarization asymmetry measures a combination of coupling constants that is particularly sensitive to $\sin^2\theta_w$. It is obvious to ask whether there is comparable information in the degree of polarization of the final state fermions. We define the final state polarization of a fermion as the difference in the cross sections to produce right-handed and left-handed particles,

$$P_f(\cos\theta^*) \equiv \frac{\frac{d\sigma}{d\Omega}(f_R) - \frac{d\sigma}{d\Omega}(f_L)}{\frac{d\sigma}{d\Omega}(f_R) + \frac{d\sigma}{d\Omega}(f_L)}, \tag{4.35}$$

where the notation is obvious. Assuming that the incident electron and positron are unpolarized, it is straightforward to show that the final state polarization is given by the following expression,

$$P_f(\cos\theta^*) = -\frac{2A_{LR}\cos\theta^* + A^f_{LR}(1+\cos^2\theta^*)}{(1+\cos^2\theta^*) + 2A_{LR}A^f_{LR}\cos\theta^*},$$

where the combination of coupling constants A^f_{LR} was defined in equation (4.30).

At any given angle, the polarization of the final state fermion depends upon A_{LR} (the natural Z^0 polarization) and the final state couplings A_{LR}^f. The dependence upon the initial state couplings can be removed by integrating the numerator and denominator of equation (4.35) over symmetric limits. The average value of the final state fermion polarization is then given by the following simple expression,

$$\langle P_f \rangle = -A_{LR}^f. \tag{4.36}$$

The fermion species that is the most obvious candidate for use as a final state polarimeter is the τ-lepton. It decays via a pure $V-A$ current* into low multiplicity final states. Since $\langle P_\tau \rangle$ is formally equivalent to the left-right asymmetry, the measurement of the average τ polarization has some of the same advantages that are inherent in the measurement of A_{LR}:

1. $\langle P_\tau \rangle$ is very sensitive to the electroweak mixing parameter $\sin^2\theta_w$. This is shown graphically in Figure 17. Small changes in $\langle P_\tau \rangle$ are related to changes in $\sin^2\theta_w$ by the following expression,

$$\delta\langle P_\tau \rangle \simeq 8\delta\sin^2\theta_w. \tag{4.37}$$

   For $M_Z = 91.17$ GeV, the average polarization is expected to be in the range 13%-15%.

2. The measured value of $\langle P_\tau \rangle$ is independent of the detector acceptance (assuming that τ^- and τ^+ are accepted equally).

3. The theoretical value of $\langle P_\tau \rangle$ is insensitive to initial state radiative corrections. The energy distributions of the final state decay products are affected slightly by the initial state radiation (which has a small effect on the measured polarization).

* Experimentally, the V-A character of τ decays is not well established. The best measurement of the Michel ρ parameter is[12] $\rho = 0.73 \pm 0.07$ which is consistent with the $V-A$ value of 0.75 but does not rule out significant deviations.

4. $\langle P_\tau \rangle$ is very sensitive to the interesting virtual electroweak corrections. It is affected by the same theoretical error that affects the interpretation of A_{LR}.

The τ as a Polarimeter

The dominant decay modes of the τ-lepton are the four single-prong modes listed in Table XIV.

Table XIV

Decay Mode	Branching Ratio
$e^-\bar{\nu}_e\nu_\tau$	17.5±0.4%
$\mu^-\bar{\nu}_\mu\nu_\tau$	17.8±0.4%
$\rho^-\nu_\tau$	22.3±1.1%
$\pi^-\nu_\tau$	10.8±0.6%
4-mode total	68.4±1.37%

The two leptonic modes are 3-body decays and the two hadronic modes are even simpler 2-body decays. We can consider these decays in the rest frame of the τ. It is assumed that the τ spin is oriented along the z axis. It is straightforward to show that the angular distribution of the charged hadron from the 2-body decay $\tau^\pm \to h^\pm\nu$ is given by the following expression,

$$\frac{1}{N}\frac{dN}{d\cos\theta^*} = \frac{1}{2}\cdot(1-\alpha_h P_\tau Q_\tau \cos\theta^*), \tag{4.38}$$

where: θ^* is the angle between the spin direction and the hadron direction; P_τ is the τ polarization; Q_τ is the charge of the τ; and the constant α_h is given by the following expression,

$$\alpha_h = \begin{cases} 1, & \text{for } h = \pi \\ \frac{m_\tau^2 - 2m_\rho^2}{m_\tau^2 + 2m_\rho^2} = 0.457, & \text{for } h = \rho \end{cases}$$

where m_τ and m_ρ are the τ and ρ masses, respectively. Ignoring the lepton mass, the energy-angle distributions of the 3-body leptonic decays are given by the fol-

lowing expression,

$$\frac{1}{N}\frac{d^2N}{dyd\cos\theta^*} = y^2[3 - 2y - P_\tau Q_\tau(1-2y)\cos\theta^*], \tag{4.39}$$

where y is the scaled energy of the outgoing lepton $y = 2E_\ell/m_\tau$.

Equations (4.38) and (4.39) show that the angular distributions of the τ decay products are sensitive to P_τ. Unfortunately, the τ-leptons that are produced in Z^0 decay are not at rest but have the beam energy (as smeared by the initial state radiation). In the case of the 2-body decays, we have a sufficient number of constraints to calculate $\cos\theta^*$ from the observed hadron momentum. Unfortunately, the non-observation of the two neutrinos from the leptonic decays makes this impossible for the 3-body decays. We therefore consider the laboratory energy distributions of the observed particles.

Let x_τ be the ratio of the observed energy of the τ decay product to the beam energy. It is then straightforward to derive a simple relationship between x_τ and $\cos\theta^*$ *that is valid for the 2-body decays*,

$$x_\tau = \frac{E_h}{E_b} = \frac{1}{2}\cdot\left[1 + z + (1-z)\cos\theta^*\right], \tag{4.40}$$

where z is the ratio of square of the hadron mass to the square of τ mass, $z \equiv m_h^2/m_\tau^2$. Changing variables from $\cos\theta^*$ to x_τ, equation (4.38) can be expressed as the laboratory energy distribution,

$$\frac{1}{N}\frac{dN}{dx_\tau} = \frac{1}{1-z}\cdot\left[1 - \alpha_h P_\tau Q_\tau\left(\frac{2x_\tau - 1 - z}{1-z}\right)\right], \tag{4.41}$$

where x_τ is constrained to the interval $z \le x_\tau \le 1$.

For the 3-body leptonic decays, we can express x_τ in terms of y and $\cos\theta^*$,

$$x_\tau = \frac{y}{2}\cdot(1 + \cos\theta^*), \tag{4.42}$$

where the lepton mass is ignored. Changing variables from $\cos\theta^*$,y to x_τ,y and integrating over all values of y (note that the allowed range for y is 0-x), equation

(4.39) can be expressed as a laboratory energy distribution,

$$\frac{1}{N}\frac{dN}{dx_\tau} = \left[\frac{5}{3} - 3x^2 + \frac{4}{3}x^3\right] - P_\tau Q_\tau \left[\frac{1}{3} - 3x^2 + \frac{8}{3}x^3\right]. \qquad (4.43)$$

Statistical Sensitivity

The sensitivity of the laboratory energy distributions given in equations (4.41) and (4.43) to the average τ polarization P_τ (note that we've simplified the notation) that is expected from the Standard Model is shown in Figure 18 for the $\tau \to \ell\nu\nu$ and the $\tau \to \pi\nu$ decays. The curves correspond to the polarization that is expected for $\sin^2\theta_w = 0.20, 0.23, 0.25, 0.30$, respectively. At $\sin^2\theta_w = 0.25$, the average polarization is zero, and the π spectrum is flat. Note that the π final state seems much more sensitive than do the leptonic final states.

There are generally two approaches to the extraction of P_τ from the measured x_τ distributions. The first is to fit the measured distributions to the functions defined in equations (4.41) and (4.43). The second approach is to measure the first moments of the x_τ distributions. It is straightforward to calculate the average value of x_τ for each distribution,

$$\langle x_\tau \rangle = a + bP_\tau Q_\tau = \begin{cases} \frac{1}{2}(1+z) - \frac{1}{6}\alpha_h P_\tau Q_\tau (1-z), & \text{2-body decays} \\ \frac{7}{20} + \frac{1}{20}P_\tau Q_\tau, & \text{3-body decays.} \end{cases} \qquad (4.44)$$

Numerically, the mean values of x_τ for the $\pi\nu$, $\rho\nu$, and $\ell\nu\nu$ final states are,

$$\langle x_\tau \rangle_\pi = 0.50 - 0.17 \cdot P_\tau Q_\tau$$
$$\langle x_\tau \rangle_\rho = 0.59 - 0.062 \cdot P_\tau Q_\tau$$
$$\langle x_\tau \rangle_\ell = 0.35 - 0.050 \cdot P_\tau Q_\tau.$$

The average x_τ distribution for the $\pi\nu$ final state has the most sensitivity to P_τ.

A third technique that can be applied only to the 2-body decays is to convert the measured value of x_τ into a value of $\cos\theta^*$ (using equation (4.40)) and to form the forward-backward asymmetry of the emitted hadrons,

$$A^*_{FB} \equiv \frac{N_h(Q_\tau \cos\theta^* < 0) - N_h(Q_\tau \cos\theta^* > 0)}{N_h(Q_\tau \cos\theta^* < 0) + N_h(Q_\tau \cos\theta^* > 0)} = \frac{\alpha_h}{2} \cdot P_\tau \cdot \cos\theta^*_{max}, \qquad (4.45)$$

where N_h is the number of detected hadrons with a positive or negative value for the product $Q_\tau \cos\theta^*$ and where $\cos\theta^*_{max}$ is the maximum accepted value of $\cos\theta^*$ (this is the appropriate form of the acceptance function F that was defined for the Z forward-backward asymmetries).

In order to evaluate the statistical precision that is possible with each of the three techniques, we assume that our ideal detector has complete acceptance (this is to avoid considerable complexity). The uncertainty on the measurement of $\langle x_\tau \rangle$ is given by standard error of the mean which is the ratio of the variance of the distribution Δx_τ and the square root of the number of events N that are used to measure the distribution. The precision that is obtainable from a likelihood fit is given by an expression that we've used several times (see equation (3.14)). The precision of a measurement of A^*_{FB} is given by $N^{-1/2}$. These estimates are listed in Table XV.

Table XV

Technique	Expected Error	δP_τ (2-body)	δP_τ (3-body)
$\langle x_\tau \rangle$	$\frac{1}{b}\frac{\Delta x}{\sqrt{N}}$	$\frac{1}{\alpha_h}\sqrt{\frac{3}{N}}$	$\simeq \sqrt{\frac{20}{N}}$
$\mathcal{L}(x_\tau)$	$[N \int dx_\tau (\frac{\partial \mathcal{L}}{\partial P_\tau})^2/\mathcal{L}]^{-1/2}$	$\frac{1}{\alpha_h}\sqrt{\frac{3}{N}}$	$\simeq \sqrt{\frac{20}{N}}$
A^*_{FB}	$\frac{2}{\alpha_h}\frac{1}{\sqrt{N}}$	$\frac{1}{\alpha_h}\frac{2}{\sqrt{N}}$	not applicable

Note that the measurement of the average $\langle x_\tau \rangle$ determines P_τ as precisely as a full likelihood fit to the x_τ distribution. The measurement of A^*_{FB} for the 2-body decays is less sensitive than either of the other techniques. Using the expressions given in Table XV, we can estimate the statistical precision of an ideal

experiment. (In reality, a minimum energy cut is necessary to reject background, hence the entire range of x_τ cannot be used.) Assuming that our experiment acquires a sample of 6×10^6 hadronic events, a total of 2.49×10^5 $\tau^+\tau^-$ pairs would be produced. We assume that the overall selection efficiency is 60%. The number of produced and observed events for each decay mode are listed in Table XVI. The estimated error on P_τ from each mode is listed in the last column. We conclude that the $\pi\nu$ and $\rho\nu$ final states are the most statistically sensitive decay modes.

Table XVI

Decay Mode	Produced Events	Observed Events	δP_τ
$\tau \rightarrow \pi\nu$	5.38×10^4	3.23×10^4	0.0096
$\tau \rightarrow \rho\nu$	1.11×10^5	6.66×10^4	0.0147
$\tau \rightarrow e\nu\nu$	8.79×10^4	5.28×10^4	0.0195
$\tau \rightarrow \mu\nu\nu$	8.79×10^4	5.28×10^4	0.0195

Systematic Errors

There are several sources of systematic uncertainty in the measurement of the average τ polarization. The two most sensitive final states are quite similar. The $\rho^\pm$ meson decays into a pair of pions, $\pi^\pm\pi^0$. The $\rho\nu$ final state therefore differs from the from the $\pi\nu$ final state only by the presence of an additional π^0. The dominant systematic uncertainty is due to contamination of the $\pi\nu$ sample by the $\rho\nu$ final state. Other systematic errors are the uncertainty on the energy scale of the decay products (from radiative effects and detector calibration uncertainties) and an uncertainty due to detector biases. The combined systematic error has been estimated to be in the range[29] $\delta P_\tau \simeq 0.005$-$0.008$.

Bottom Line

The measurement of the average polarization of the τ-leptons in Z^0 decay is a reasonably sensitive test of the Standard Model. It appears that the polarization could be measured to the 0.012 level with a sample of 200 pb^{-1} at LEP. This corresponds to an uncertainty on the effective $\sin^2\theta_w$ of 0.0015.

5. Conclusions

The recent measurements of the mass of the Z^0 have determined the parameters of the electroweak portion of the Standard Model at tree-level. Precise measurements of other physical quantities will test the electroweak theory at the loop level. The most promising of these are the measurements of the W boson mass that will be performed by experiments at the Tevatron and at LEP II and the measurements of the ratio the vector and axial-vector couplings of the Z^0 that will be performed with a variety of techniques at the SLC and LEP I. It is interesting to compare the sensitivities of these measurements to loop-level corrections.

We have seen that measurements of M_W to a level of precision $\delta M_W \simeq$ 100-150 MeV are possible in the next several years. The dependence of M_W upon the top quark mass is shown in Figure 19. The solid curves enclose the 68.3% confidence region that is expected for a $\pm$20 MeV uncertainty on M_Z (it is assumed that $M_Z = 91.17 \pm 0.20$ GeV) as m_{top} is varied from 60 GeV to 240 GeV. The Higgs boson mass is assumed to be 500 GeV. The 68.3% confidence interval that corresponds to a $\pm$100 MeV measurement is shown as a solid error bar. The theoretical error that is due to the uncertainty on the renormalization of the electromagnetic coupling constant to the W mass scale is also shown. Note that a measurement error $\delta M_W = \pm 100$ MeV corresponds to an uncertainty on m_{top} of roughly 16 GeV. The analagous dependence of M_W upon m_{Higgs} is shown in Figure 20. The dashed curves enclose the 68.3% confidence region that is expected as m_{Higgs} is varied from 100 GeV to 900 GeV. The top quark mass is fixed to 150 GeV. Note that future measurements of M_W are unlikely to constrain the Higgs mass.

The ratio of the vector and axial-vector couplings of the Z^0 is best determined from measurements of the b-quark forward-backward asymmetry and the left-right polarization asymmetry. Note that the precision of a measurement of A_{FB}^b that is based upon a sample of 6×10^6 hadronic Z decays is comparable to a measurement of A_{LR} that is based upon 10^5 Z decays. We therefore use the left-right asymmetry as a standard to determine the loop-level sensitivity of this class of measurements.

The experimental confidence intervals that are presented in Table XIII are compared with the theoretical expectation for A_{LR} in Figures 21 and 22. The solid curves in Figure 21 enclose the 68.3% confidence region that is expected for m_{Higgs} = 500 GeV and m_{top} varying between 60 GeV and 240 GeV. The finite width of the region is due to a ±20 MeV uncertainty on the Z^0 mass (we assume M_Z = 91.17 ± 0.02 GeV). The solid curves in Figure 22 enclose the 68.3% confidence region that is expected for m_{top} = 150 GeV and m_{Higgs} varying from 100 GeV to 900 GeV. The size of the theoretical error on A_{LR} (±0.002) is shown as the dotted vertical error bar in each figure. The sizes of the experimental 68.3% confidence intervals that correspond to the various values of N_{tot} are indicated by the solid vertical error bars. Since the τ polarization asymmetry is formally equivalent to A_{LR}, we plot the confidence region that is expected from a measurement with a 6M Z^0 sample. It is clear that A_{LR} is quite sensitive to m_{top}. A measurement with 300K Z^0 events constrains the top quark mass to a region of roughly $\delta m_{top} = \pm 17$ GeV which is comparable to a 100 MeV determination of M_W. The sensitivity to m_{Higgs} is clearly much smaller. A very high statistics measurement of A_{LR} could provide, at best, an indication of m_{Higgs}.

It is important to note that the sensitivities of M_W and the Z pole asymmetries to higher order corrections and to new physical processes are quite different. They are, to a large degree, quite **complementary**. This is particularly true if deviations from the Standard Model expectations are found. In that case, several precise measurements would be required to constrain the space of new physical possibilities. An example of this complementarity is shown[30] in Figure 23 for the case that the Standard Model is extended to include a 500 GeV, χ-type Z' boson.[31] The contours show the expected values of M_W and A_{LR} as m_{top} is varied from 50 GeV to 200 GeV (m_{Higgs} is fixed to 100 GeV). The three contours in each group correspond to the three values of the Z^0 mass, M_Z = 91.17 ± 0.02 GeV. Each group represents a different value of the $Z^0 - Z'$ mixing parameter $\sin\theta_m$. The four groups correspond to the four values $\sin\theta_m = 0.0, -0.005, -0.010, -0.015$ (top to bottom). The precision expected from a 300K event measurement of A_{LR} and a

100 MeV measurement of M_W is shown by the error bars in the corner of the plot. It is clear that the unfolding of deviations from the Standard Model expectations is greatly aided by the presence of several different high precision measurements.

Acknowledgements: The author would like to thank Michael Peskin, Gary Feldman, and Guy Blaylock for several useful and informative discussions. Additionally, Guy deserves special thanks for his careful scrutiny this manuscript.

REFERENCES

1. E.R. Cohen and B.N. Taylor, *Rev. Mod. Phys.* **59**, 1121 (1987).
2. *Review of Particle Properties*, G.P. Yost et al., *Phys. Lett.* **B204**,1 (1988).
3. G. Abrams et al., *Phys. Rev. Lett.* **63**, 2173 (1989).
4. D. Decamp et al., *Phys. Lett.* **B231**, 519 (1989) and *Phys. Lett.* **B235**, 399 (1990).
5. P. Aarnio et al., *Phys. Lett.* **B231**, 539 (1989).
6. B. Adeva et al., *Phys. Lett.* **B231**, 509 (1989) and L3 Preprint #004, December(1989).
7. M.Z. Akrawy et al., *Phys. Lett.* **B231**, 530 (1989).
8. The quoted value is a weighted average (assuming a 27 MeV LEP energy scale uncertainty) of the results given in References 3-7.
9. J. Alitti et al., CERN-EP/90-22, March 1990.
10. J.C. Collins and D.E. Soper, *Phys. Rev.* **D16**, 2219 (1977).
11. C. Albajar et al., *Z. Phys.* **C44**, 15 (1989).
12. F. Abe et al., *Phys. Rev. Lett.* **63**, 720 (1989).
13. A. Sirlin, *Phys. Rev.* **D22**, 971 (1980).
14. W.J. Marciano and A. Sirlin, *Phys. Rev.* **D29**, 945 (1984).
15. F. Abe et al., *Phys. Rev. Lett.* **62**, 154 (1990).
16. M. Peskin, SLAC-PUB-5210, March 1990.
17. B. Adeva et al., L3 preprint 005, February 1990.
18. G.S. Abrams et al., *Phys. Rev. Lett.* **63**, 2780 (1989).
19. T. Muta, R. Najima, and S. Wakaizumi, *Mod. Phys. Lett.* **A1**, 203 (1986).

20. P. Roudeau et al., *Proceedings of the ECFA Workshop on LEP 200*, edited by A. Böhm and W. Hoogland, CERN 87-08, June 1987, pg 85.

21. J. Alitti et al., CERN preprint CERN-EP/90-20, February 1990.

22. J. Drees, K. Mönig, H. Staeck, and S. Überschär, Vol. I *Polarization at LEP*, CERN 88-06, September 1988, pg 317.

23. A. Blondel, B.W. Lynn, F.M. Renard, and C. Verzegnassi, Montpellier preprint PM/87-14, March 1987.

24. M. Böhm and W. Hollik, Z Physics at LEP 1, CERN 89-08, Sept. 1989, Vol I, pg 203.

25. R. Kleiss, F.M. Renard, and C. Verzegnassi, *Nucl. Phys.* **B286**, 669 (1987).

26. D. Kennedy, B.W. Lynn, and C.J.C. Im, *Nucl. Phys.* **B321**, 83 (1989).

27. H. Burkhardt, F. Jegerlehner, G. Penso, and C. Verzegnassi, Vol. I *Polarization at LEP*, CERN 88-06, September 1988, pg 145.

28. C.Y. Prescott et al., *Phys. Lett.* **77B**, 347 (1978); and *Phys. Lett.* **84B**, 524 (1979).

29. F. Boillot and Z. Was, *Z. Phys.* **C43**, 103 (1989).

30. The author is grateful to M. Peskin for providing this calculation.

31. P. Langacker, R.W. Robinett, and J.L. Rosner, Phys. Rev. D30, 1470 (1984).

FIGURE CAPTIONS

1) The Drell-Yan mechanism for the production of W and Z bosons in $p\bar{p}$ collisions. The incident proton and antiproton have momenta k_1 and k_2, respectively. A parton carrying the fraction x_1 of the proton momentum collides with a parton carrying the fraction x_2 of the antiproton momentum. The two lowest order subprocesses that produce gauge bosons are shown in parts a) and b).

2) The scaled longitudinal momentum distribution $x_2 - x_1$ for W^- bosons produced at $\sqrt{s} = 630$ GeV. The mean of the distribution is 0.06 indicating that the average longitudinal momentum is along the antiproton direction. Note that $x_2 - x_1 = 0.4$ corresponds to a W boson longitudinal momentum of 125 GeV.

3) The electron transverse momentum distribution from W bosons produced at $\sqrt{s} = 630$ GeV. The P_t^e distribution is shown for three phenomenological W boson transverse momentum distributions. Top to bottom, the average values of the W boson transverse momentum are: 0 GeV (dashed curve), 7 GeV (dashed-dotted curve), and 14 GeV (solid curve).

4) The electron and neutrino transverse momentum distributions of 1203 $W \rightarrow e\nu$ candidates measured by the UA2 Collaboration[9].

5) The transverse mass distributions corresponding to the P_t^e distributions shown in Figure 3. Top to bottom, the average values of the W boson transverse momentum are: 0 GeV (dashed curve), 7 GeV (dashed-dotted curve), and 14 GeV (solid curve). The neutrino P_t resolution is assumed to be $\delta P_{t,xy}^{\nu} = 0.5\sqrt{E_t}$ GeV along the x and y axes.

6) The angular distribution of electrons from W decay as measured by the UA1 collaboration[11].

7) The electron and muon pair mass distributions in the Z^0 region that have been measured by the CDF Collaboration.[12]

8) The Z^0 lineshape as measured by the Mark II Collaboration.[3] The dashed curve is the result of a single parameter fit (for M_Z). The results of two and three parameter fits are indistinguishable and are shown as the solid curve.

9) The sensitivity function for M_Z as a function of center-of-mass energy about the Z pole, $E - M_Z$.

10) The sensitivity function for Γ_Z as a function of center-of-mass energy about the Z pole, $E - M_Z$.

11) The sensitivity function for $\sigma^0_{had}(M_Z^2)$ as a function of center-of-mass energy about the Z pole, $E - M_Z$.

12) The cross section for the process $e^+e^- \rightarrow W^+W^-$ as a function of $E_b - M_W$. The mass and width of the W are assumed to be 80 GeV and 2.1 GeV, respectively. Note that three curves are plotted: the dashed curve is the basic tree-level cross section; the dashed-dotted curve is the cross section including the effect of initial state radiation; and the solid curve is the cross section including initial state radiation and the effect of a finite W width.

13) The sensitivity function for M_W as a function of the single beam energy about the W pair threshold $E_b - M_W$.

14) The sensitivity function for Γ_W as a function of the single beam energy about the W pair threshold $E_b - M_W$.

15) The sensitivity function for the background parameter B as a function of the single beam energy about the W pair threshold $E_b - M_W$.

16) The forward-backward asymmetries for leptons, u-quarks, and d-quarks are plotted as a functions of the center-of-mass energy about the Z^0 pole. The asymmetries are also shown for the case that the incident beams are polarized. The energy dependence of the left-right asymmetry and an improved polarized forward-backward asymmetry $\tilde{A}^f_{FB}$ (from Reference 23) are also shown. The Z^0 mass is assumed to be 94 GeV. Note that the unimproved

forward-backward asymmetries are much more sensitive to the center-of-mass energy than are the improved ones and the left-right asymmetries.

17) The left-right asymmetry A_{LR} is plotted as a function of $\sin^2\theta_w$ and M_Z (for some choice of m_t and m_h). The leptonic forward-backward asymmetry A^{FB} is shown for comparison.

18) The normalized laboratory energy distributions of the observed decay products of polarized τ-leptons. Figure (a) shows the energy distribution for the $\tau \rightarrow \ell\nu\nu$ decay. The various curves correspond to the polarization that is expected for $\sin^2\theta_w = 0.20, 0.23, 0.25, 0.30$. Figure (b) shows the same curves for the decay $\tau \rightarrow \pi\nu$. Note that $\sin^2\theta_w = 0.25$ corresponds to zero net polarization.

19) The W boson mass as a function of the top quark mass. The Higgs boson mass is assumed to be 500 GeV. The solid curves enclose the 68.3% confidence region that is expected for a ± 20 MeV uncertainty on M_Z (we assume $M_Z = 91.17 \pm 0.02$ GeV) as m_{top} is varied from 60 GeV to 240 GeV. The size of the experimental 68.3% confidence interval (± 100 MeV) is indicated by the solid vertical error bar. The size of the theoretical error (± 25 MeV) is also shown.

20) The W boson mass as a function of the Higgs boson mass. The top quark mass is assumed to be 150 GeV. The dashed curves enclose the 68.3% confidence region that is expected for a ± 20 MeV uncertainty on M_Z (we assume $M_Z = 91.17 \pm 0.02$ GeV) as m_{Higgs} is varied from 100 GeV to 900 GeV. The dotted vertical error bar shows the size of the theoretical error (± 25 MeV) on M_W. The size of the experimental 68.3% confidence interval (± 100 MeV) is indicated by the solid vertical error bar.

21) The left-right asymmetry as a function of the top quark mass (m_{top}). The Higgs boson mass (m_{Higgs}) is assumed to be 500 GeV. The solid curves enclose the 68.3% confidence region that is expected for a ± 20 MeV uncertainty on M_Z (we assume $M_Z = 91.17 \pm 0.02$ GeV) as m_{top} is varied from 60 GeV

to 240 GeV. The dotted vertical error bar shows the size of the theoretical error (± 0.002) on A_{LR}. The sizes of the experimental 68.3% confidence intervals that are expected for the various values of N_{tot} are indicated by the solid vertical error bars. The confidence interval that is expected from a measurement of the τ polarization asymmetry with 6M Z^0 events is also shown.

22) The left-right asymmetry as a function of the Higgs boson mass. The top quark mass is assumed to be 150 GeV. The dashed curves enclose the 68.3% confidence region that is expected for a ± 20 MeV uncertainty on M_Z (we assume $M_Z = 91.17 \pm 0.02$ GeV) as m_{Higgs} is varied from 100 GeV to 900 GeV. The dotted vertical error bar shows the size of the theoretical error (± 0.002) on A_{LR}. The sizes of the experimental 68.3% confidence intervals that are expected for the various values of N_{tot} are indicated by the solid vertical error bars. The confidence interval that is expected from a measurement of the τ polarization asymmetry with 6M Z^0 events is also shown.

23) The expected values of M_W and A_{LR} are shown as m_{top} is varied from 50 GeV to 200 GeV (m_{Higgs} is fixed to 100 GeV) for the case that the Standard Model is extended to include a χ-type Z' boson (see Reference 13). The mass of the Z' boson is assumed to be 500 GeV. The three contours in each group correspond to the three values of the Z^0 mass, $M_Z = 91.17 \pm 0.02$ GeV. The dots along each contour indicate the points $m_{top} = 50$, 100, 150, 200 GeV. The four groups of contours show four values of the $Z^0 - Z'$ mixing parameter, $\sin\theta_m = 0.00$, -0.005, -0.01, -0.015. The precision expected from a 300K event measurement of A_{LR} and a 100 MeV measurement of M_W is shown by the error bars in the corner of the plot.

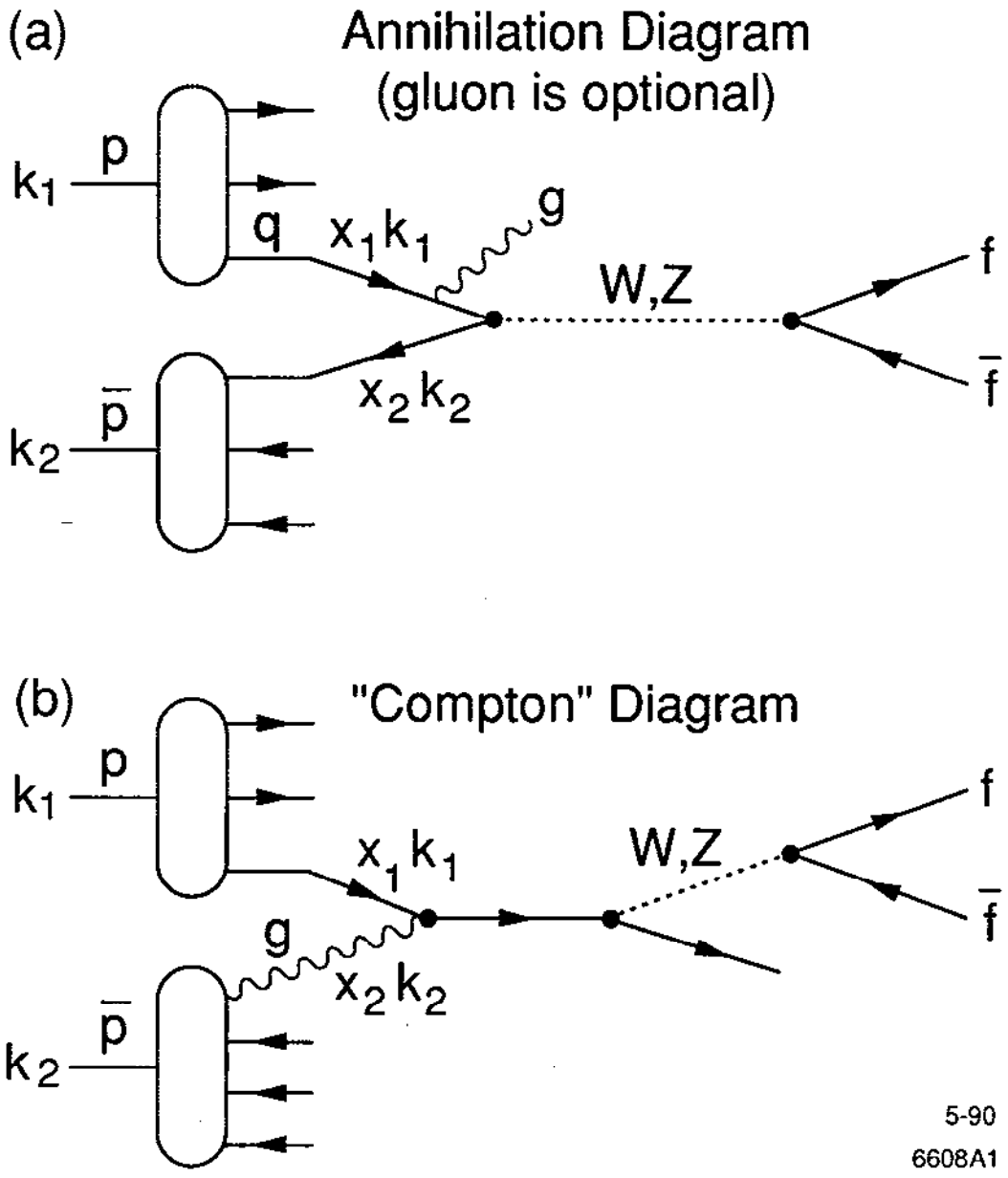
(a)
Annihilation Diagram
(gluon is optional)
k1
p
q
x1k1
g
W,Z
f
f̄
x2k2
k2
p̄
(b)
"Compton" Diagram
k1
p
x1k1
W,Z
f
f̄
g
x2k2
k2
p̄
5-90
6608A1

Fig. 1

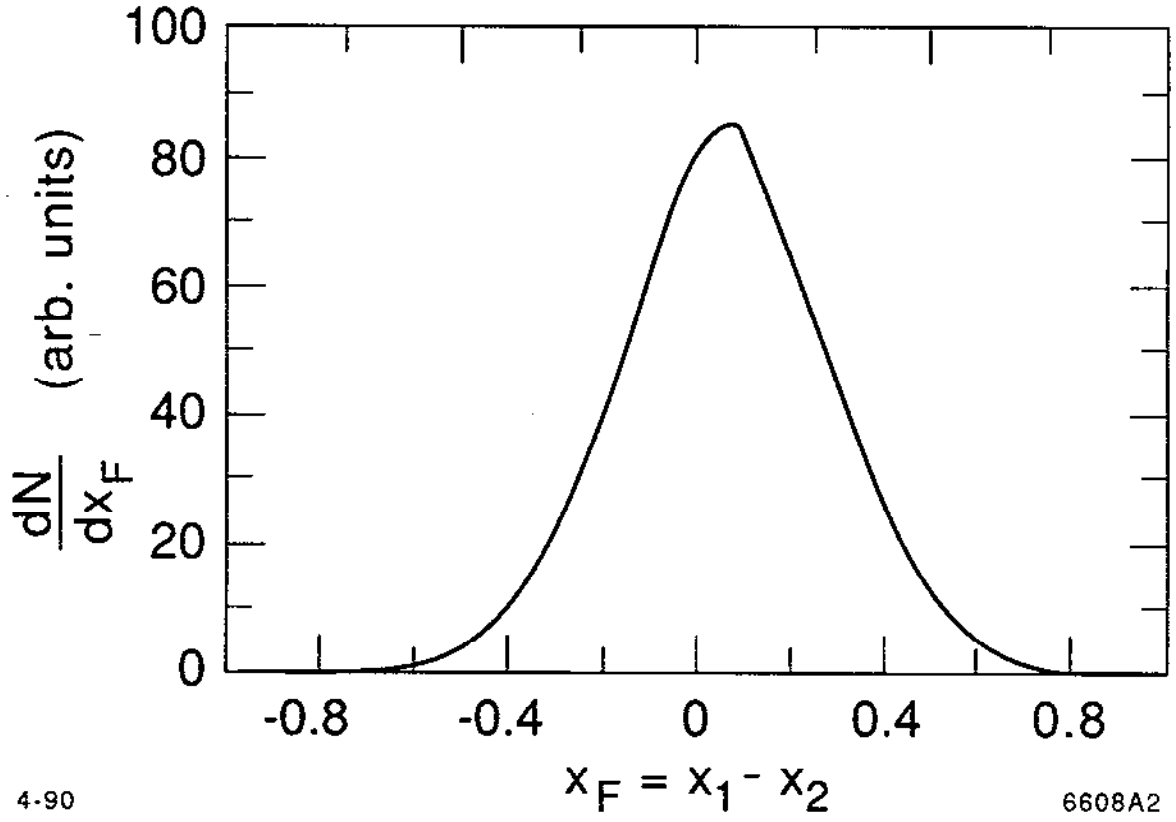
100
80
60
40
20
0
$\frac{dN}{dx_F}$ (arb. units)
-0.8
-0.4
0
0.4
0.8
$x_F = x_1 - x_2$
4-90
6608A2

Fig. 2

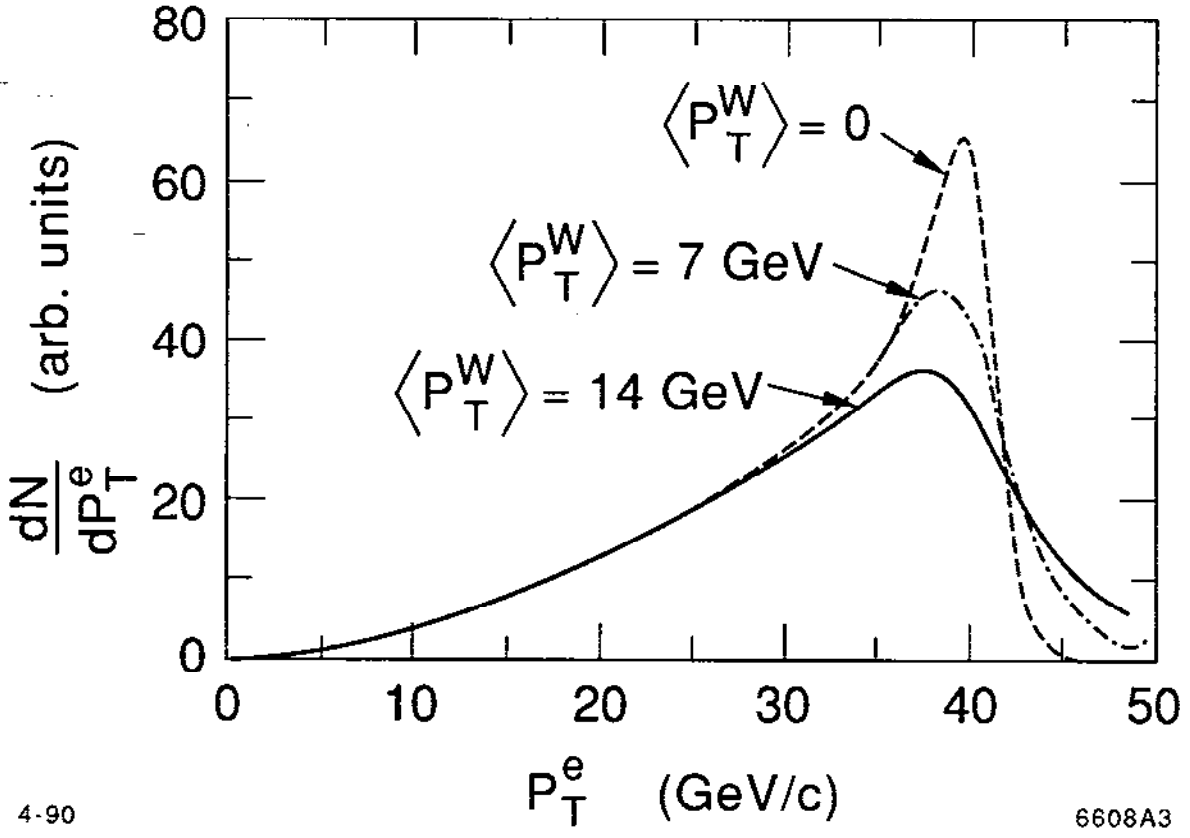
80
60
40
20
0
0
10
20
30
40
50
$\frac{dN}{dP_T^e}$ (arb. units)
$\langle P_T^W \rangle = 0$
$\langle P_T^W \rangle = 7$ GeV
$\langle P_T^W \rangle = 14$ GeV
P_T^e (GeV/c)
4-90
6608A3

Fig. 3

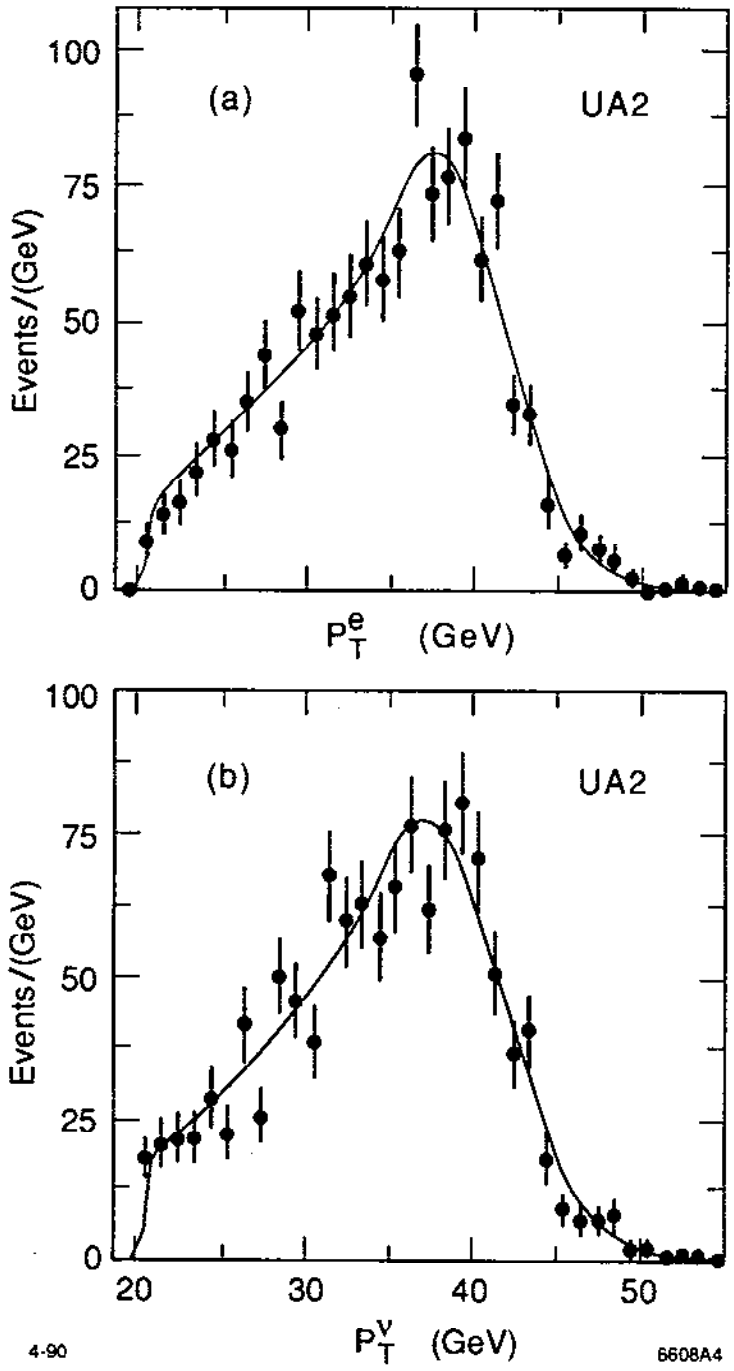
(a)
UA2
Events/(GeV)
100
75
50
25
0
P_T^e (GeV)
(b)
UA2
Events/(GeV)
100
75
50
25
0
20
30
40
50
P_T^ν (GeV)
4-90
6608A4

Fig. 4

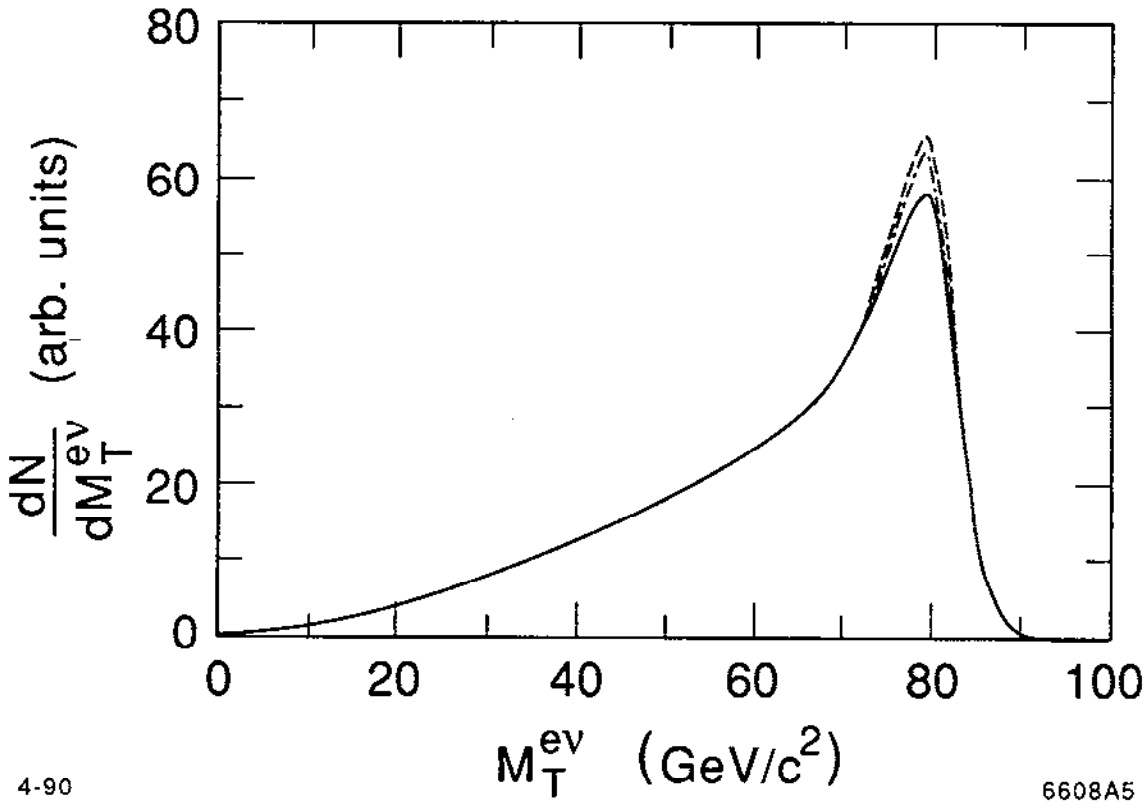
80
60
40
20
0
0
20
40
60
80
100
$\frac{dN}{dM_T^{ev}}$ (arb. units)
M_T^{ev} (GeV/c^2)
4-90
6608A5

Fig. 5

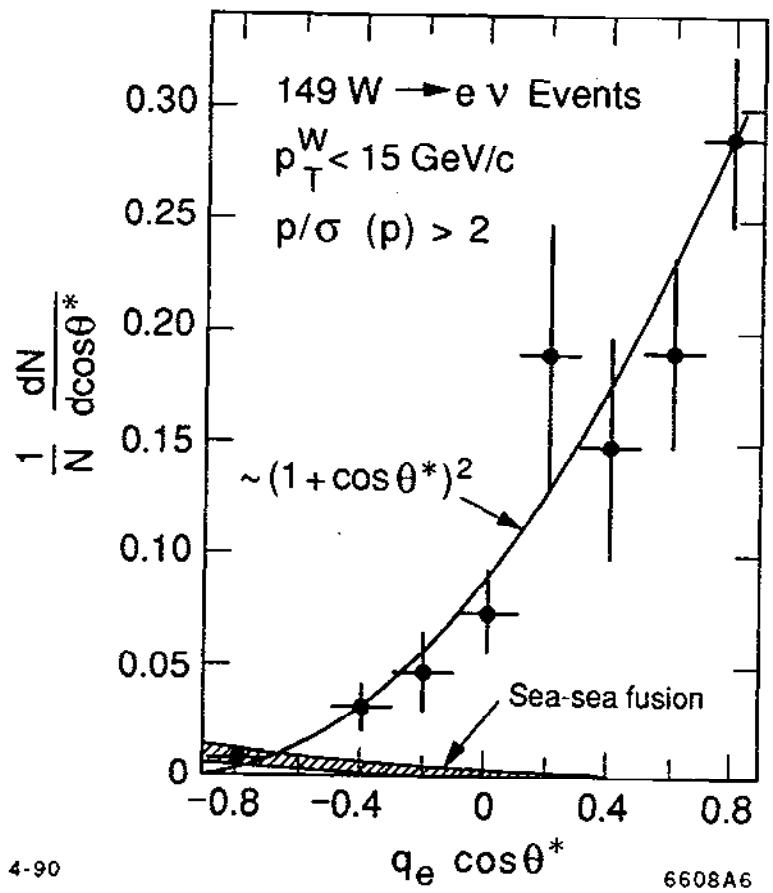
149 W → e ν Events
p_T^W < 15 GeV/c
p/σ (p) > 2
$\frac{1}{N}\frac{dN}{d\cos\theta^*}$
~ $(1+\cos\theta^*)^2$
Sea-sea fusion
0.30
0.25
0.20
0.15
0.10
0.05
0
−0.8
−0.4
0
0.4
0.8
$q_e \cos\theta^*$
4-90
6608A6

Fig. 6

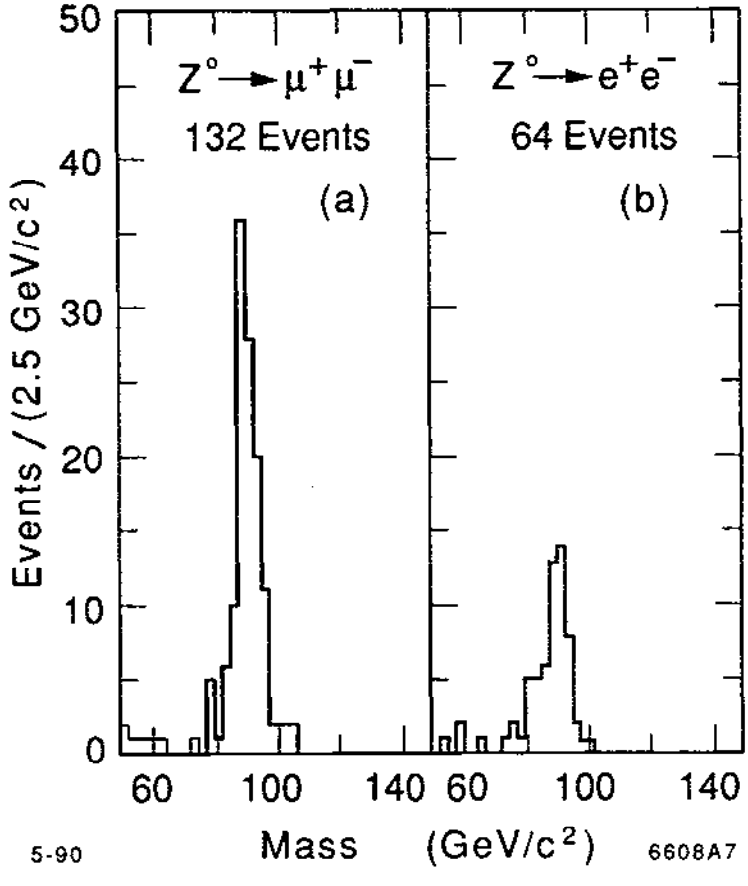
50
40
30
20
10
0
Events / (2.5 GeV/c²)
Z° → μ⁺μ⁻
132 Events
(a)
Z° → e⁺e⁻
64 Events
(b)
60
100
140
60
100
140
Mass (GeV/c²)
5-90
6608A7

Fig. 7

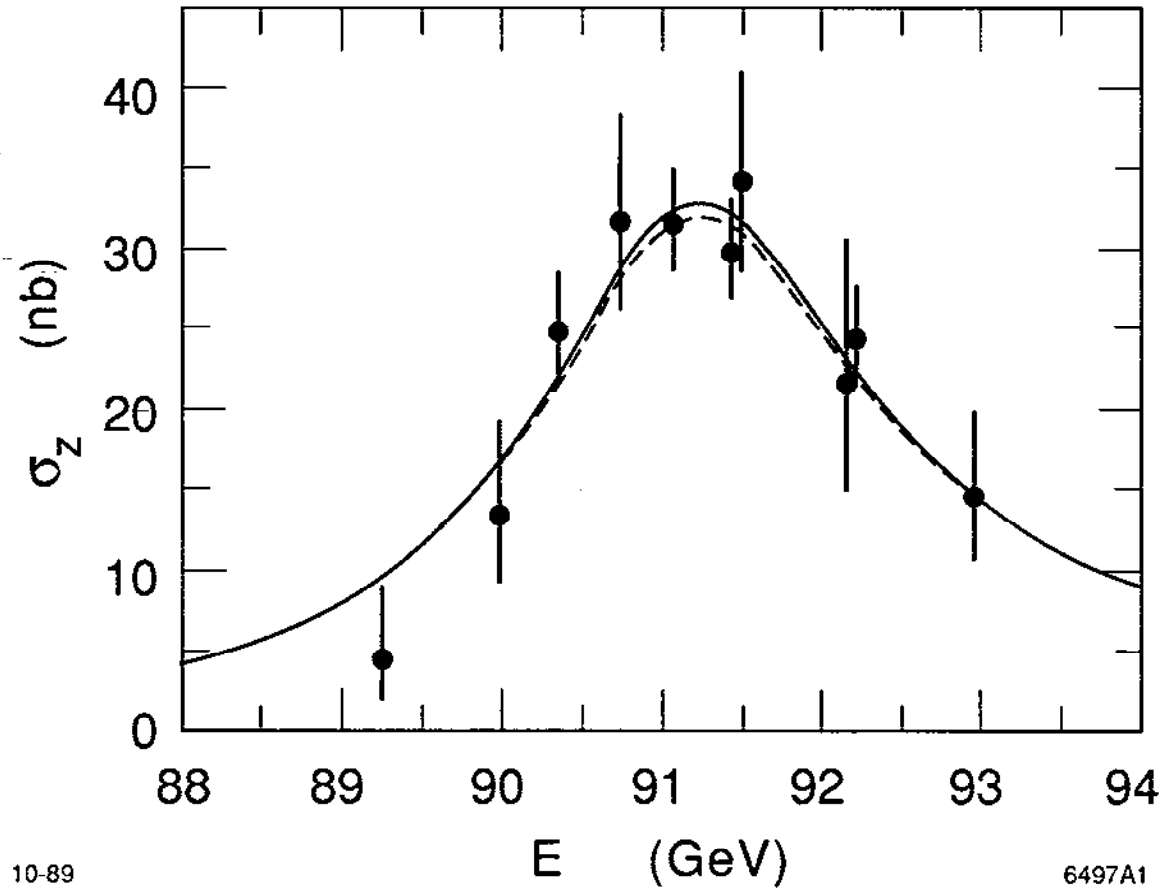

Fig. 8

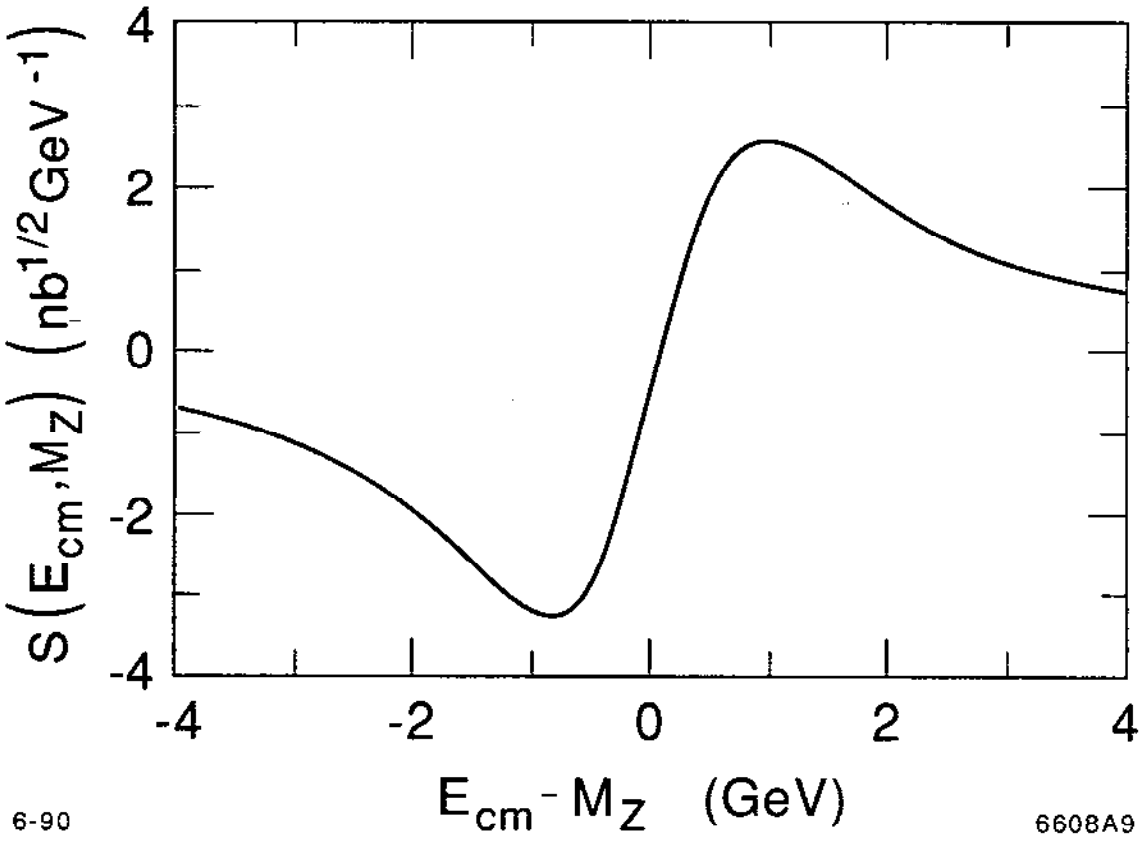

Fig. 9

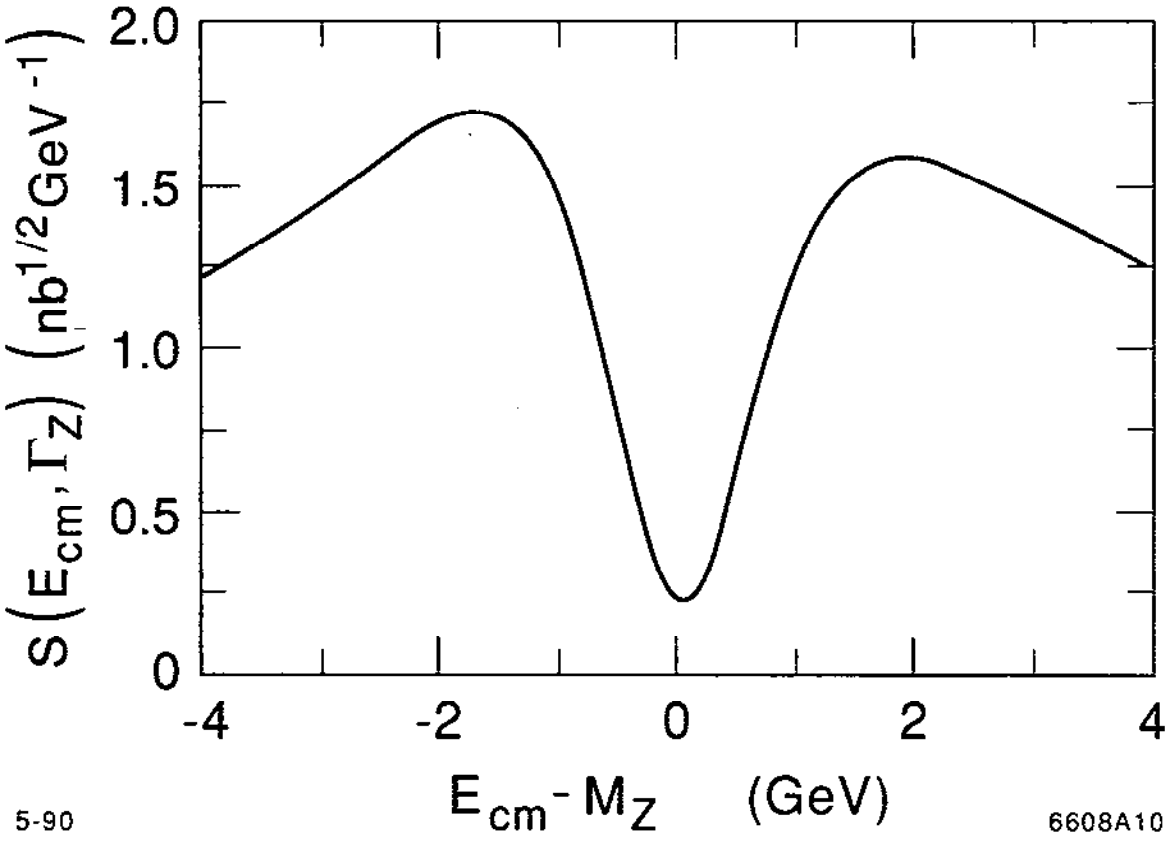
2.0
1.5
1.0
0.5
0
$S(E_{cm}, \Gamma_Z)$ $(nb^{1/2}GeV^{-1})$
-4
-2
0
2
4
$E_{cm} - M_Z$ (GeV)
5-90
6608A10

Fig. 10

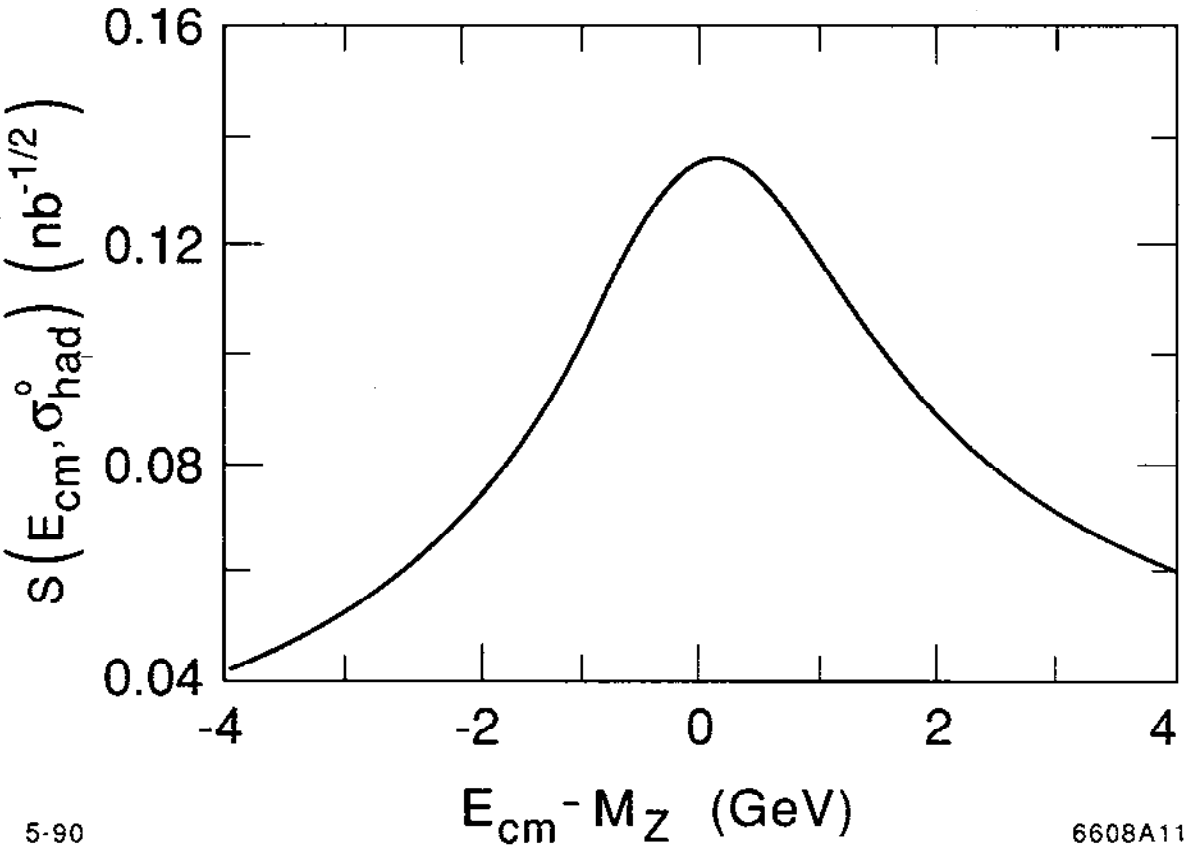
0.16
0.12
0.08
0.04
$S\left(E_{cm}, \sigma^{\circ}_{had}\right)\ \left(nb^{-1/2}\right)$
-4
-2
0
2
4
$E_{cm} - M_Z$ (GeV)
5-90
6608A11

Fig. 11

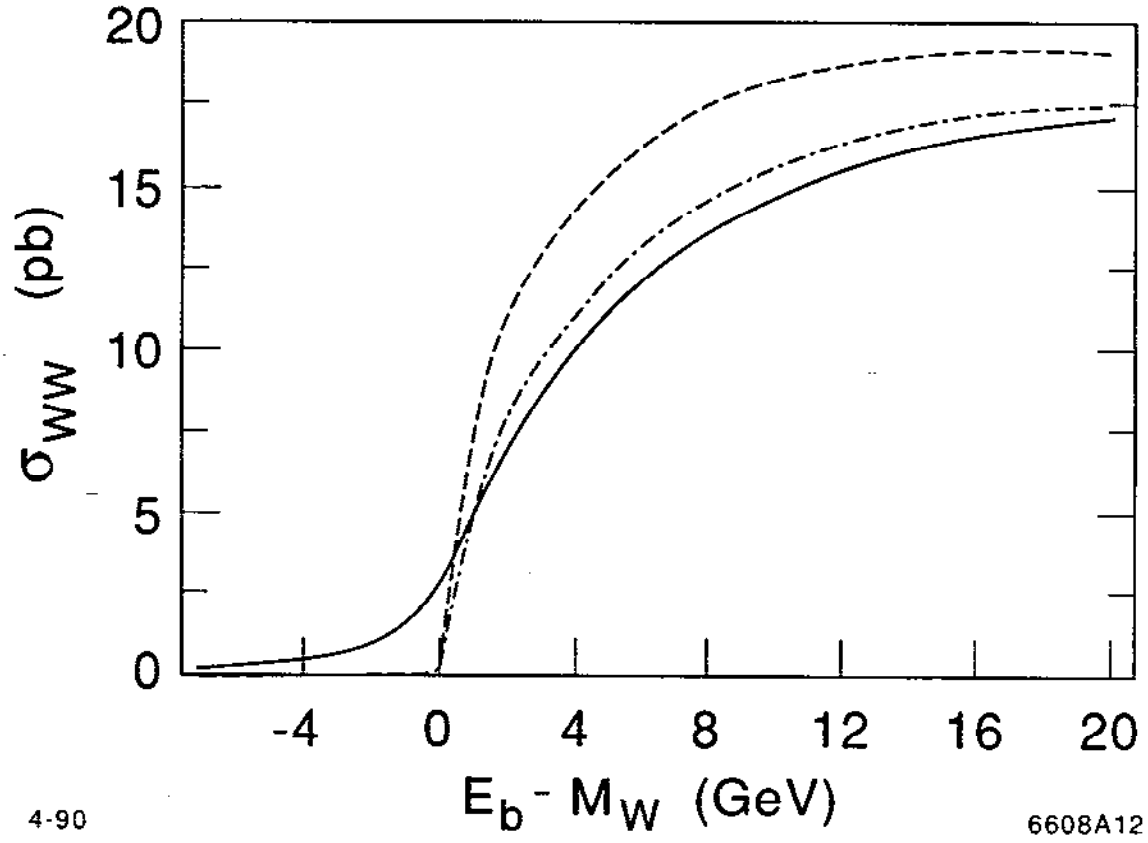

Fig. 12

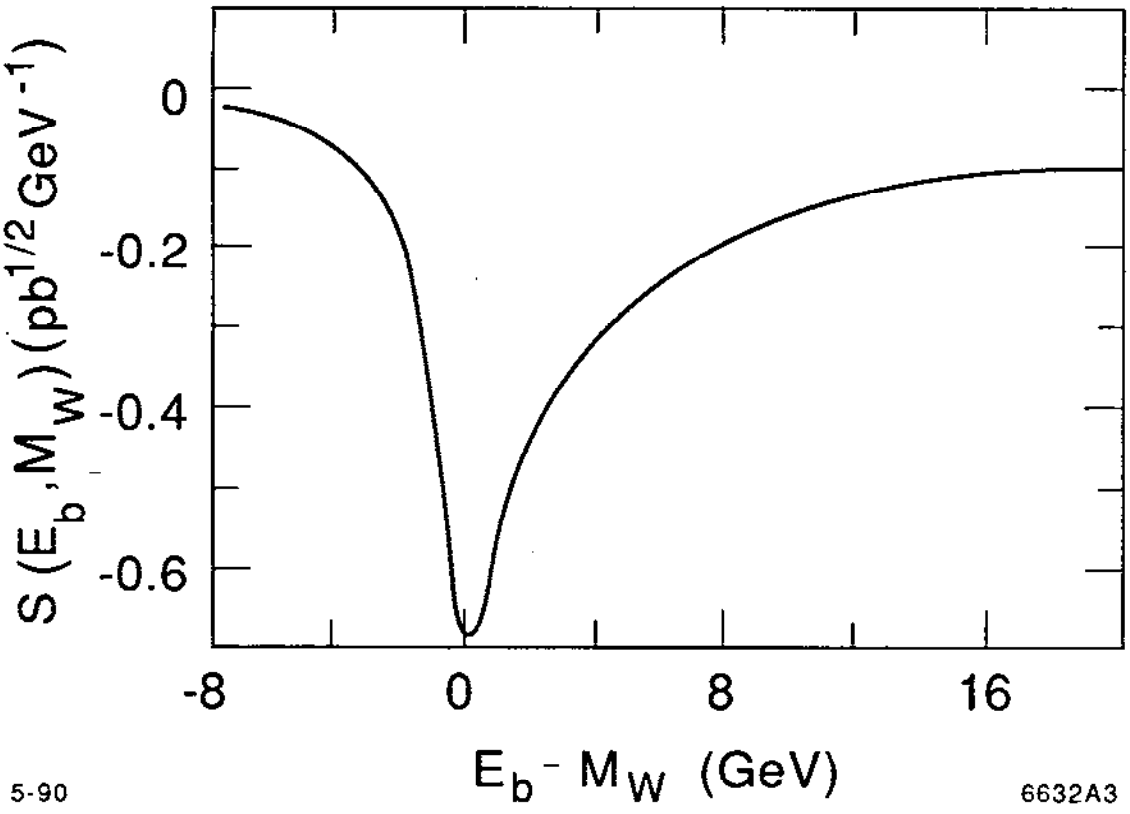

Fig. 13

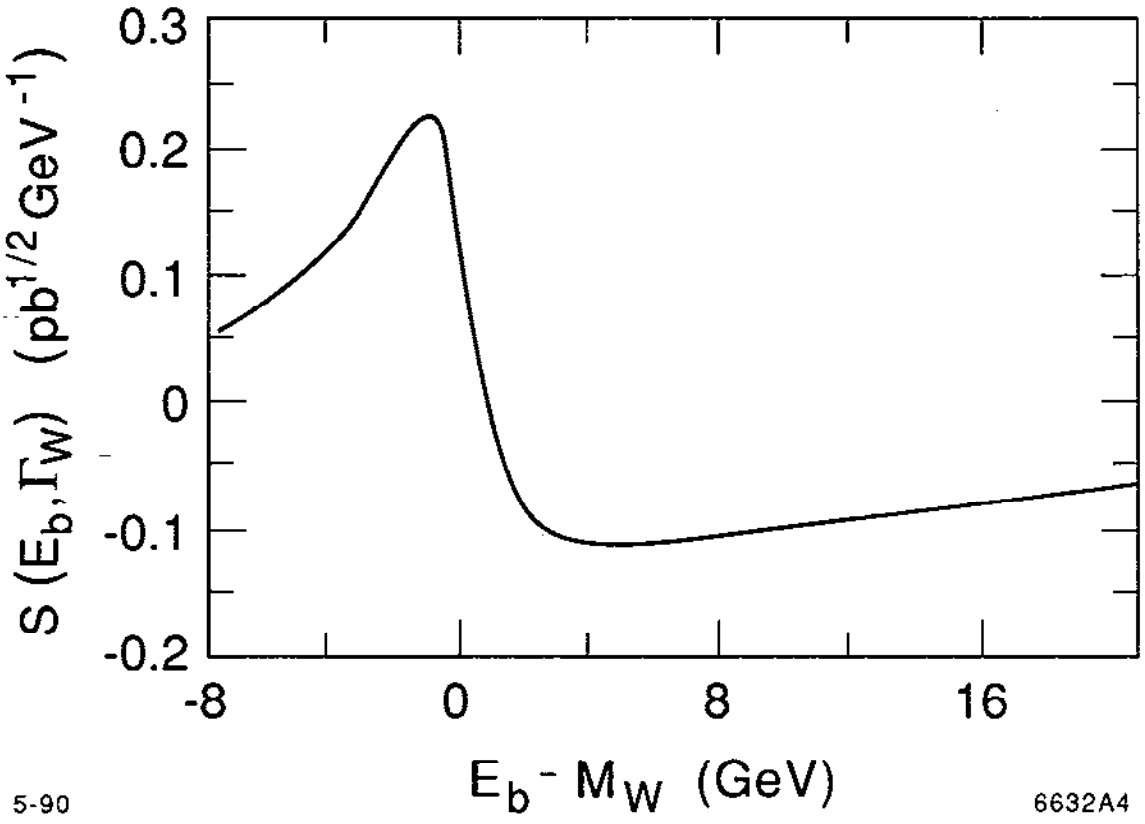

Fig. 14

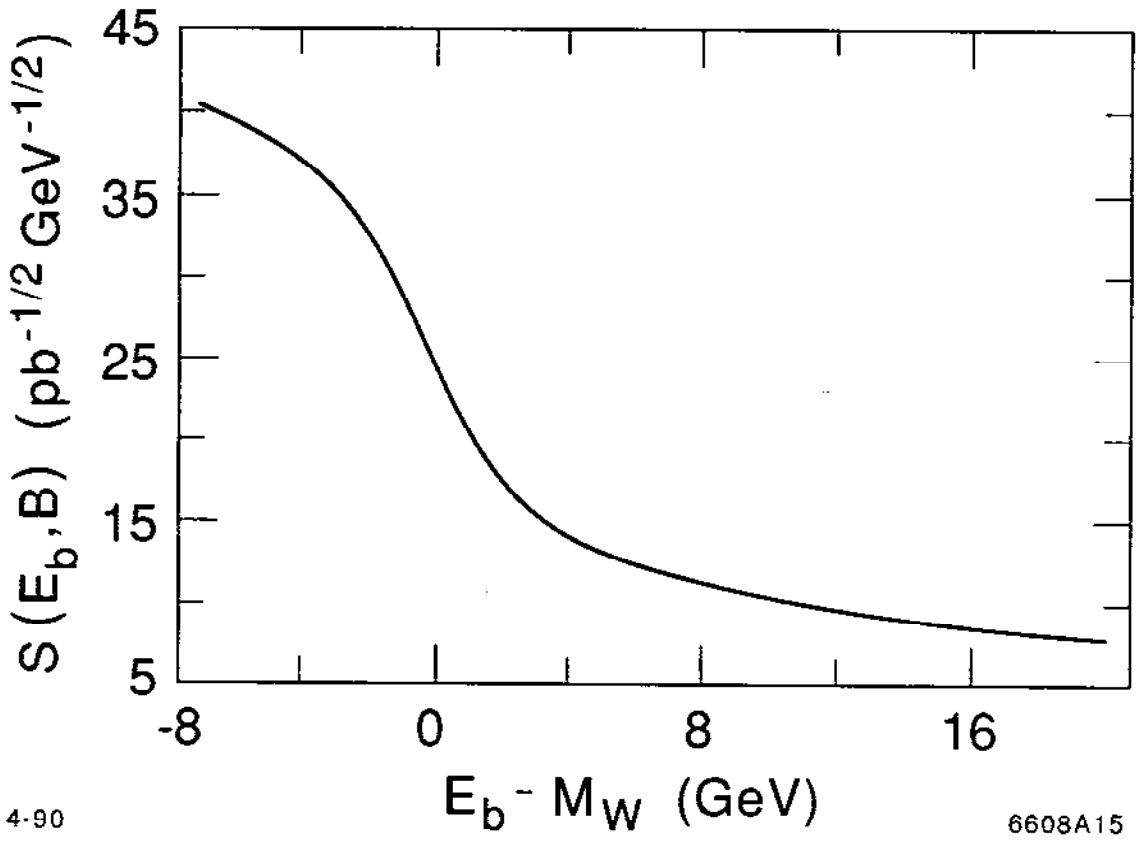

Fig. 15

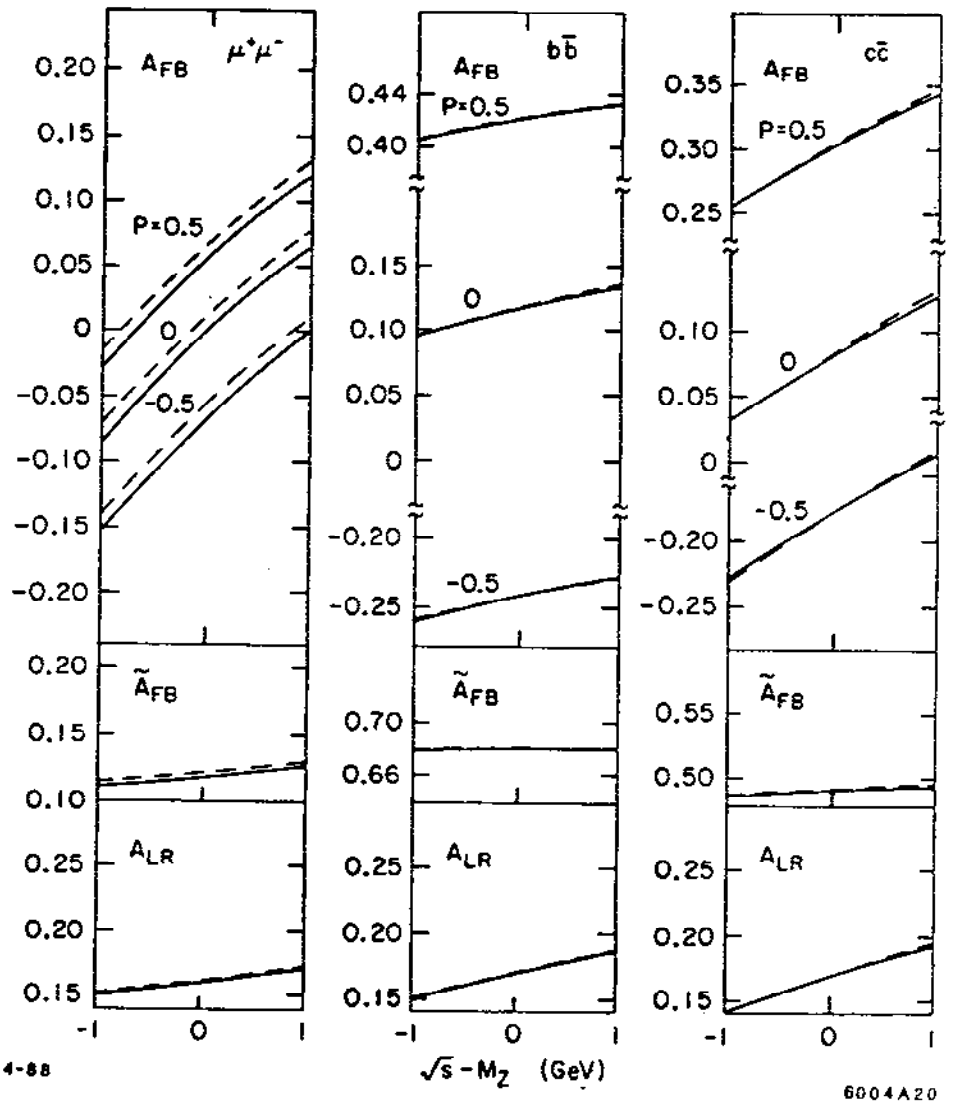
A_{FB} $\mu^+\mu^-$
P=0.5
0
-0.5
$\tilde{A}_{FB}$
A_{LR}
A_{FB} $b\bar{b}$
P=0.5
0
-0.5
$\tilde{A}_{FB}$
A_{LR}
A_{FB} $c\bar{c}$
P=0.5
0
-0.5
$\tilde{A}_{FB}$
A_{LR}
$\sqrt{s} - M_Z$ (GeV)
4-88
6004A20

Fig. 16

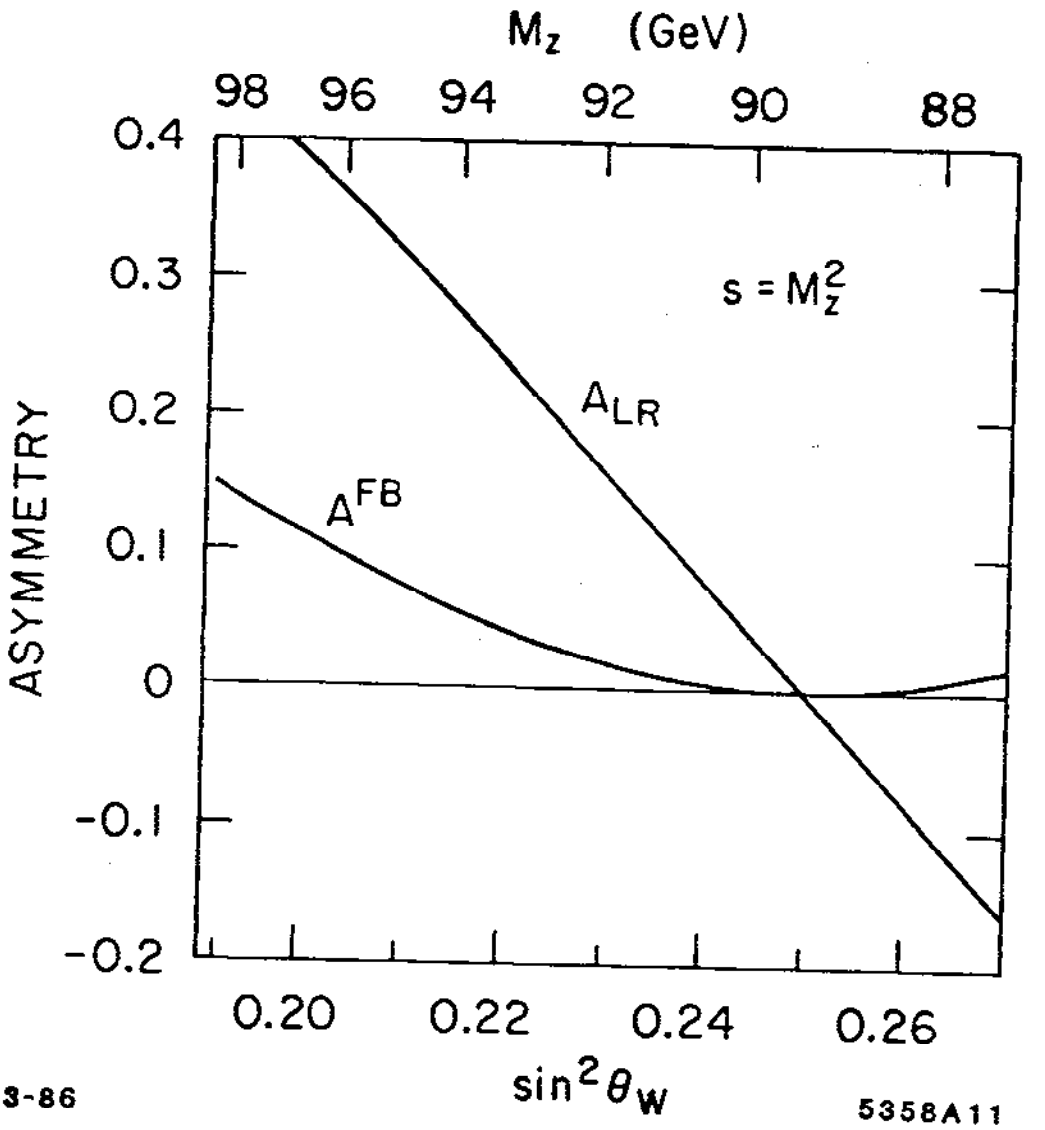
M_z (GeV)
98
96
94
92
90
88
0.4
0.3
0.2
0.1
0
-0.1
-0.2
ASYMMETRY
$s = M_z^2$
A_{LR}
A^{FB}
0.20
0.22
0.24
0.26
$\sin^2\theta_W$
3-86
5358A11

Fig 17

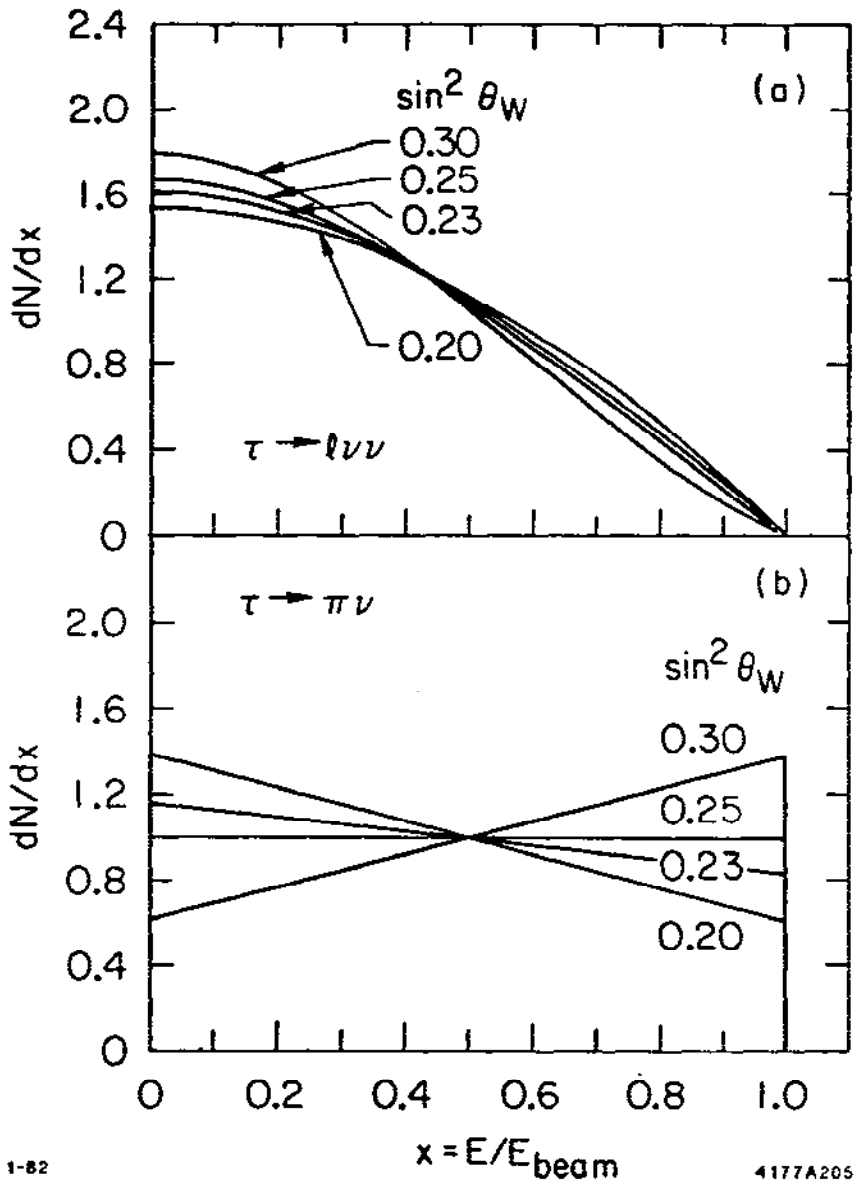
2.4
2.0
1.6
1.2
0.8
0.4
0
dN/dx
$\sin^2\theta_W$
(a)
0.30
0.25
0.23
0.20
$\tau \to \ell\nu\nu$
(b)
$\tau \to \pi\nu$
$\sin^2\theta_W$
0.30
0.25
0.23
0.20
0
0.2
0.4
0.6
0.8
1.0
$x = E/E_{beam}$
1-82
4177A205

Fig. 18

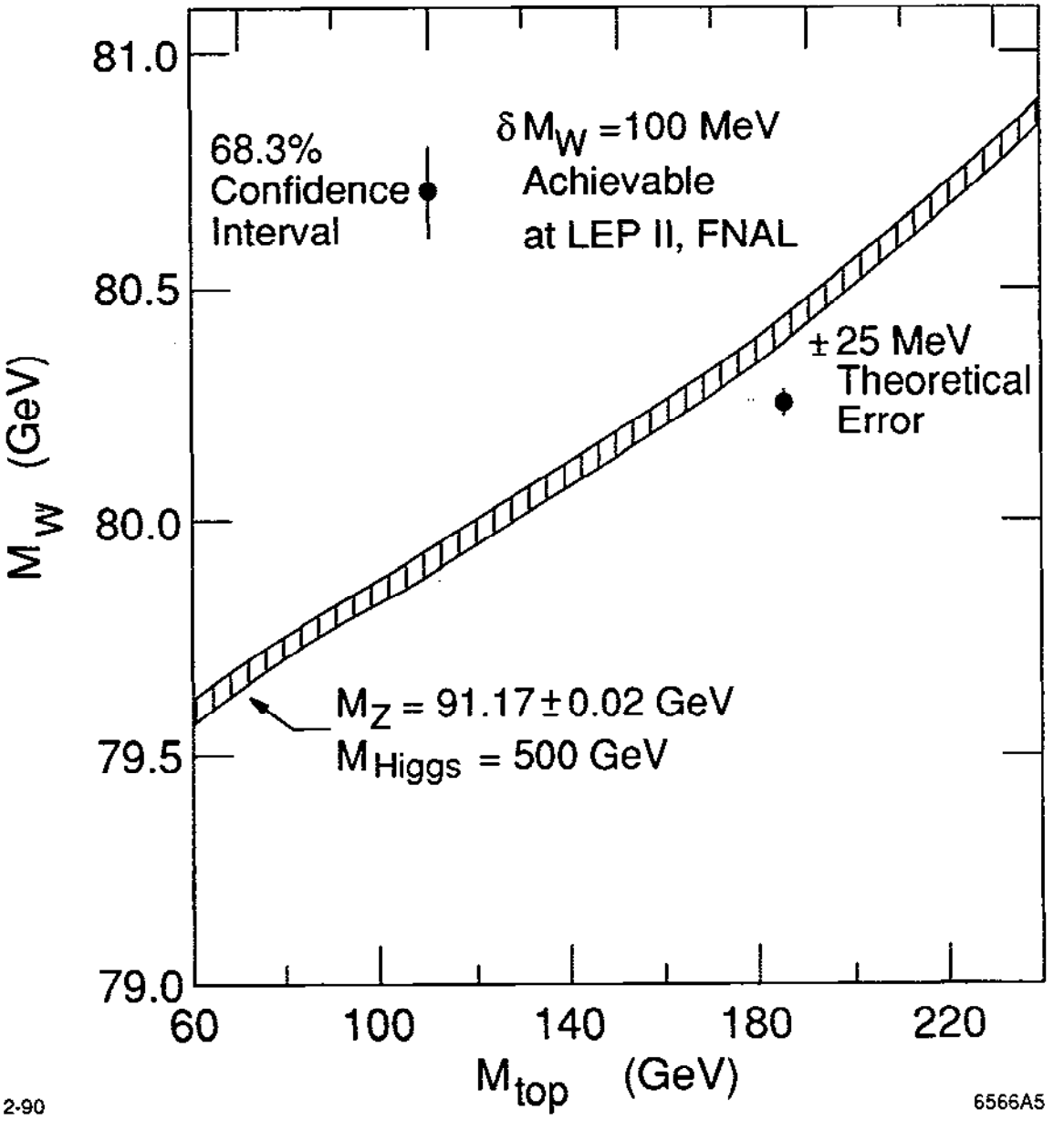
81.0
80.5
80.0
79.5
79.0
60
100
140
180
220
M_W (GeV)
M_{top} (GeV)
68.3% Confidence Interval
δM_W = 100 MeV Achievable at LEP II, FNAL
± 25 MeV Theoretical Error
M_Z = 91.17 ± 0.02 GeV
M_{Higgs} = 500 GeV
2-90
6566A5

Fig. 19

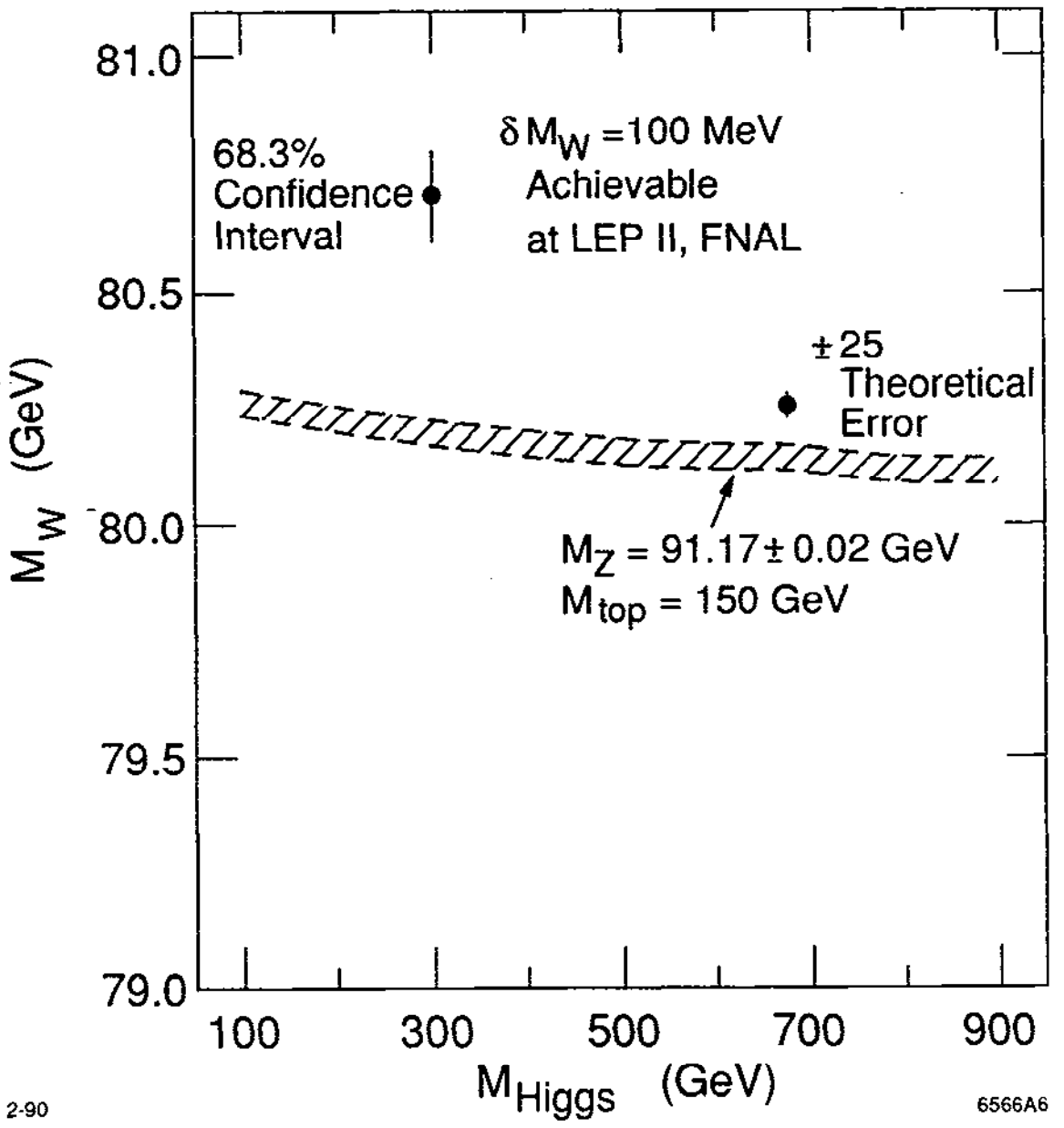
81.0
80.5
80.0
79.5
79.0
M_W (GeV)
68.3%
Confidence
Interval
δM_W =100 MeV
Achievable
at LEP II, FNAL
±25
Theoretical
Error
M_Z = 91.17 ± 0.02 GeV
M_{top} = 150 GeV
100
300
500
700
900
M_{Higgs} (GeV)
2-90
6566A6

Fig. 20

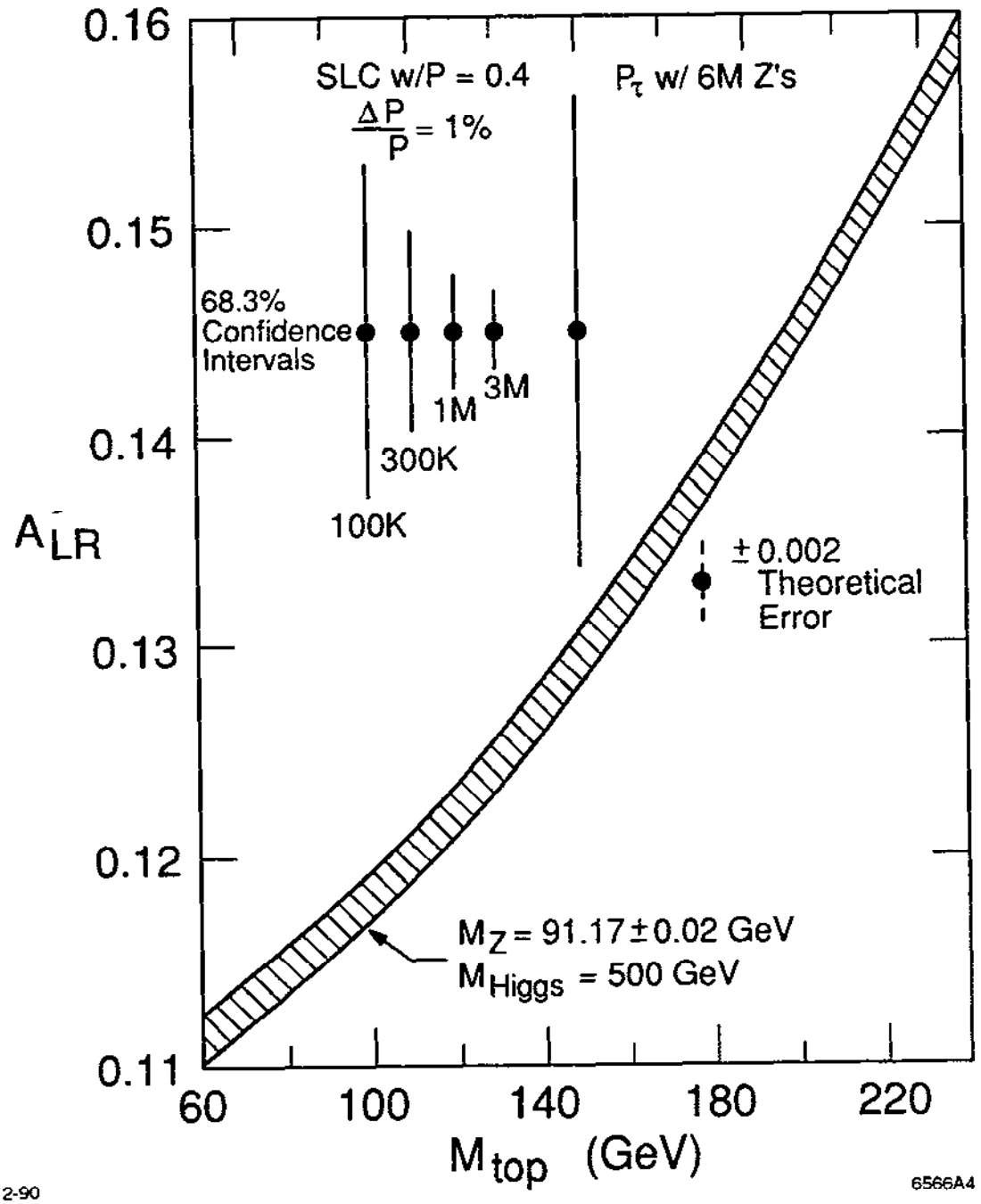
0.16
0.15
0.14
0.13
0.12
0.11
A_{LR}
SLC w/P = 0.4
$\frac{\Delta P}{P}$ = 1%
P_τ w/ 6M Z's
68.3%
Confidence
Intervals
100K
300K
1M
3M
± 0.002
Theoretical
Error
M_Z = 91.17 ± 0.02 GeV
M_{Higgs} = 500 GeV
60
100
140
180
220
M_{top} (GeV)
2-90
6566A4

Fig. 21

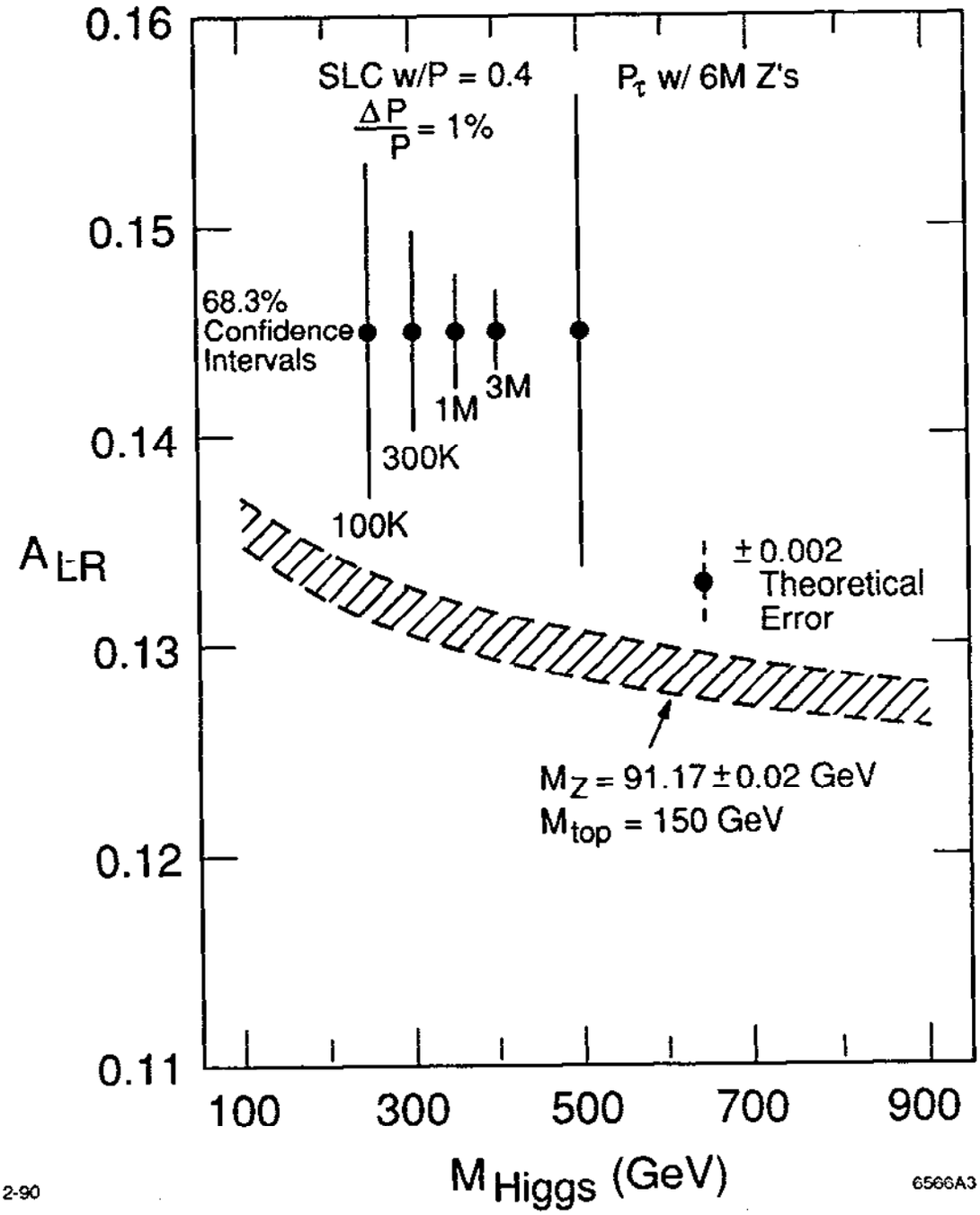
0.16
0.15
0.14
0.13
0.12
0.11
SLC w/P = 0.4
ΔP/P = 1%
P_τ w/ 6M Z's
68.3%
Confidence
Intervals
100K
300K
1M
3M
± 0.002
Theoretical
Error
M_Z = 91.17 ± 0.02 GeV
M_top = 150 GeV
A_LR
100
300
500
700
900
M_Higgs (GeV)
2-90
6566A3

Fig. 22

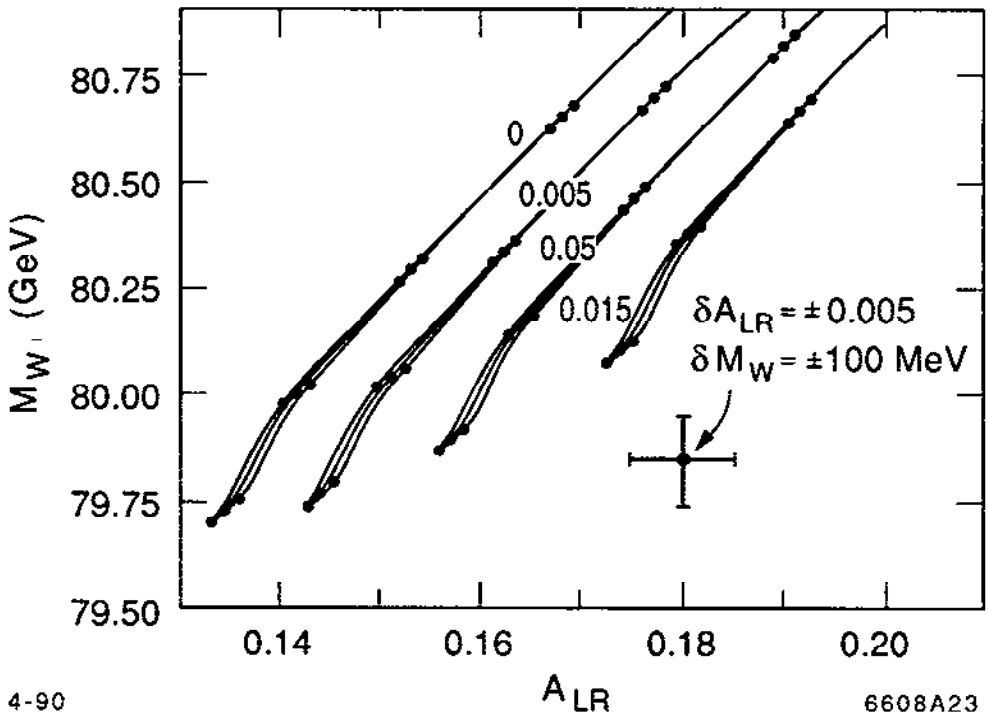
80.75
80.50
80.25
80.00
79.75
79.50
M_W (GeV)
0
0.005
0.05
0.015
$\delta A_{LR} = \pm 0.005$
$\delta M_W = \pm 100$ MeV
0.14
0.16
0.18
0.20
A_{LR}
4-90
6608A23

Fig. 23